



universität
wien

MASTERARBEIT

Enzyme Histochemistry: A tool to decipher metabolic
landscapes in complex tissues with subcellular resolution

verfasst von

Anne Elisabeth Miller

angestrebter akademischer Grad

Master of Science (MSc)

Wien, 2014

Studienkennzahl lt. Studienblatt: A 066 834

Studienrichtung lt. Studienblatt: Masterstudium Molekulare Biologie

Betreut von: Univ. Prof. Dr. Oswald Wagner

Abstract

Cancer is responsible for one out of three deaths in Europe and the development of new therapeutic approaches is one of the main research interests worldwide. Despite great variety in cancer types and origin, cancerogenesis is primarily based on uncontrolled cellular proliferation accompanied by subsequent dissemination to other body parts. Plenty of intracellular and extracellular factors are involved in directing a single cell to lose its growth control. One hallmark of excessive proliferation is the adaptation of cellular energy metabolism, which is prerequisite for a sufficient energy and precursor molecule supply. Aerobic glycolysis, as previously described by Otto Warburg, has become synonymous with *deregulating cellular bioenergetics*. Nevertheless, the process of metabolic adaptation in tumor tissue appears as far more complex as initially imagined. Satisfaction of all proliferative needs such as enhanced ATP production, nucleotide and lipid synthesis is as crucial as maintenance of a functional redox balance. The process of metabolic adaptation gained renewed interest with the observation that a *metabolic coupling* between glycolytic stromal cells and oxidative cancer cells promotes growth and metastatic potential of the tumor. To date, no appropriate tools are available to analyze the *in-vivo* metabolic configuration of complex tumor tissues. In this thesis, I established a technique to demonstrate the activities of five metabolic enzymes in healthy and tumorous tissues to estimate the metabolic flux of glycolysis, the oxidative branch of the pentose phosphate pathway and the citric acid cycle. Combining this technique with traditional histochemical procedures enabled cell type identification and exact intracellular localization of enzymatic activities in complex tissue sections. Moreover, kinetic analysis demonstrated that the activity measurements of the enzymatic reactions followed the stoichiometric principles of enzyme-biochemistry and that the method was able to reveal even subtitle metabolic differences. Furthermore, the identified *metabolic landscapes* were partly recreated in an *in-vitro* 3D organotypic co-culture model of human colon cancer. Establishing this *in-vitro* model allowed further functional evaluations of the role of macrophages and how their activation status might influence cancer cell metabolism. In summary, establishing *metabolic landscapes with enzyme histochemistry* appeared as a valid tool to demonstrate the *in-vivo* metabolic configurations of tumor microenvironments and by translating this to an *in-vitro* model provided a valid platform for functional testing. In the light of personalized medicine, this approach might become an important tool to identify and to target the metabolic constitution of the tumor microenvironment from an individual patient.

Zusammenfassung

Auf der ganzen Welt sind Krebserkrankungen eine der Haupttodesursachen. Die Entwicklung neuer Therapieansätze basiert auf dem fundamentalen Verständnis aller Veränderungen, die sich im Laufe der Krebsentstehung in malignen Zellen ansammeln. Eine Gemeinsamkeit, die fast alle Krebsarten miteinander teilen, liegt im Kontrollverlust über die Zellproliferation. Erhöhte Zellteilungsraten werden durch eine Vielzahl intra- und extrazellulärer Faktoren ausgelöst - haben jedoch immer eine Anpassung des Stoffwechsels zur Auswirkung. Schon vor über 90 Jahren hat Otto Warburg festgestellt, dass Krebszellen, im Gegensatz zu nicht-proliferierenden Zellen ihre Energie durch den Abbau von Glukose zu Pyruvat und anschließender Fermentation zu Laktat gewinnen. Auch wenn ein solcher Vorgang auf den ersten Blick keinen energetischen Vorteil für die Zelle bringt, liefert der anaerobe Abbau von Glukose Vorläufer für eine Vielzahl an wichtigen Zellbausteinen wie z.B. Nukleotide oder Lipide sowie die Aufrechterhaltung einer zellulären Redox-Balance. Des Weiteren wurde vor einigen Jahren die Beobachtung gemacht, dass epitheliale Krebszellen dazu in der Lage sind, die umgebenen Zellen im Tumorstroma dazu zu bringen, erhöhte Glykolyseraten zu betreiben und Laktat und Pyruvat direkt für sie zur Verfügung zu stellen. So wurde klar, dass auch Zellen in der direkten Tumorumgebung an den malignen Veränderungen des Stoffwechsels beteiligt sind. Bis heute gibt es jedoch noch keine Möglichkeit um die metabolischen Eigenschaften von einzelnen Zellen im intakten Gewebe zu bestimmen. Im Zuge dieser Masterarbeit, habe ich ein Verfahren etabliert mit dem es möglich ist, die Konstitution des primären Kohlenhydratstoffwechsels in verschiedenen Zellen zu ermitteln ohne das intakte Gewebe zu zerstören. In Kombination mit traditionellen histochemischen Färbungen ist es so möglich gewesen, einzelne Zelltypen in diesen Geweben zu identifizieren und ihnen spezifische metabolische Eigenschaften zuzusprechen. Außerdem war es möglich, diese *metabolischen Landschaften in-vitro* mithilfe von organotypischen Kolonkrebs Co-Kulturen nachzubilden. Die funktionelle Integration von Makrophagen und Fibroblasten in dieses System hat auch gezeigt, dass die Anwesenheit eines einzelnen Zelltyps zu metabolischen Veränderungen in Krebszellen führen kann. Die Erstellung *metabolischer Landkarten* kann in der Zukunft eine wertvolle Ergänzung zu traditionellen molekularbiologischen Methoden darstellen. Die Anwendung der Methodik hat großes Potential in der personalisierten Medizin, sowie in verschiedensten Forschungsrichtungen wie z.B. Immunbiologie, Neuropathologie und metabolischen Erkrankungen.

Abstract	
Zusammenfassung	
List of Figures	
List of Tables	
List of Reaction Schemes	
List of Equations	
List of Graphs	
List of Supplemental Figures	
Abbreviations	

1. Introduction.....	1
1.1. The metabolic phenotype of cancer.....	1
1.1.1. Metabolic requirements for proliferation.....	2
1.1.2. Nutritional catabolism and metabolic flexibility.....	3
1.1.3. The primary carbohydrate catabolism.....	4
1.2. The concept of the tumor microenvironment.....	7
1.2.1. Molecular microenvironmental factors.....	8
1.2.1.1. Oxidative stress.....	8
1.2.1.2. Lactate and extracellular acidosis.....	9
1.2.2. Cancer associated niche cells.....	9
1.2.2.1. Stromal cells.....	10
1.2.2.2. Immune related cells.....	11
1.3. Imaging the tumor microenvironment - Enzyme histochemistry as a powerful tool in modern pathology.....	12
1.4. Aim of the thesis.....	15
2. Material and Methods.....	17
2.1. Chemicals and Antibodies.....	17
2.2. Cell lines.....	18
2.3. Disposables.....	19
2.4. Determination of enzyme activities in unfixed	

cryostat sections.....	19
2.4.1. Preparation of unfixed cryostat tissue sections.....	19
2.4.2. Preparation of media containing polyvinyl alcohol.....	20
2.4.3. Histochemical detection of enzymatic activities.....	20
2.4.3.1. Dehydrogenases.....	20
2.4.3.1.1. G6PD.....	21
2.4.3.1.2. GAPDH.....	21
2.4.3.1.3. LDH.....	21
2.4.3.1.4. IDH.....	22
2.4.3.1.5. SDH.....	22
2.4.3.1.6. PDH.....	22
2.4.3.2. Kinases.....	23
2.4.4. Fluorescence based detection of dehydrogenase activity.....	23
2.4.5. Combined histochemical determination of dehydrogenase activity with fluorescently labelled antibodies and DAPI.....	24
2.5. Kinetic analysis of dehydrogenases.....	24
2.5.1. Experimental procedure.....	24
2.5.2. Analysis of dehydrogenase biochemical properties using Michaelis-Menten kinetics and Hanes-Woolf plot.....	27
2.6. Imaging and analysis.....	29
2.6.1. Image acquisition.....	29
2.6.1.1. TissueFAX.....	29
2.6.1.2. Confocal laser scanning microscopy.....	30
2.6.2. Image analysis.....	30
2.6.2.1. Colorimetric formazan intensity quantification.....	30
2.6.2.2. Manually merging bright field and fluorescent images.....	30
2.7. Organotypic co-cultures.....	33
2.7.1. Isolation of human peripheral blood mononuclear cells, macrophage differentiation and polarization.....	33
2.7.2. Assembly of organotypic 3D co-cultures on collagen gels.....	34

2.8. Ethics.....	35
3. Results.....	37
3.1. Establishing a method to decipher metabolic landscapes....	37
3.1.1. Dehydrogenase activity stainings reveal different biochemical properties of metabolic enzymes in liver and muscle.....	37
3.1.1.1. G6PD activity.....	37
3.1.1.2. GAPDH activity.....	41
3.1.1.3. LDH activity.....	43
3.1.1.4. IDH activity.....	45
3.1.1.4. SDH activity.....	47
3.1.3. Combination of the dehydrogenase activity assay with fluorescently labelled antibodies for cell type identification.....	50
3.1.4. Substitution of NBT with fluorescent CTC – a great advantage?	50
3.2. Deciphering metabolic landscapes of different tumor types.	54
3.3. Cell type specific metabolic landscapes of healthy and cancerous colon tissue.....	57
3.3.1. Activity of G6PD.....	57
3.3.2. Activity of SDH.....	60
3.4. Metabolic landscapes of organotypic colon cancer co-culture can be used for functional <i>in-vitro</i> assays.....	62
4. Discussion.....	67
4.1. Enzyme histochemistry: a valid tool to decipher metabolic landscapes?.....	67
4.1.1. Kinetic analysis of mouse liver and muscle metabolic enzymes reveals different biochemical properties between both tissues.....	67
4.1.2. Integration of pyruvate metabolism in metabolic	

landscapes is desirable but not methodologically sound.....	69
4.1.3. Substitution of NBT by fluorescent CTC is not recommendable for deciphering metabolic landscapes.....	70
4.2. Metabolic landscapes of complex tumor tissues.....	70
4.2.1. Cell type identification in the metabolic landscapes of healthy and cancerous colon tissue reveals differences in cellular metabolic configurations.....	71
4.2.2. Metabolic structure replication of organotypic colon cancer co-cultures is a valuable tool and reveals a possible role for macrophage activation status on cancer cell metabolism....	73
4.3. Conclusion.....	74
5. Supplements.....	76
Attempting to integrate pyruvate metabolism in metabolic landscaping.....	76
Detection of PDH activity is not necessarily specific.....	76
Detection of PK activity is not necessarily specific.....	76
6. References.....	82
7. Curriculum Vitae	90
8. Danksagung.....	91

List of Figures

Figure 1	The Hallmarks of Cancer	2
Figure 2	The cellular primary carbohydrate catabolism	6
Figure 3	Activity of G6PD, GAPDH, LAD, IDH and SDH indicate metabolic flux of the primary carbohydrate catabolism	16
Figure 4	Experimental setup for biochemical determination of dehydrogenase kinetics	25
Figure 5	Overlay of bright field and fluorescent images using „Image J	32
Figure 6	Assembly of organotypic co-cultures	35
Figure 7	G6PD activities in mouse liver and muscle	38
Figure 8	Inhibition of G6PD in liver and muscle tissue	40
Figure 9	Michalis-Menten kinetics and Hanes-Woolf plot of G6PD in mouse liver and muscle tissue sections	41
Figure 10	Kinetic analysis of GAPDH in mouse liver and muscle	42
Figure 11	Kinetic analysis of LDH in mouse liver and muscle	44
Figure 12	Kinetic analysis of IDH in mouse liver and muscle	46
Figure 13	Kinetic analysis of SDH in mouse liver and muscle	48
Figure 14	Chemical structure of CTC	50
Figure 15	G6PD activity in healthy colon tissue using different redox-dyes	52
Figure 16	3D reconstruction of G6PD activity in mouse liver with nuclear DAPI and MAC-2 antibody stain	53
Figure 17	Metabolic landscapes of lung adenocarcinoma, pleural mesothelioma and colon carcinoma	56
Figure 18	G6PD activity in healthy and cancerous colon tissue	58
Figure 19	G6PD activity in cells of healthy and cancerous colon tissue	59
Figure 20	SDH activity in healthy and cancerous colon tissue	61
Figure 21	LDH activity in colon tumor cells cultured on organotypic co-culture gels	64
Figure 22	Enzyme activities in colon tumor cells cultured on organotypic co-culture gels	65

List of Tables

Table 1	Chemicals	17
Table 2	Cell lines	18
Table 3	Disposables	19
Table 4	G6PD	21
Table 5	GAPDH	21
Table 6	LDH	21
Table 7	IDH	22
Table 8	SDH	22
Table 9	PDH	22
Table 10	PK	23
Table 11	Pipetting scheme for G6PD, GAPDH and LDH kinetic analysis	26
Table 12	Pipetting scheme for mitochondrial IDH and SDH kinetic analysis	27

List of reaction schemes

Reaction scheme 1	14
Reaction scheme 2	37
Reaction scheme 3	41
Reaction scheme 4	43
Reaction scheme 5	45
Reaction scheme 6	47

List of Equations

Equation 1	28
Equation 2	28

List of Graphs

Graph 1	28
---------	----

List of supplemental Figures

Figure S1	Chemical reaction series catalyzed by PDH and the associated detection via reduction of NBT	77
Figure S2	Detection of PDH activity in mouse liver cryosections	78
Figure S3	Coupled series of reactions for PK activity detection	80
Figure S4	Detection of PK activity in mouse liver	81

Abbreviations

3-Phosphoglycerate	3PG
4',6-diamidino-2-phenylindole	DAPI
5' adenosine monophosphate-activated protein kinase	AMPK
5-Cyano-2,3-ditolyl-tetrazolium chloride	CTC
6-Phosphogluconolacton	6PGL
Adenosine diphosphate	ADP
Adenosine monophosphate	AMP
Adenosine triphosphate	ATP
Bovine serum albumin	BSA
Cancer associated fibroblast	CAF
CoEnzyme A	CoA
Dehydroepiandrosterone	DHEA
Deoxyribonucleic acid	DNA
Fetal bovine serum	FBS
Fibroblast activation protein	FAP
Flavin adenine dinucleotide (reduced)	FADH ₂
Flavin adenine dinucleotide	FAD
Glucose-6-phosphate	G6P
Glucose-6-phosphate	G6PD
Glutathione	GSH
Glyceraldehyde-3-phosphate	G3P
Glyceraldehyde-3-phosphate	GAPDH
Hexokinase	HK
Human macrophage colony-stimulating factor	hu-MCSF
Interferon	IFN
Interleukin	IL
Isocitrate dehydrogenase	IDH
Lactate dehydrogenase	LDH
Lipopolysaccharide	LPS
Matrix metalloprotease	MMP
NADPH oxidase complex family	NOXes
Nicotinamide adenine dinucleotide (reduced)	NADH
Nicotinamide adenine dinucleotide phosphate (reduced)	NADPH

Nicotinamide adenine dinucleotide phosphate	NADP ⁺
Nicotinamide adenine dinucleotide	NAD ⁺
Nitroblue terazolium chloride	NBT
Pentose phosphate pathway	PPP
Phosphoenolpyruvate	PEP
Phosphate buffered saline	PBS
Pyruvate dehydrogenase	PDH
Pyruvate kinase	PK
Reactive oxygen species	ROS
Ribose-5-phosphate	R5P
Sedoheptulose 1,7-bisphosphate	S17BP
Sedoheptulose 7-phosphate	S7P
Smooth muscle actin	SMA
Succinate dehydrogenase	SDH
Thiamine pyrophosphate	TPP
Tricarboxylic acid cycle	TCA (cycle)

1. Introduction

1.1. The metabolic phenotype of cancer

Nowadays cancer is seen as one of the main public health issues all over the world. With over three million cases each year only in Europe, the urgent need for new therapeutic options is obvious. The molecular understanding on different levels of cellular organization and regulation is the bases of novel therapeutic approaches. In the past decades of oncogenic research it has become clear, that DNA point mutations, translocations and deletions trigger cancer initiation and metastasis. Further bioinformatic analysis suggests that those genomic mutations affect more than a dozen core signaling pathways involved in tumorigenesis. One of the earliest approaches to further determine a specific cancerous phenotype has been made in the in 2000s by Hanahan and Weinberg. They postulated, that despite great molecular variability in different cancers, it is possible to characterize a distinct number of alterations on cellular as well as on organismic level. All in all, six mandatory molecular alterations have been appointed, which – taken together – define the phenotype of virtually all neoplastic cells. Those features enable cancer cells to escape endogenous protective systems and allow them to survive and grow in a foreign and partly hostile environment. The named properties include *unlimited proliferation potential*, *self-sufficiency in growth signals*, *resistance to anti-proliferative signals*, *apoptotic resistance*, *sustained angiogenesis* and the ability to *metastasize into distant organs* (Hanahan and Weinberg, 2000). The results of a decade of molecular cancer research then motivated Hanahan and Weinberg to propose four new hallmarks in 2011. Those include the two characteristics *genomic instability* and *tumor-promoting inflammation* as well as *reprogramming of the cellular energy metabolism* and *evasion of the host immune system* (**Figure 1**) (Hanahan and Weinberg, 2011) . Besides those nominations, Hanahan and Weinberg suggested yet another dimension of complexity in tumors: Affecting cancer promotion, progression and metastasis, the so called *tumor microenvironment* involves different cell types within the tumor mass. These very popular and often cited *hallmarks of cancer* illustrate that regulation on all levels of cellular organization have impact on the tumorigenic phenotype.

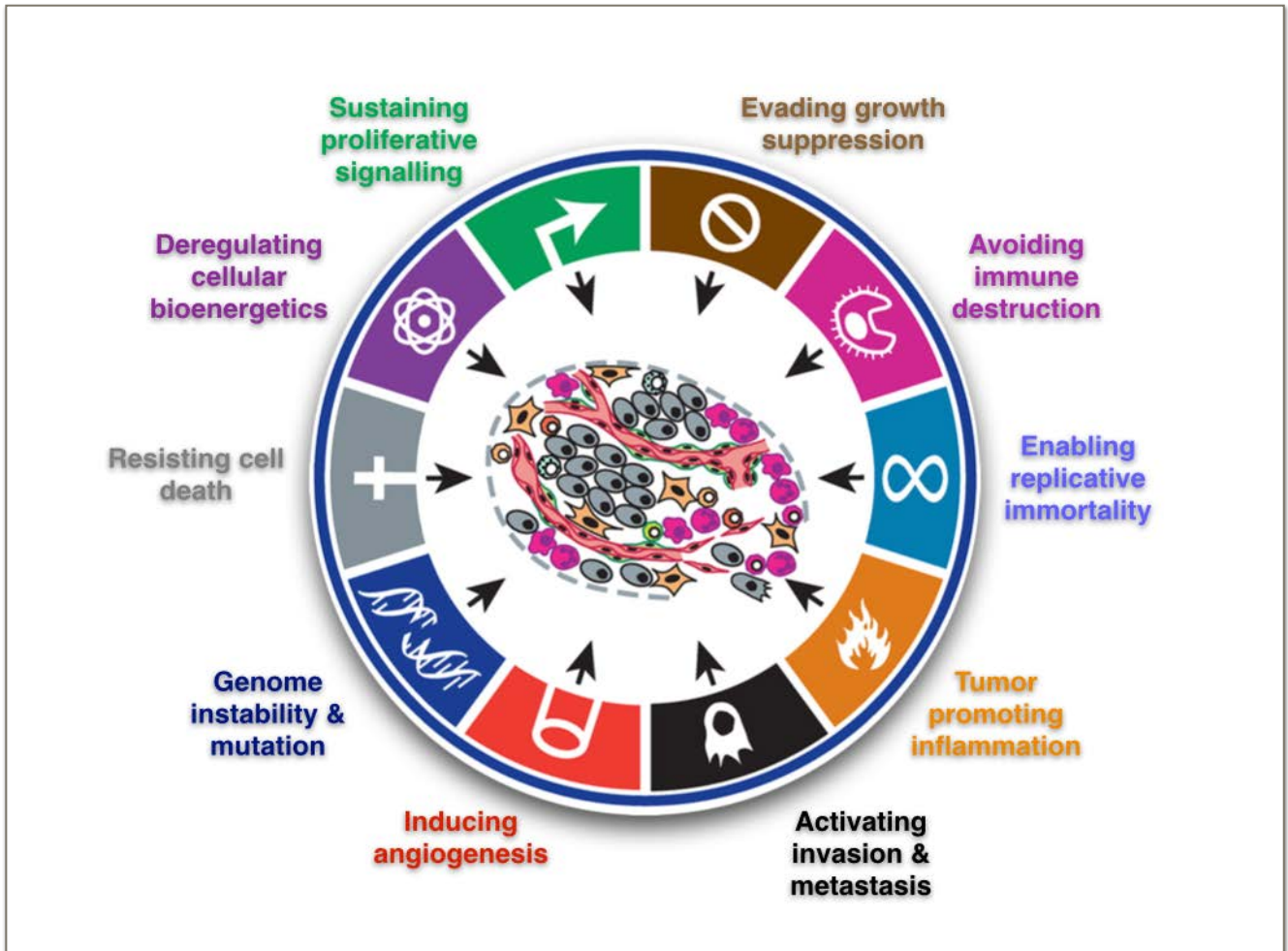


Figure 1. The Hallmarks of Cancer. Illustration describes the 6 hallmarks of cancer as previously described by Hanahan and Weinberg in 2000 as well as the two additional emerging hallmarks and enabling characteristics proposed in 2011. Adapted from Hanahan and Weinberg, Cell, 2011 (Hanahan and Weinberg, 2011).

1.1.1. Metabolic requirements for proliferation

The uncontrolled proliferation of cancer cells as the basis of malignancy induces special metabolic needs for neoplastic cells. Many of the alterations in oncogenic signaling pathways seem to lead to the adaptation of tumor cell metabolism, supporting their growth and survival. Some of these metabolic alterations may even be crucial for malignant transformation. Even though the reprogramming of cellular bioenergetics was proposed as one of the *new* Hallmarks, this phenomenon is one

of the oldest discoveries in the history of cancer research. In the presence of oxygen, most non-proliferative cells convert glucose to pyruvate through the process of glycolysis. The greatest proportion of the pyruvate is then completely oxidized to CO₂ through the tricarboxylic acid cycle (TCA) in the mitochondria. This reaction produces NADH [nicotinamide adenine dinucleotide (NAD⁺), reduced], which then serves in the oxidative phosphorylation to maximize ATP [adenosine 5'-triphosphate] production. The oxygen is utilized as the final acceptor in the electron transport chain forming an electrochemical gradient through which ATP can then be generated. It is only upon oxygen depletion that differentiated cells use pyruvate for the production of lactate – a sensation known as the *Pasteur Effect*. Over 90 years ago, first evidence to link metabolism and cancer was found by Otto Warburg. His observation describes, that in contrast to non-proliferative cells, most cancer cells predominantly produce energy by increased glycolytic rates followed by lactic acid fermentation – even in the abundant presence of oxygen (Warburg et al., 1927). Since then, many approaches led to different explanations about one of the most substantial benefits that glycolytic metabolism provides for highly proliferative cancer cells. In the past, the phenomenon of *aerobic glycolysis* was misinterpreted in a way that aberrant proliferation in neoplastic cells leads to mitochondrial impairments. Hence, the energetic demands of those cells were implemented through aerobic glycolysis. Nowadays it is known that not only mitochondrial respiration is sustained in most cancer cells, but it also obtains its role in ATP production (DeBerardinis et al., 2008).

1.1.2. Nutritional catabolism and metabolic flexibility

Even though the Warburg effect has become synonymous with the previously described hallmark of *deregulating cancer metabolism*, it may not be the only explanation to support such drastic alterations. Overall, the process of oxidative phosphorylation generates up to 36 ATPs per molecule glucose – in contrast, the metabolism of glucose to lactate only generates two ATPs per glucose molecule. Nevertheless, malignant, rapidly growing cells often display increased glycolytic rates by 200 times compared to those of their original tissues. However, metabolic rewiring in proliferating cancer cells is far more complicated than aerobic glycolysis

itself. The metabolic setup of tumors must not only be directed towards the maintenance of energy homeostasis in terms of ATP production, but to also fulfill demands of proliferation: macromolecular synthesis such as nucleotide-, amino acid- and lipid synthesis as well as the preservation of a cellular redox balance (**Figure 2**). It seems obvious, that the metabolic setup, that enables cancer cells to abundantly grow and survive is obligatory in fulfilling the sum of all requirements (Cantor and Sabatini, 2012). Synthesis of amino acids as well as of nucleotides requires higher amounts of carbon and NADPH than ATP. One molecule of glucose can be either processed into 36 molecules of ATP via oxidative phosphorylation, 30 molecules plus two equivalents of NADPH or six carbons that can directly be introduced to the synthesis of macromolecules (Callura et al., 2012). Hence, partial oxidation of glucose through aerobic glycolysis - in contrast to complete oxidation through oxidative phosphorylation - fulfills the metabolic requirements of proliferative cells far more sufficient than at first glance. A part of the cellular available glucose must be converted into macromolecular precursors such as acetyl-Coenzyme A (acetyl-CoA) necessary for the synthesis of fatty acids, glycolytic intermediates for the amino acid synthesis and ribose for nucleotide synthesis (**Figure 2**).

1.1.3. The primary carbohydrate catabolism

Glycolysis is embedded within a complex network of several catabolic pathways. These not only share metabolic intermediates and substrates, but are highly interconnected on multiple levels. The simplified scheme of the primary carbon catabolism connects the main pathways associated with *de novo* synthesis of cellular building blocks such as the pentose phosphate pathway (PPP) and the TCA cycle (**Figure 2**). Increased glucose uptake does not only imply enhanced glycolytic flux, but was shown to elevate fluxes to other affiliated biosynthetic pathways (Locasale and Cantley, 2011). For example can the glycolytic intermediate glucose-6-phosphate (G6P) be transferred into the oxidative branch of the PPP generating ribose-5-phosphate (R5P) and NADPH, which is a major contributor to cellular antioxidative defenses (Cantor and Sabatini, 2012). Fructose-6-phosphate (F6P) and glyceraldehyde-3-phosphate (G3P) can be directed into the non-oxidative arm

of the PPP also leading to R5P creation as an intermediate for nucleotide biosynthesis. Reduction of dihydroxyacetone phosphate to glycerol-3-phosphate (G3P) is substantial for cellular phospholipid and triacylglycerol synthesis (Lunt and Vander Heiden, 2011). Another glycolytic intermediate, 3-phosphoglycerate (3PG) can be shuttled into serine biosynthesis, providing backbone carbons for a variety of essential amino acids. One fate of glycolysis derived pyruvate is to be channeled into the TCA cycle to feed citrate production in the mitochondria. Upon discharge to the cytoplasm, this citrate can then enter in fatty acid synthesis, while an alternative processing of pyruvate is transamination to alanine (Jones and Thompson, 2009). In contrary to glycolysis, the role of the pentose phosphate pathway in proliferation is yet insufficiently understood. However, Glucose-6-phosphate dehydrogenase (G6PD) which catalyzes the first irreversible reaction of the oxidative branch of the PPP (with concomitant NADPH production) is highly elevated in rat (pre-)neoplastic liver lesions and different cancer cell lines (Frederiks et al., 2008). In yeast, a popular eukaryotic model system to study proliferation, a process called *riboneogenesis* has been described. The non-oxidative PPP transforms glycolytic intermediates to R5P without NADPH formation (Clasquin et al., 2011). The sequence of enzymatically catalyzed chemical reactions often requires dietary minerals and other cofactors for proper function. The *metabolic network* describes the interconnection of the different co-dependent catabolic and anabolic pathways and reveals the variety of shared metabolites and intermediates.

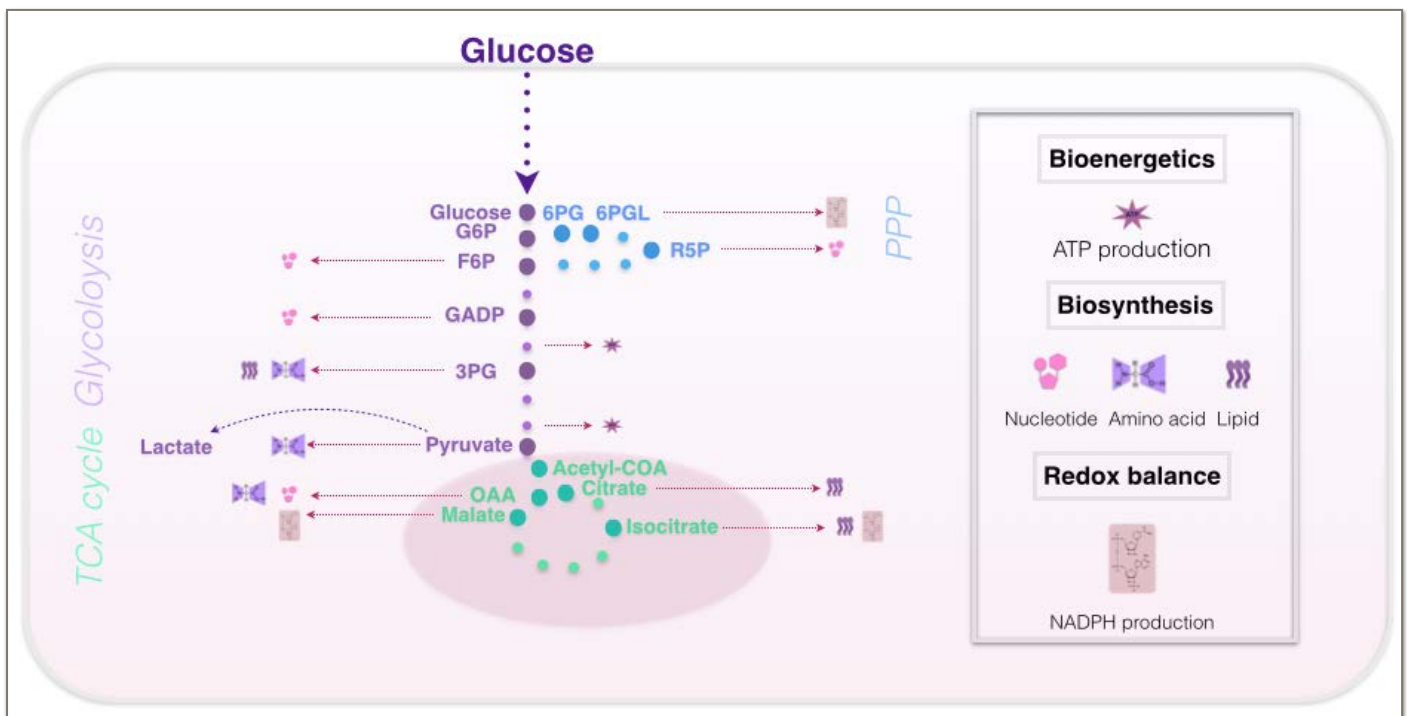


Figure 2. The cellular primary carbohydrate catabolism. The special metabolic demands include bioenergetics (ATP production), macromolecular biosynthesis of nucleotides, amino acids and lipids as well as the maintenance of a redox balance through NADPH generation. To fulfill those, the metabolic setup in proliferating cells is dominated by increased glucose uptake and utilization. Mainly, glucose is metabolized through the process of anaerobic glycolysis leading to lactate production. This allows a proliferating cell to shunt a variety of glycolytic intermediates (purple dots) into anabolic pathways that enable the fulfillment of all three metabolic demands. Adapted from Cantor and Sabatini, Cancer Discovery, 2012 (Cantor and Sabatini, 2012)

1.2. The concept of the tumor microenvironment

Nowadays, research strategies frequently identify genomic variability in between histologically similar neoplasms, different cells within the same tumor mass, but also among cells of the same population within cancerous tissue (Gerlinger et al., 2012). The tumor microenvironment can be seen as a network of different components in which the tumor mass is localized. It has also been part of Hanahan and Weinberg's new postulation in 2011. Those components do not only surround but also infiltrate the tumor and are composed of a multitude of factors with different functions and activities. On the one hand, complex interactions are shown to involve the tumor cells, stromal cells and a variety of immune cells, but on the other hand, also the acellular matrix and soluble factors in the close neighborhood. All of the mentioned factors play their individual role in the regulation of metabolism, tumor growth, progression and metastasis as well as treatment resistance and patient prognosis (Vaupel, 2010). A new area in cancer research was introduced in 2008 when Sonveaux and colleagues demonstrated a *metabolic symbiosis* between hypoxic and aerobic cancer cells (Sonveaux et al., 2008). A scenario, where the lactate produced under hypoxic conditions in the tumor mass is shuttled to aerobic cells where it can be taken up and used as a substrate for oxidative phosphorylation. The result is a fine tuned network of mechanisms in which tumor cells use the available glucose most efficiently. Some cells (hypoxic) down regulate oxidative phosphorylation and consume greater amounts of glucose to maintain redox and energy homeostasis than normoxic cancer cell (Kim et al., 2006; Seagroves et al., 2001). Since then, a variety of temporary as well as spatially pathophysiological heterogeneous conditions have been identified, contributing to the development of a tumor friendly ambience. In the early beginning of carcinogenesis, loss of growth control and concomitant contact inhibition with the basement membrane are the first features to be overcome by developing self-sufficiency in growth promoting signals (Hanahan and Weinberg, 2011). Even though cancer cells are able to proliferate quickly, the tumorous bulk cannot grow beyond a certain size of about 10-50 mm, due to the lack of nutrients and oxygen inside the cellular mass. To overcome this growth barrier tumors are able to induce

emergent blood vessel formation by selective secretion of growth factors.

The so-called process of *neoangiogenesis* establishes an immature and inconsistent vasculature network resulting in unstable oxygen delivery (Gillies et al., 1999).

1.2.1. Molecular microenvironmental factors

The molecular components surrounding neoplastic cells are also quite heterogeneous, both spatially and temporally. Especially, the extracellular matrix and soluble factors altogether form a complex network influencing tumor growth, progression and metastasis. Consequences of abnormal microvascular network and function involve oxygen supply, tumor hypoxia as well as partial nutrient deprivation. Cellular upregulation of aerobic glycolysis and associated lactate accumulation together with consequent extracellular acidosis influence the redox state of the extracellular surrounding as well as the cellular compartments. All of the molecular factors found in the microenvironment have their origin and effect – they can be intrinsic or extrinsic and they can be reason and consequence – creating a fine tuned network to provide a tumor-friendly vicinity.

1.2.1.1. Oxidative stress

Reactive oxygen species (ROS) include hydrogen peroxide (H_2O_2), superoxide anions (O_2^-), singlet oxygen ($^1\text{O}_2$) and ozone (O_3) (Hunter, Desrosiers et al. 1989). Stability varies from nanoseconds to hours and the inducible damage depends on concentration and ratio between ROS and intracellular antioxidants. Oxidative stress describes an imbalance between ROS and associated cellular antioxidative defense mechanisms (Veskoukis et al., 2012). Oxidative stress may derive from a number of intracellular sources, mostly from peroxisomes and mitochondrial associated oxidative phosphorylation (Addabbo et al., 2009). In cancerous cells, high ROS levels may result from increased metabolic- and peroxisomal activity, increased growth factors or imbalance in cytokine signaling (Babior, 1999; Storz, 2005). Enzymatic defense mechanisms include phase II detoxification enzymes

such as glutathione-S-transferase, NADP(H) quinone oxidoreductase, glutathione peroxidase, superoxide dismutase, heme oxygenase and many others. Their elevated expression protects from possible damage due to free oxygen radicals and associated tumor initiation. One of the most important enzymatic detoxification mechanisms is realized by reduced glutathione (GSH). GSH reductase is responsible for reduction of oxidized GSH using G6PD-derived NADPH as reducing equivalent (Pool-Zobel et al., 2005). In cancer cells, elevated G6PD expression has been associated with advantages in ROS defense (Anastasiou et al., 2011).

1.2.1.2. Lactate and extracellular acidosis

In cancer cells the shift towards aerobic glycolysis leads to increased formation of lactate which is transported to the extracellular space where it accumulates. Concentrations range from 4mM to 40mM in different cancer types (Vaupel, 2010). Higher lactate concentrations are associated with an increased metastatic potential and a decreased overall patient survival as this metabolite can interfere with immune surveillance by inhibiting Natural Killer cells activity and T cell cytotoxicity (Fischer et al., 2007; Lardner, 2001). Most importantly, normoxic cancer cells were shown to take up lactate produced by hypoxic cells to directly fuel oxidative phosphorylation (Sonveaux et al., 2008). Additionally, the intracellular readjustment of the pH is very important as even smallest variations can affect many cellular functions including enzyme activities, ATP-production, protein synthesis, proliferation and apoptosis (Pouyssegur et al., 1984; Roos and Boron, 1981). Therefore, cancer cells develop certain auxiliary pH regulating systems such as additional monocarboxylate transporters or a membrane associated carbonic anhydrase which help restore a favorable intracellular pH (Ullah et al., 2006)

1.2.2. Cancer associated niche cells

In the past decades, researchers became aware that tumors are not only composed of neoplastic cells but live along with a heterogeneous population of stromal cells, including endothelial cells and fibroblasts as well as a vast number of immune cells. Those cells profoundly enhance or inhibit tumor progression through the production

of chemokines, growth factors, matrix degrading enzymes and by the support of vascularization as well as breakage of the baseline membrane. Tumor cells seem to be constantly giving instructions through direct interactions or secretion of soluble factors by which benign host cells can be hijacked promoting cancer cell survival and proliferation (Pavrides et al., 2012). In recent years, a great variety of data has been published suggesting various functions of multiple different cell types and subtypes (Hanahan and Coussens, 2012). It seems, that different cell types and even different subtypes have different roles in different tumor tissues and stages and might perhaps even be patient-specific.

1.2.1.1. Stromal cells

The tumor stroma mainly consists of the basement membrane, fibroblasts, the extracellular matrix and the vasculature. While the stromal cells in the microenvironment are not malignant per se, the composition of the stroma permanently changes during malignancy and the associated cells play an undeniable part in cancer growth and survival (Zhang et al., 2008). Cancer associated fibroblasts (CAFs) are the most prominent cells in the tumor microenvironment of various different cancers (Kalluri and Zeisberg, 2006). Recent studies highlight different subpopulations of stromal fibroblasts within close contact to different tumors. Most of them present only partly overlapping functions and phenotypes. The differences in cellular origin may be an explanation for the expression of different markers such as *fibroblast activation protein* (FAP) in over 90% of all carcinomas or alpha-smooth muscle actin (SMA) in human breast and pancreatic tumors (Sugimoto et al., 2006). Different CAF populations have been reported to stem from resident local fibroblasts, bone marrow-derived progenitor cells or epithelial cells after transdifferentiation (Anderberg and Pietras, 2009). In 2009 Lisanti and colleagues hypothesized, that epithelial cancer cells are able to manipulate surrounding stromal fibroblast to undergo transformation and perform aerobic glycolysis. They termed the mechanism the *reverse Warburg effect*. These fibroblasts secrete lactate and pyruvate which can be taken up by cancer cells. These energy-rich components can be directly channeled into the cancer cells TCA cycle and effectively promote ATP generation via oxidative phosphorylation. The

outcome of this scenario is an increased proliferation capacity still consistent with Warburg's original observation and represents the importance of complex interplay between different cell types on the metabolic level (Pavlidis et al., 2009).

1.2.2.2. Immune related cells

As mentioned before, *evading immune destruction* and *tumor promoting inflammation* are nowadays recognized as two hallmarks of cancer (Hanahan and Weinberg, 2011). Nevertheless, most tumor cells do express antigens that enable host immune recognition. Cancers that are detected clinically must most certainly have evaded antitumorigenic immune responses for continual growth. Recent work revealed two major types of modalities to escape immune response through distinct cellular characteristic of the tumor microenvironment. One subset of tumors shows immune cell infiltration comparable to an inflammation phenotype including a broad chemokine profile and type I interferon signature. This subset of tumors seems to elude immune destruction. Another cancer subtype most apparently lacks immune cell infiltration and appears to resist immune response through evading immune recognition (Gajewski et al., 2013). While immune cell infiltration has been successfully linked to patients prognosis, metastatic status and disease reoccurrence, the more specific role of immune cells as regulators of cancer cells energy metabolism is just beginning to be revealed (Biswas et al., 2012b). Macrophages are cells of the innate immune system which reside in every tissue of the body where they are able to engulf pathogens, apoptotic cells and produce immune effector molecules. Originating from the bone marrow and circulating in the blood, they undergo specific differentiation in response to local signals derived from microbes, tissue or lymphocytes (Biswas and Mantovani, 2010). Broadly speaking, two different polarization states of macrophages have been acknowledged: the classically activated type 1 macrophages (M1) and the alternatively activated type 2 macrophages (M2). Triggered by bacterial components or interferon gamma (IFN- γ) macrophages adapt a proinflammatory M1 phenotype which enables them to phagocytize and kill their targets as well as activate cells of the adaptive immune system. Their most important characteristics are the expression of proinflammatory cytokines, reactive oxygen species (ROS), anti-microbial and anti-tumorigenic

activity plus the production of interleukin 12 (IL-12) – a natural killer cell and type 1 T-cell stimulating cytokine. On the contrary, macrophages are polarized towards an M2 phenotype in response to IL-4 or IL-13. They play important roles in the elimination of parasites, tissue remodeling and wound healing. Furthermore, they feature production of ornithine and polyamines (arginase pathway), high expression of scavenging-, mannose- and galactose-receptors and high production of IL-10, IL-1 β , VEGF and matrix metalloproteases (MMPs). They are also able to polarize type 2 T-cells, dampen immune response and show protumoral activities (Biswas et al., 2012a). Nowadays, it is well established that metabolism serves as an important factor in macrophage phenotype switching. The coherence between macrophages and metabolism is bipolar – on one side macrophages can modulate metabolic functions, on the other hand intracellular metabolic functions are responsible for their activation state (Pavlidis et al., 2009). For example, do IFN- γ or lipopolysaccharide exposed macrophages show a metabolic shift towards anaerobic glycolysis, increasing glycolytic rates and decreasing oxygen consumption while IL-4 has no such effect (Haschemi et al., 2012; Odegaard and Chawla, 2011).

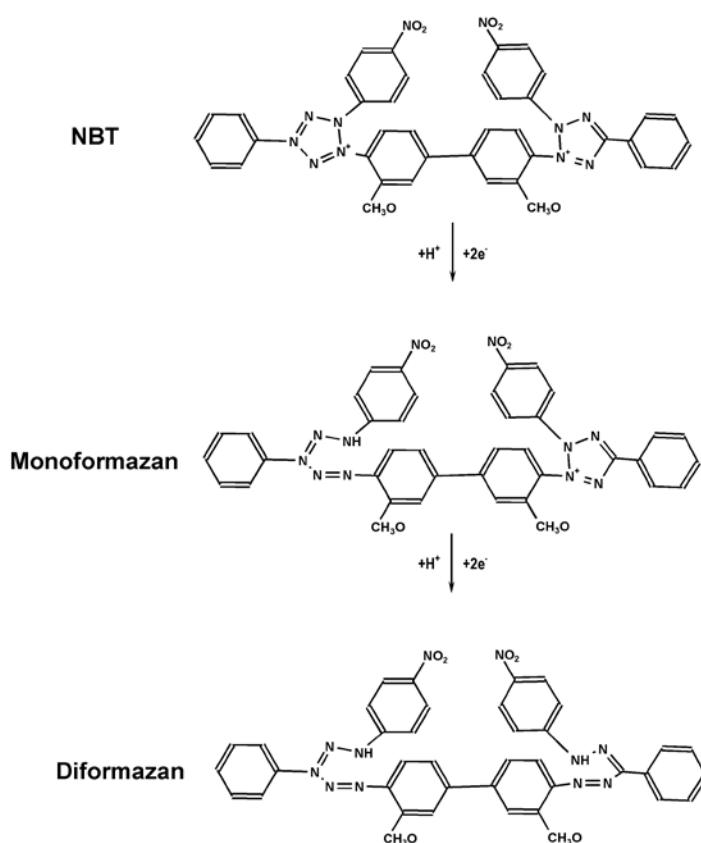
1.3. Imaging the tumor microenvironment - Enzyme histochemistry as a powerful tool in modern pathology

Over the past decades cancer related research concentrated on common genetic mutations and their functional consequences in cell cycle control. These results enlightened the functions of a multitude of tumor suppressor genes, oncogenes and associated signaling pathways involved in cellular proliferation and death. In the present time, tumors are widely recognized as heterogeneous tissue-like entities which not only depend on their own genetic alterations but on mutual interactions with their direct environment. Moreover, it has become clear that tumor promotion and progression is not a result of only a certain genomic setup. Transcription, translation, protein assembly and other variables determine the activity of each process within the cell - including enzymatic activity. Therefore it is more than obvious that localization or measurement of mRNA or protein levels of an enzyme

alone is not sufficient in predicting its activity. Likewise, activity measurements of purified enzymes in tissue or cell homogenates most obviously do not illustrate the activity that reflects the *in-vivo* situation (Van Noorden, 2010).

Enzyme histochemistry is a method for imaging enzymatic reactions that links biochemistry and morphology (Hardonk and Koudstaal, 1976). Its application may serve as valuable supplement to conventional histological, immunohistochemical and molecular pathological methods and has been applied to various human and mice tissues as well as biopsy specimens. Especially in the field of neuropathological research, enzyme histochemical methods are frequently applied to diagnose celiac disease and brain lesions (Ishii, 1969). One of the most studied enzyme histochemical methods is the visualization of dehydrogenase activity with redox-sensitive tetrazolium salts. Tetrazolium salts such as *nitroblue tetrazolium chloride* (NBT) are yellow and partly water soluble, but can be reduced to a water-insoluble and strongly colored formazan. Usually applied in viability assays or in the test for chronic granulomatous disease, reduced NBT immediately binds to local protein and permits precise localization of the investigated dehydrogenase. The chemical reaction of the detection involves multiple electron transfers. Dehydrogenases are able to oxidize their substrates by transferring an electron to electron acceptors such as NAD^+ or NADP^+ forming NAD(P)H/H^+ as a byproduct. In turn, NAD(P)H/H^+ can reduce NBT to its monoformazan state - which results in a pink staining. Upon further reduction by H^+ , the diformazan product is formed, leading to a dark purple staining (**reaction scheme 1**) (Altman, 1974). To speed up the electron transfer from the electron acceptor to the tetrazolium salt, an exogenous electron transporter such as 1-methoxyphenazine methosulfate is usually applied to the reaction (Van Noorden et al., 1983). A more modern approach has been introduced by using *5-cyano-2,3-ditolyl-tetrazolium chloride* (CTC), a tetrazolium salt which is reduced to a fluorescent formazan. CTC has been applied to visualize dehydrogenase reactions in viability assays, flow cytometry and in combination with confocal laser scanning microscopy to precisely localize enzyme activities in individual cells. Theoretically, all dehydrogenases can be visualized using the same method (Meier-Ruge and Bruder, 2008). Enzyme histochemistry does not provide absolute quantitative data, but good correlations have been described between histochemically judged enzyme activity per area and

biochemically determined activity per tissue weight (Hardonk and Koudstaal, 1976). In the oncological praxis, succinate dehydrogenase (SHD) and lactate dehydrogenase (LDH) activities are of particular interest because they demonstrate tumor vitality and glycolytic activity (Prahoveanu et al., 1973). It has been demonstrated, that tumor tissue with a high glycolytic activity is particularly resistant to radiotherapy. Therefore, enzyme histochemistry may provide an efficient and inexpensive tool to assess the actual energy metabolism and to estimate the efficiency of the therapeutic strategy (Landex et al., 2006). Overall, enzyme histochemistry may serve as a sensitive technique which is able to reveal even small metabolic imbalances. The utilization of enzyme histochemistry represents a valuable complementation to other molecular and pathological techniques proving insights in the individual physiology of particular pathological processes.



Reaction scheme 1. Proposed chemical reduction properties of NBT.

Reduction of the colorless redox-dye NBT first forms a water insoluble pink monoformazan product which turns to a dark purple diformazan product upon further reduction.

1.4. Aim of the thesis

Enzyme histochemistry is a relatively simple technique and provides reliable results. However, this method is not frequently applied in cancer research although it was already successfully applied to subclassify human lymphomas or to detect hematologic and hepatologic malignancies (Dawson and Filipe, 1967). Although, the idea of cancer as a complex tissue-like entity has become well accepted, most cancer related studies focusing on metabolism were performed in simplified model-system such as unicellular and one dimensional tissue culture. Therefore, the aim of this study was to establish a method that allows the analysis of metabolic networks in intact primary tissue to reflect the *in-vivo* situation and account for complexity of the tissue. In the course of this thesis, I developed a strategy and established a method to dissect metabolic landscapes of healthy and cancerous tissues by measuring the activities of five key enzymes of carbohydrate metabolism. In our model, the activity of glyceraldehyde-3-phosphate dehydrogenase (GAPDH) was used as an indicator for the glycolytic rate, LDH as an attribute of aerobic glycolysis, G6PD as indicator of carbon flux through the oxidative branch of the PPP and mitochondrial isocitrate dehydrogenases (IDH) and SDH represented flux rates of the citric acid cycle (**Figure 3**). In addition, the combination of enzyme histochemistry and immunohistochemical staining techniques allowed a precise localization of enzyme activities within individual cells and on subcellular level. Together, this approach provided valuable information about the cellular as well as area-specific configuration of metabolism within complex tissue. This method may not only serve cancer related research, but might be important to any scenario in which the metabolic-configuration of individual cell types in a heterogeneous multicellular networks are of importance.

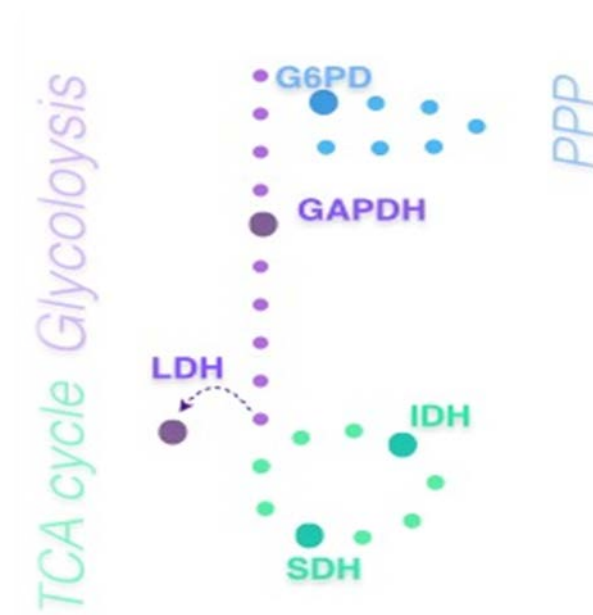


Figure 3. The activity of G6PD, GAPDH, LDH, IDH and SDH indicate the metabolic-flux of the primary carbohydrate catabolism. G6PD indicates carbon flux through the oxidative branch of the PPP (blue), GAPDH functions is an indicator for the glycolytic rate, LDH is an attribute of aerobic glycolysis (purple). Mitochondrial IDH and SDH stand for flux rates in the citric acid cycle (TCA cycle; green).

2. Material and methods

2.1. Chemicals and Antibodies

Chemical	Providing Company
1-Methoxyphenazine methosulfate	Sigma-Aldrich
2-methyl butane	Sigma-Aldrich
5-Cyano-2,3-di-(p-tolyl)tetrazolium chloride (CTC)	Sigma-Aldrich
anti-Human FAPA Alexa 647	BiossUSA
anti-Mouse Ki67 FITC	BD Bioscience
anti-Mouse MAC-2 M3/38 Alexa Fluor 647	BioLegend
Bovine Serum Albumin (BSA)	Gibco
Collagen I, rat	Becton Dickinson
DAPI	Sigma-Aldrich
Dehydroepiandrosterone-2,2,3,4,4,6-d ₆ (DHEA)	Sigma-Aldrich
DL-Glyceraldehyde 3-phosphate diethyl acetal barium salt	Santa Cruz Biotechnology
DL-Isocitric acid trisodium salt hydrate	Sigma-Aldrich
DMEM	Gibco
Ethanol	Sigma-Aldrich
Fetal Bovine Serum (FBS)	Gibco
Glucose-6-phosphate	Sigma-Aldrich
Glycerol Gelatin	Sigma-Aldrich
human-MCSF	Sigma-Aldrich
Lipopolysaccharide (LPS)	Sigma-Aldrich
Magnesium Chloride	Sigma-Aldrich
Malonic acid	Sigma-Aldrich
Mowiol	Sigma-Aldrich

N,N-Dimethylformamide	Sigma-Aldrich
Nitrotetrazolium Blue chloride	Sigma-Aldrich
Oxaloacetic acid	Sigma-Aldrich
Penicillin/Streptomycin	Gibco
Phenazine methosulfate	Sigma-Aldrich
Phosphate buffered saline (PBS)	Sigma-Aldrich
Poly(vinyl alcohol) M _w 89,000-98,000	Sigma-Aldrich
RPMI-1640	PAA
Sodium DL-lactate	Sigma-Aldrich
Sodium iodoacetate	Sigma-Aldrich
Sodium oxamate	Sigma-Aldrich
Sodium succinate dibasic	Sigma-Aldrich
Tissue-Tek® O.C.T™ Compound	Sakura
Trizma-Maleate	Sigma-Aldrich
Trypsin-EDTA	Gibco
TWEEN® 20	Sigma-Aldrich
β-Nicotinamide adenine dinucleotide hydrate	Sigma-Aldrich
β-Nicotinamide adenine dinucleotide phosphate hydrate	Sigma-Aldrich

Table 1. Chemicals

2.2 Cell lines

Cell line	Provided by
HTC-116 (ATCC® Number CCL-247)	Provided by Dr. Dolznig
Primary cancer associated fibroblasts	Provided by Dr. Dolznig

Table 2. Cell lines.

2.3. Disposables

Disposable	Providing Company
Cell culture dishes (10cm, 6-well, 24-well)	Techno Plastic Products AG
Eppendorf tubes	Eppendorf
Leucosep TM	Greiner Bio-One
MACS CD14 MicroBeads	Miltenyi Biotec
Nylon mesh inserts	Provided by Dr. Dolznig
Silicone gel casting devices	Self-made by Dr. Dolznig
Superfrost Microscope slides	Thermo Scientific
Tisse-Tek [®] Cryomolds	Sakura

Table 3. Disposables.

2.4. Determination of enzyme activities in unfixed cryostat sections

The demonstration of enzyme activities was based on the method described by Van Noorden and Frederiks (Noorden, Frederiks et al. 1992).

2.4.1. Preparation of unfixed cryostat tissue sections

Cryostat sections were prepared from frozen tissue that was kept at -80°C after being snap frozen in O.C.T. medium. The tissue block was attached to a metal chuck in the cryostat cabinet (CM3050 S, Leica) using O.C.T. containing medium at -20°C. After temperature compensation for five minutes, the tissue block was trimmed to desired level and then cut in 7µm thickness at slow and constant speed. Slides were kept at -80°C for at least 24 hours.

2.4.2. Preparation of media containing polyvinyl alcohol

18% Polyvinyl alcohol was dissolved in enzyme specific buffer stirring in a water bath at 60°C for 48 hours until the mixture was clear. The solution was stored in air tight vials at 60°C in a heater (Hybridiser HB-1, Techne). Before further usage solution was cooled to 37°C.

2.4.3. Histochemical detection of enzymatic activities

2.4.3.1. Dehydrogenases

Basically, all dehydrogenase activities can be demonstrated according to the same principle with variation of their substrates and coenzymes. All reactions contained NBT as a detection reagent, sodium azide to inhibit intrinsic electron transfer at the mitochondrial membrane and an exogenous electron transporter. The electron transporter was chosen according to the enzymatic subcellular localization. Cytoplasmatic enzymes when demonstrated using methoxyphenazine methosulfate whereas mitochondrial enzymes were demonstrated using phenazine methosulfate, as it can pass the mitochondrial membrane.

The detection mastermix contained: NBT (final concentration 5 mM, dissolved in 50% Ethanol and 50% dimethylformamide), sodium azide (final concentration 5 mM). and methoxyphenazine methosulfate (final concentration 0,45 mM) or phenazine methosulfate (final concentration 0,2 mM). Compounds were added to polyvinylalcohol medium containing the enzyme specific substrate and coenzymes as indicated in **2.4.3.1.1. – 2.4.3.1.6.**

Tissue sections were left to defreeze for two minutes at room temperature. Polyvinylalcohol medium containing the enzyme specific substrate and coenzymes was generously applied to the tissue sections. Control incubations were carried out in the presence of an enzyme specific inhibitor (see **2.4.3.1.1. - 2.4.3.1.6.**). The reaction was carried out for 15 minutes in the dark at room temperature while gentle shaking. Slides were washed two times in 60°C PBS for three minutes and once in 4°C PBS for three minutes. Tissue sections were dried and mounted in glycerol gelatin.

2.4.3.1.1. G6PD

Electron carrier	0,45 mM methoxyphenazine methosulfate
Buffer	0,1 M Tris-Maleate, pH 7,5
Substrate	15 mM glucose-6-phosphate
Coenzyme	0,8 mM NADP ⁺
Other constituents	4 mM MgCl
Inhibitor	60 mM DHEA

Table 4. Substrates for detection of G6PD activity

2.4.3.1.2. GAPDH

Electron carrier	0,45 mM methoxyphenazine methosulfate
Buffer	0,1 M Tris-Maleate, pH 8,5
Substrate	2,5 mM diethyl-acetal salt of glyceraldehyde-3-phosphate
Coenzyme	3 mM NAD ⁺
Other constituents	-
Inhibitor	40 mM iodoacetate

Table 5. Substrates for detection of GAPDH activity.

2.4.3.1.3. LDH

Electron carrier	0,45 mM methoxyphenazine methosulfate
Buffer	0,1 M Tris-maleate, pH 7,5
Substrate	150 mM sodium lactate
Coenzyme	3 mM NAD ⁺
Other constituents	-
Inhibitor	200 mM sodium oxamate

Table 6. Substrates for detection of LDH activity

2.4.3.1.4. IDH (NAD⁺ dependent)

Electron carrier	0,2 mM phenazine methosulfate
Buffer	0,1 M Tris-maleate, pH 7,5
Substrate	100 mM D,L-isocitrate
Coenzyme	7 mM NAD ⁺
Other constituents	10 mM MgCl
Inhibitor	200 mM oxaloglycine

Table 7. Substrates for detection of IDH activity

2.4.3.1.5. SDH

Electron carrier	0,2 mM phenazine methosulfate
Buffer	0,1 M Tris-HCl, pH 8,0
Substrate	60 mM succinate
Coenzyme	-
Other constituents	-
Inhibitor	250 mM malonate

Table 8. Substrates for detection of SDH activity

2.4.3.1.6. PDH

Electron carrier	0,45 mM methoxyphenazine methosulfate
Buffer	0,1 M Tris-Maleate, pH 8,0
Substrate	320 mM Pyruvate
Coenzyme	16 mM TPP, 10 mM CoA, 7 mM NAD, 10 mM FAD
Other constituents	10 mM MgCl, 4 mM CaCl
Inhibitor	300 mM 3-Fluoro-2-oxopropanoic acid

Table 9. Substrates for detection of PDH activity

2.4.3.2. Kinases

To measure the activity of enzymes other than dehydrogenases coupled multistep reactions were performed. The reaction product of the enzyme of interest served as a substrate for a dehydrogenase. The product was further converted with simultaneous reduction of NBT. To ensure that the dehydrogenase activity was not rate limiting, auxiliary enzymes were dissolved in ddH₂O + 0.1% BSA, applied to squares of 1cm² on microscope slides and dried in air. Cryostat sections were placed onto the glass slides which were kept at -20°C until further usage. Subsequently, the NBT reaction was performed as described in **2.4.3.1**. Enzyme specific substrates, coenzymes and inhibitors were added as indicated below:

PK

Electron carrier	methoxyphenazine methosulfate
Buffer	0,1 M Tris-Maleate, pH 7.5
Substrates	300 mM PEP, 2,5 mM ADP
Coenzyme	1,9 mM NADP
Other constituents	25 mM MgCl, 6,5 mM AMP, 25 mM glucose
Auxiliary enzymes	2,5U hexokinase (HK), 2,5U G6PD
Inhibitor	300 mM Glutathione

Table 9. Substrates for detection of PK activity

2.4.4. Fluorescence based detection of dehydrogenase activity

In contrast to NBT, CTC gives rise to a fluorescent formazan product upon reduction. Experimental handling was performed equal to NBT. The reaction was carried out as indicated in **2.4.3.1**. Because fluorescent staining was diminished upon mounting in glycerol-gelatin, tissue sections were mounted in mowiol.

2.4.5. Combined histochemical determination of dehydrogenase activity with fluorescently labelled antibodies and DAPI

Subsequent to the dehydrogenase activity assay, the tissue sections were blocked in 1% BSA dissolved in PBS + 0.001% Tween 20. After short washing in PBS + 0.001% Tween 20, 20µl of a 1:50 antibody dilution was applied to the tissue sections and incubated at room temperature for 60 minutes while gently shaking in the dark. Slides were washed three times for three minutes in PBS + 0.001% Tween 20. 50µl of 1x DAPI were applied to each section and incubated for 15 minutes at room temperature in the dark while gently shaking. Slides were washed three times for three minutes in PBS + 0.001% Tween 20. Tissue sections were dried for five minutes at room temperature, mounted in mowiol and sealed with nail lacquer.

2.5. Kinetic analysis of dehydrogenases

2.5.1. Experimental procedure

Tissue blocks of mouse liver and muscle tissue frozen in O.C.T. containing medium were kept at -80°C and unfixed cryostat tissue sections were prepared according to the protocol in **2.1.1**. Two sections of liver tissue and two sections of muscle tissue were positioned next to each other on one microscope slide (**Figure 4 A**). Three slides were prepared for each time point and kept at -80°C for 48 hours. For each reaction containing the appropriate substrate, a starting concentration (50x, “concentration 4”) was used to prepare serial dilutions with a first dilution step of 1:2, followed by 1:10 to reach the final concentrations (**Figure 4 B and C**). For each substrate specific reaction, a total volume of 500µl PVA-containing medium was prepared, necessary reagents were added as shown in **Table 10 and 11**. At the time of the experiment, sections were defrozed for two minutes at room temperature. For each time point, 50µl of the proper dilution was added to each liver and muscle tissue section (**Figure 4 A**). Reactions were stopped by washing the tissue sections two times in 60°C PBS for three minutes and once in 4°C PBS for three minutes. Tissue sections were dried and mounted in glycerol-gelatin.

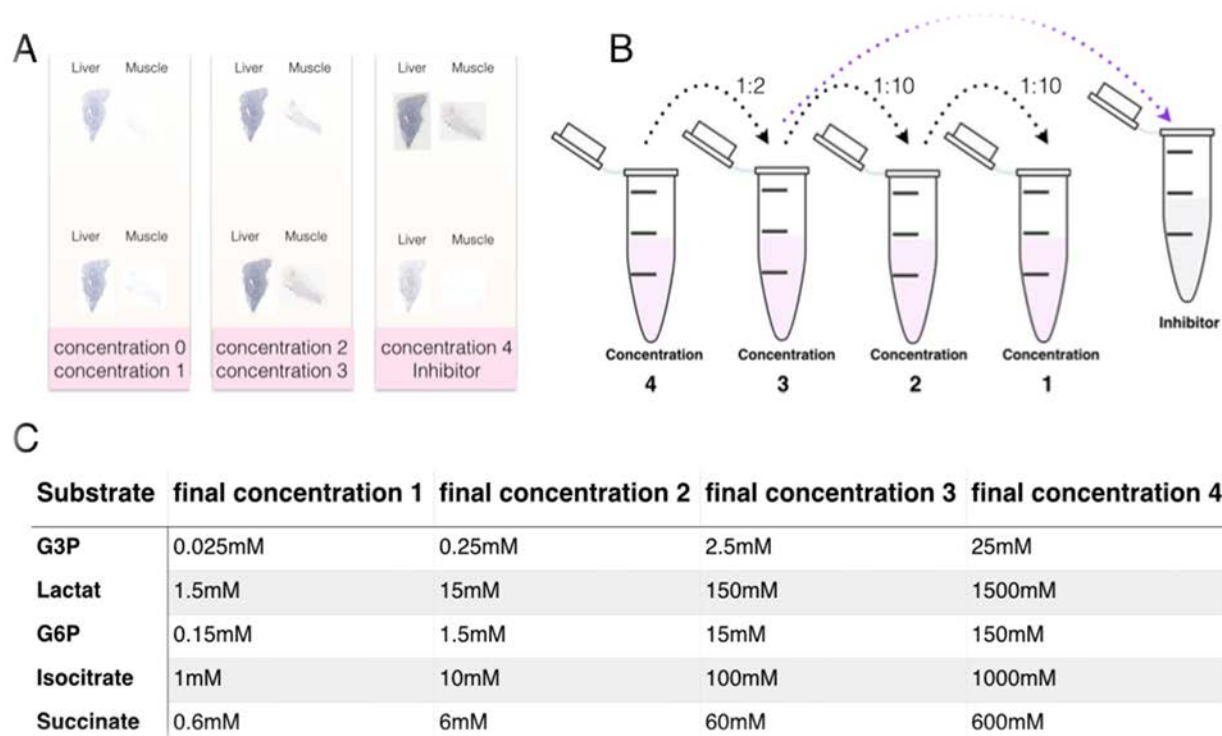







Figure 4. Experimental setup for biochemical determination of dehydrogenase kinetics. NBT was used as detection reagent. Different substrate concentrations were applied to liver and muscle unfixed frozen tissue sections (A). A dilution series of different substrates was prepared (B) which was specific for the detected enzyme (C).

G6P						
Reagents	Concentration	final conc. 0mM	final conc. 0.15mM	final conc. 1.5mM	final conc. 15mM	final conc. 150mM
NBT	125mM	20	20	20	20	20
sodium azide	125mM	20	20	20	20	20
meth. methos.	11.25mM	20	20	20	20	20
conc. 1	3.75mM	-	20	-	-	-
conc. 2	37.5mM	-	-	20	-	-
conc. 3	375mM	-	-	-	20	-
conc. 4	750mM	-	-	-	-	100
NADP	20mM	20	20	20	20	20
MgCl	100mM	20	20	20	20	20
PVA-containing medium		400	380	380	380	300

G3P						
Reagents	Concentration	final conc. 0mM	final conc. 0.025mM	final conc. 0.25mM	final conc. 2.5mM	final conc. 25mM
NBT	125mM	20	20	20	20	20
sodium azide	125mM	20	20	20	20	20
meth. methos.	11.25mM	20	20	20	20	20
conc. 1	0.625mM	-	20	-	-	-
conc. 2	6.25mM	-	-	20	-	-
conc. 3	62.5mM	-	-	-	20	-
conc. 4	625mM	-	-	-	-	100
NAD	75mM	20	20	20	20	20
PVA-containing medium		320	400	400	400	320

Lactate						
Reagents	Concentration	final conc. 0mM	final conc. 1.5mM	final conc. 15mM	final conc. 150mM	final conc. 1.5mM
NBT	125mM	20	20	20	20	20
sodium azide	125mM	20	20	20	20	20
meth. methos.	11.25mM	20	20	20	20	20
conc. 1	37.5mM	-	20	-	-	-
conc. 2	375mM	-	-	20	-	-
conc. 3	3750mM	-	-	-	20	200
NAD	75mM	20	20	20	20	20
PVA-containing medium		420	400	400	400	220

Table 11. Pipetting scheme for G6PD, GAPDH and LDH kinetic analysis

Isocitrate

Reagents	Concentration	final conc. 0mM	final conc. 1mM	final conc. 10mM	final conc. 100mM	final conc. 1000mM
NBT	125mM	20	20	20	20	20
sodium azide	125mM	20	20	20	20	20
phen. methos.	5mM	20	20	20	20	20
conc. 1	25mM	-	20	-	-	-
conc. 2	250mM	-	-	20	-	-
conc. 3	2500mM	-	-	-	20	200
NAD	175mM	20	20	20	20	20
MgCl	250mM	20	20	20	20	20
PVA-containing medium		400	380	380	380	200

Succinate

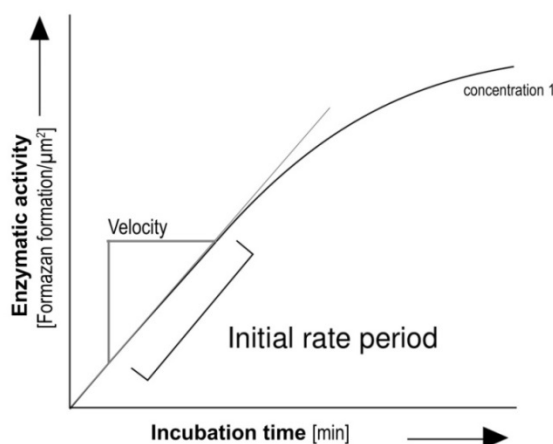
Reagents	Concentration	final conc. 0mM	final conc. 0.6mM	final conc. 6mM	final conc. 60mM	final conc. 600mM
NBT	125mM	20	20	20	20	20
sodium azide	125mM	20	20	20	20	20
phen. methos.	5mM	20	20	20	20	20
conc. 1	15mM	-	20	-	-	-
conc. 2	150mM	-	-	20	-	-
conc. 3	1500mM	-	-	-	20	-
conc. 4	3000mM	-	-	-	-	100
PVA-containing medium		440	420	420	420	340

Table 12. Pipetting scheme for mitochondrial IDH and SDH kinetic analysis.

2.5.2. Analysis of dehydrogenase biochemical properties using Michaelis-Menten kinetics and Hanes-Woolf plot

The rate of an enzymatic reaction increases with rising substrate concentrations until the maximum reaction rate is reached (V_{\max}). When all substrate binding sites are occupied the reaction rate is only limited by the speed of the catalytic process (zero-order activity of an enzyme). K_M , the substrate concentration at which the reaction rate is half of V_{\max} is a measure of how solid the substrate is bound to the enzyme. For most enzymes, a larger K_M value implies a weaker substrate binding capacity (Hardonk and Koudstaal, 1976). Most enzyme kinetics studies are models for single-substrate reactions. However, reactions catalyzed by dehydrogenases are multi-substrate reactions. It is only upon saturating concentration of one substrate that the enzymes behave like in single-substrate reactions. Therefore, concentrations of all enzyme-specific coenzymes and cofactors were kept constant and at saturating levels. Technically, the *reaction velocity* v was calculated by plotting the measured enzymatic activities, in this case the formazan formation in

ratio to the incubation times (5, 10, 15 and 20 minutes). This was performed for five different substrate concentrations and the *slope* of each curve equaled the *reaction velocity* v (**Graph 1**).



Graph 1. Progress curve for an enzymatic reaction. The slope in the initial rate period is the *reaction rate* or *velocity* v . The Michaelis–Menten and Hanes-Woolf equations describe how this slope varies with variations in substrate concentrations.

The most noted model to describe enzymatic behaviors is the *Michaelis-Menten kinetics*. The equation describes the rate of an enzymatic reaction by relating the reaction velocity v to the substrate concentration $[S]$ with the formula

$$v = \frac{d[P]}{dt} = \frac{V_{\max}[S]}{K_m + [S]}$$

Equation 1.

The corresponding calculations were performed using the GraphPad Prism 5 software.

Due to the experimental setup, a more adequate calculation represented the *Hanes-Woolf plot* in which the ratio of the initial *substrate concentration* $[S]$ to the *reaction velocity* v was plotted against $[S]$:

$$\frac{[S]}{v} = \frac{1}{v_{\max}}[S] + \frac{K_m}{v_{\max}}$$

Equation 2.

Because statistical errors could only occur in the velocity but not in the substrate concentration statistical outliers did not falsify the results. Again, calculations were performed using the GrapPad Prism 5 software and data yielded a straight line of slope $1/V_{\max}$ and a x-intercept of $-K_m$. Also Hanes-Woolf plots were generated for each enzyme separately for liver and muscle and plotted in the same graph.

2.6. Imaging and analysis

2.6.1. Image acquisition

2.6.1.1. TissueFAX

TissueFAX acquisition was performed using a Zeiss Observer Z1 microscope equipped with a stage for 12-slides and a Hamamatsu Photonics Orca flash 4.0 Camera assembled by TissueGnostics, Austria. The Laser was a X-Cite Series 120PCQ and the manual Joystick was provided by Märzhäuser Wetzlar. All images were acquired using the 4.0 slides software by TissueGnostics. Preview settings were adjusted according to the manufacturer's recommendation with a 2,5x objective. Preview was acquired with either scanning in the transmitted light channel on whole slides. Areas containing tissue were selected manually on the basis of visibility. Acquisition was performed using a 20x objective. DAPI, Cy5, FITC and TL filters were used as well as a custom made filter set with a scan range of 440 nm to 750 nm for the detection of CTC. Exposure times were adjusted individually for each channel, but fixed for the whole experiment. Autofocus options used a manual focus search algorithm with variance rough focus measurements. Fine focus was set at HP with x and y to 50%. The utilized focus strategy scanned 3 pictures in height and three pictures in width. The focus point was appointed a floating focus point. The fill focus interval was set after manual focusing around the current z position.

2.6.1.2. Confocal laser scanning microscopy

Confocal microscopy was performed with a Zeiss LSM780 system. 20x/0.8 Plan-Apochromat objective was used. DAPI was detected with 405nm excitation using an argon multiline laser and setting for the detection at 410-460nm with a PMT 1 (371-740nm) filter. CTC-formazan imaging used 488nm excitation with an argon multiline laser and detection at 610-690nm with a Quassar (GaAsP: 416-721 in 8.3nm steps), FITC-labelled antibodies were detected at 488nm excitation (argon multiline laser) and 470-600nm detection (Quassar GaAsP: 416-721 in 8.3nm steps). Alexa647-labelled antibodies were detected at 633 (HeNe Laser, 5mV) excitation and 600-700nm emission (GaAsP: 416-721 in 8.3nm steps). Z stacks were acquired with optimal stepping conditions varying from 0.27-0.35 μ m. Pinhole setting was corresponding with one Airy disc to ensure optimal resolution, laser power was set to 2%. Images were adjusted to full (8 bit) dynamic range. Images were further processed using the Zeiss black software.

2.6.2. Image analysis

2.6.2.1. Colorimetric formazan intensity quantification

For the analysis and quantification of mono- and diformazan formation, the HistoQuest 4.0.4.0150 software (TissueGnostics GmbH, Vienna, Austria) was used. Formazan intensities were analyzed in the various shapes 2.0 mode detecting area (μ m²), mean intensity and sum intensity. The color picker tool was used to individually recognize monoformazan (pink shades) and diformazan (purple shades) formation. Diformazan was appointed as a master marker. Setting were saved as a template and reused for all subsequent experiments.

2.6.2.2. Manually merging bright field and fluorescent images

TissueGnostics does not provide a solution to combine bright field and fluorescent images yet, therefore primary pictures were handled using the freeware „Image J“ (provided by NIH). The goal was to overlay the bright field picture carrying the information of enzymatic activities with a nuclear stain and data from two

fluorescent channels. All images were acquired in “scanned RGB” mode. This introduced the problem that the pixels in the single fluorescent channel images were polluted by intensity values from the other base color values. To avoid this, RGB signal fluorescent channel images were converted into 16-bit greyscale images. Subsequently, the greyscale images were converted to pseudo-color by performing RGB-merge selecting the appropriate channel and “none” for the other channels. Subsequently, the BF image was kept in color format and the pixels of fluorescent images were mathematically added (**Figure 5 A-D**). Consecutive overlay of the different color channels created a pseudo-image in which all information was displayed in one merged picture (**Figure 5 D**).

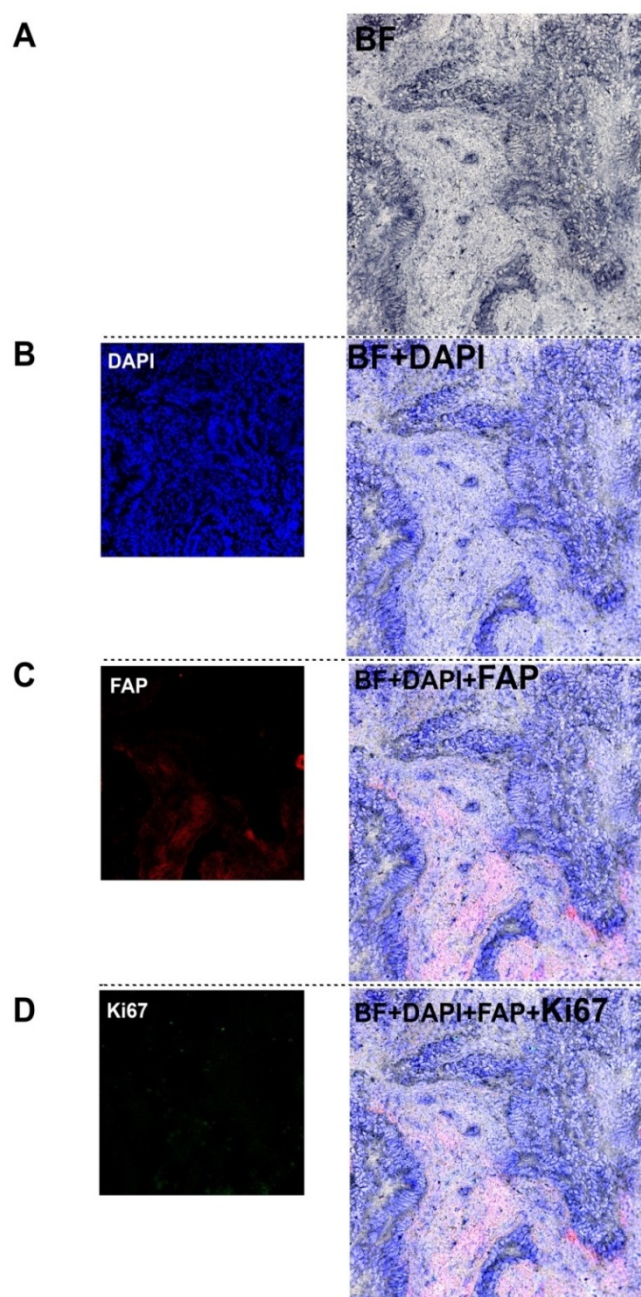


Figure 5. Overlay of bright field and fluorescent images using „Image J“. Images of colon cancerous tissue were acquired with the TisseFAX system, using the same camera and resolution taken in “scanned RGB” mode yielding RGB color images of the single channel fluorescent data. After RGB signal fluorescent channel images were converted into greyscale and recombined in pseudo color, the BF image was kept in color format and the pixels of fluorescent images were mathematically added in sequence (A-D). Consecutive overlay of the different color channels created a pseudo-image in which all information is displayed in one merged picture (D).

2.7. Organotypic co-cultures

2.7.1. Isolation of human peripheral blood mononuclear cells, macrophage differentiation and polarization

18ml of human blood was drawn from the peripheral vein from a healthy volunteer and blood was diluted 1:2 with PBS. Leukocytes and mononuclear cells were separated using Leucosep density gradient centrifugation according to the instructions manual. The buffy coat was collected and further purified using MACS CD14 MicroBeads. Briefly, the cell suspension was centrifuged at 300 x g for 10 minutes and the supernatant was discarded. The cell pellet was resuspended in 160µl of MACS buffer each, 40µl of CD14 MicroBeads was added. After mixture and incubation at 4°C for 15 minutes, cells were washed in 2ml of MACs buffer and centrifuged for 10 minutes at 300 x g. The supernatant was discarded and cells were resuspended in 500µl buffer. For the magnetic separation, the column was prepared by rinsing with 500µl of MACS buffer before the cell suspension was added. Unlabeled cells that passed through were collected by washing the column with 3 x 500µl of MACS buffer. The column was removed from the separator and placed onto a sterile collection tube. 1ml of MACS buffer was pipetted onto the column to flush out the magnetically labeled cells, another washing step with 1ml MACS buffer was performed. Cells were centrifuged for 10 minutes at 300 x g, the cell pellet was resuspended with 3ml of RPMI-1640, supplemented with 20% FBS, 1% Penicillin/Streptomycin and 20ng/ml h-MCSF. The isolated cells were seeded into a 10 cm dish and incubated for five minutes at 37°C/ 5% CO₂ to remove contaminating platelets. Afterwards, the supernatant was taken and seeded in three 24-well plate wells, 1 ml each. To remove remaining lymphocytes, after four hours of incubation the culture plate was gently shaken and the medium was replaced. On day 5, the cells in one well of the cell culture were stimulated with 40ng/ml LPS, the other cells were left naïve, one well was used to determine the cell number. The next day, cells were harvested after washing two times with 500µl PBS and addition of 300µl trypsin for 50 minutes at room temperature while gently shaking. After addition of 500µl of medium, cells were centrifuged for 7 minutes at 300 x g, the pellet was resuspended in 40µl of RPMI-1640 20% FBS, 1% Penicillin/Streptomycin and 20ng/ml h-MCSF.

2.7.2. Assembly of organotypic 3D co-cultures on collagen gels

Addition of differentiated primary human monocytes and cultured primary CAFs in organic collagen co-cultures was based on the protocols by Dolznig et al (Dolznig et al., 2011). Silicone gel casting devices with holes of 0,5 cm diameter were arranged in 6-well cell culture dishes. Cells were counted and 3×10^4 macrophages and 1×10^5 CAFs were prepared in eppis. After centrifugation for four minutes at 1000 rpm, the supernatant was removed. All steps of the collagen gel preparation were performed on ice. Collagen solutions were prepared by mixing 0,1 mL of $10 \times$ PBS, 0.5 mL of 2mg/ml collagen I and 400 μ l of DMEM, the pH was adjusted with 7 μ L of 1M NaOH. The solution was mixed carefully and 300 μ L of the collagen solution was transferred into the tubes already containing the cell pellets, which were gently resuspended. Then, the cell-collagen suspension was transferred into the silicone gel casting devices. After polymerization of the collagen solution for 30 minutes at 37°C/5% CO₂, the silicone was removed and the gels were covered in DMEM. After 24 hours, gels were transferred to a six-well plate. Subsequently, $1,25 \times 10^6$ HTC-116 cells - a human colon cancer cell line - per well were carefully distributed on top of the gels (**figure 6**). After overnight incubation at 37°C/5% CO₂, an autoclaved metal grid was placed in a six-well cell culture dish, on top of that a sterile mesh was placed in the middle of the grid. 3ml of Medium was added to each dish, gels were transferred on top of the mesh. Further medium was added until gels were appropriately covered. Co-culture-gels were incubated for 10 days and then embedded in O.C.T containing medium and finally snap frozen in 2-methyl butane.

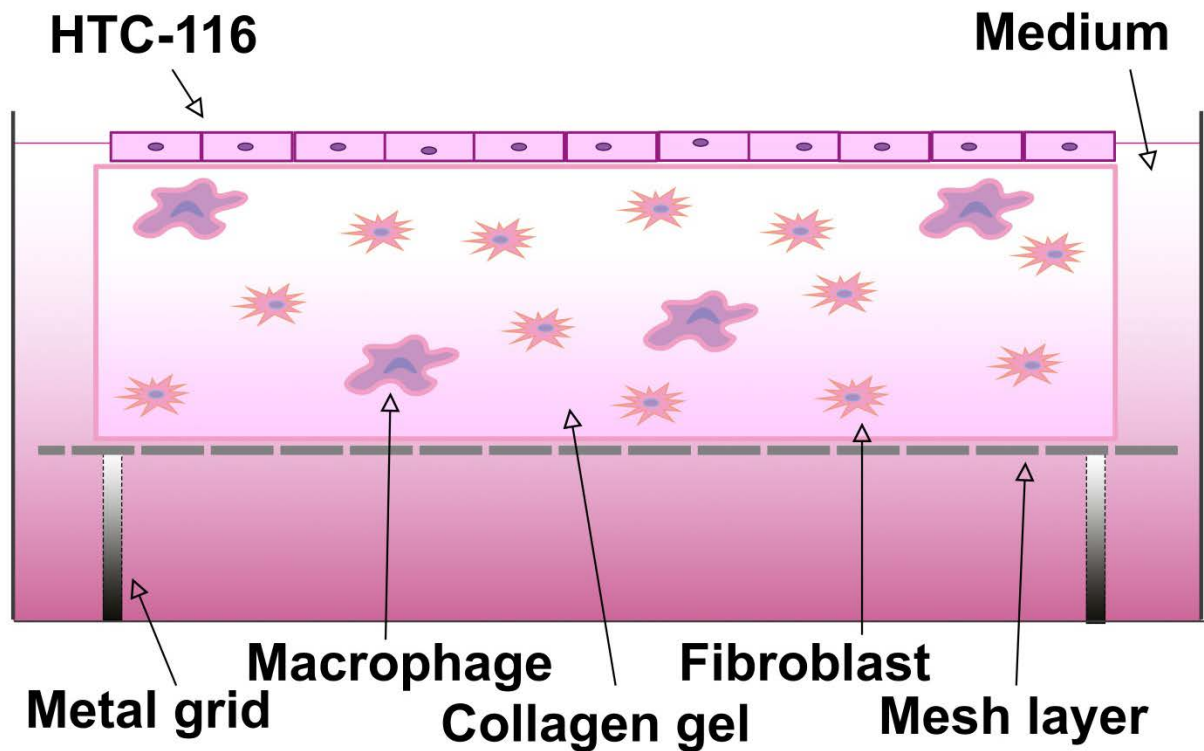


Figure 6. Assembly of organotypic co-cultures. Primary CAFs from colon cancer tissue were grown alone, or together with primary macrophages in collagen gels. After polymerization, the gels were transferred to 6-well plates and placed on mesh layers. Subsequently, HCT-116 colon cancer cells were carefully distributed on top of the gels. Co-cultures were incubated for 10 days.

2.8. Ethics

All animal experiments were carried out according to an ethical animal license protocol and contract approved by the Medical University Vienna (BMWF-66.009/0140-II/10b/2010). Patient samples were collected and handled according to an ethical license protocol approved by the Medical University Vienna (EK Nr. 1374/2014).

3. Results

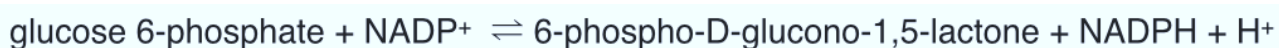
3.1. Establishing a method to decipher metabolic landscapes

3.1.1. Dehydrogenase activity stainings reveal different biochemical properties of metabolic enzymes in liver and muscle

Different organs such as liver, muscle and adipose tissue perform different metabolic tasks to fulfill the assigned energetic needs. I hypothesized, that enzyme histochemical detection of dehydrogenase activity is an appropriate tool to reveal such metabolic differences. In order to verify this hypothesis, the kinetic properties of G6PD were determined in the metabolically distinct environment of liver and muscle tissues.

3.1.1.1. G6PD activity

G6PD is the first and rate limiting enzyme of the oxidative branch of the pentose phosphate pathway (PPP) which catalyzes the following reaction:



Reaction scheme 2.

To determine the biochemical properties of G6PD with enzyme histochemistry, I analyzed the dose response to G6P with NADP⁺ as a coenzyme in liver and muscle cryosections (**Figure 7**). In both tissues, the color of the staining varied from light pink to dark purple according to the reduction state of NBT (Altman, 1974). Formazan formation was quantified as intensity per μm^2 on images acquired with a 20x objective. In liver as well as in muscle tissue identification of monoformazan (pink shades) and diformazan (purple shades) was performed separately by selectively quantifying the individual color ranges. The substrate control reaction (no G6P) displayed monoformazan, but no diformazan formation (highlighted in green) (**Figure 7 A and G**). In contrast to this, in both tissues addition of 15 mM G6P resulted in a strong pink and partly purple staining (**Figure 7 B and H**).

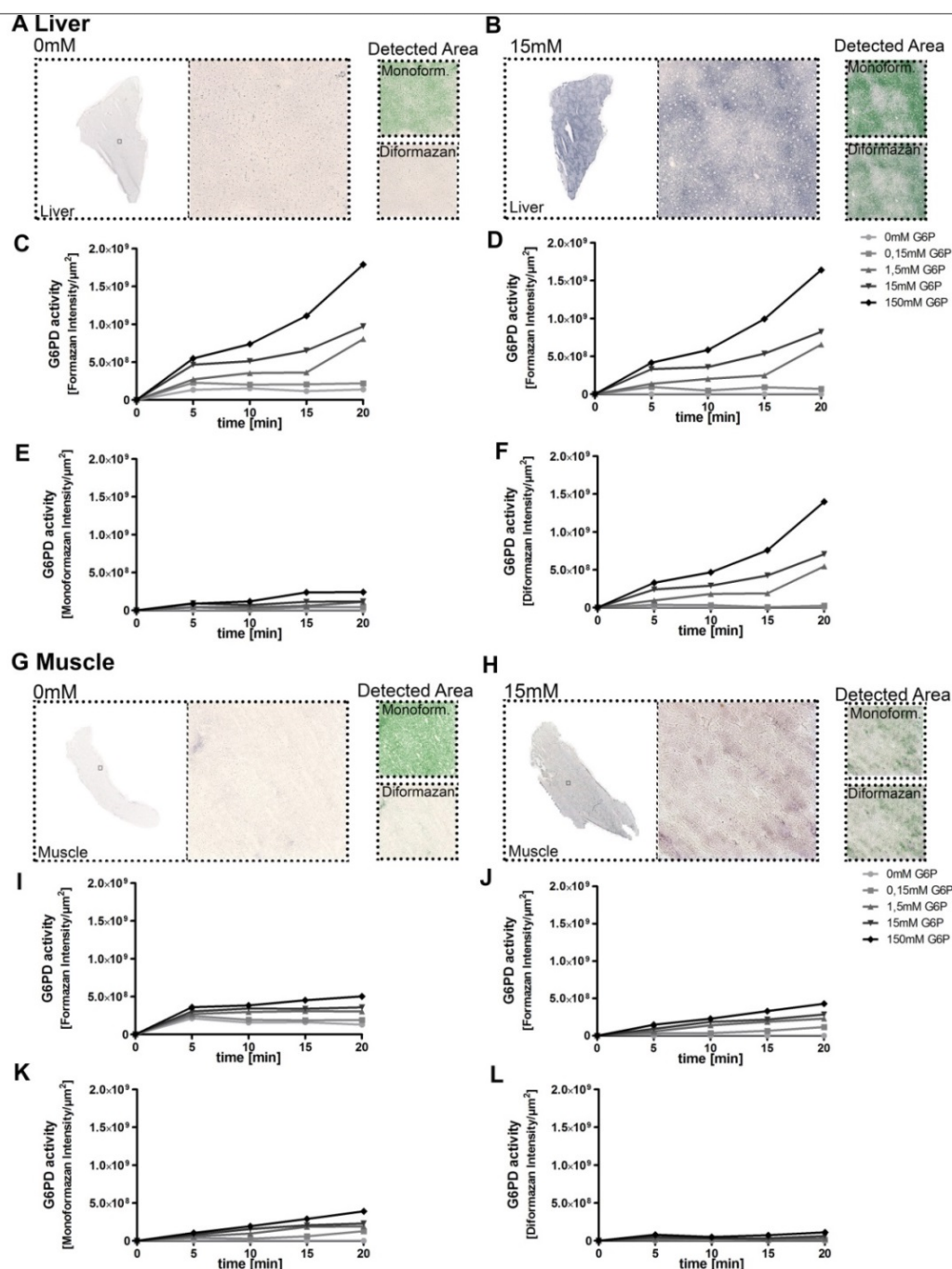


Figure 7. G6PD activities in mouse liver and muscle. Different G6P concentrations (0 mM , 0,15 mM, 1,5 mM, 15 mM and 150 mM) were incubated for the time course of 5, 10, 15 or 20 minutes on liver (A-F) and muscle (G-L) tissue sections. Staining was performed without substrate addition (A, G) and upon addition of 15 mM G6P (B, H). Whole tissue sections were acquired with a 20x objective. Computational image analysis detected monoformazan and diformazan formation separately (highlighted in green). Formazan intensity/μm² before (C and I) and after (D and J) normalization to the substrate-free control reaction was plotted as well as the formation of mono- (E and K) and diformazan (F and L). Data represents mean values of three replicates per time point and per concentration.

Compared to liver, the overall staining in muscle was much weaker showing decreased monoformazan and diformazan production and therefore less G6PD activity (**Figure 7 H**).

To establish the kinetic properties of G6PD in both tissues, liver and muscle were incubated with increasing substrate concentrations (0 mM, 0,15 mM, 1,5 mM, 15 mM and 150 mM) in a time course of 5, 10, 15 and 20 minutes. In liver, a substrate dependent increase in G6PD activity was measured over the time course of 20 minutes (**Figure 7 C**). Subsequently, the substrate dependent increase in G6PD activity was normalized by subtraction of the intensities measured in the substrate control reaction (background), which resulted in comparable results (**Figure 7 D**). Compared to diformazan formation, the formation of monoformazan appeared as a weak overall staining and showed moderate increase in intensity (**Figure 7 E and F**). In muscle, the dose dependent increase in G6PD activity was also time dependent (**Figure 7 I**). Upon subtraction of the intensities of substrate control reactions, the increase in G6PD activity appeared also time and dose dependent (**Figure 7 J**). Other than in the liver, separate analysis of mono- and diformazan formation indicated a dose-dependent increase in monoformazan, but not in diformazan formation (**Figure 7 K - L**).

To confirm the specificity of the G6PD activity staining, G6PD activity in liver and muscle tissue was analyzed in the presence of the specific inhibitor DHEA (**Figure 8**). Compared to stainings without DHEA addition, G6PD activity was reduced up to approximately 90% in the presence of 60 mM DHEA for the time course of 20 minutes.

Based on the time dependent dose responses of G6PD activity, Michaelis-Menten kinetics and Hanes-Woolf plot were calculated to further define the biochemical properties of liver and muscle G6PD (**Figure 9**). Between both tissues, the curve shape as well as slope of the reaction velocity versus G6P concentration showed great differences and revealed major differences in K_M and V_{max} . As compared to G6PD activity in muscle, liver G6PD exhibited a relatively high V_{max} of $7,9 \times 10^7$ mM/ $\mu\text{m}^2/\text{min}$ and K_M of 10,6 mM, whereas in muscle V_{Max} was only $1,8 \times 10^7$ and K_M only 0,6 mM/ $\mu\text{m}^2/\text{min}$.

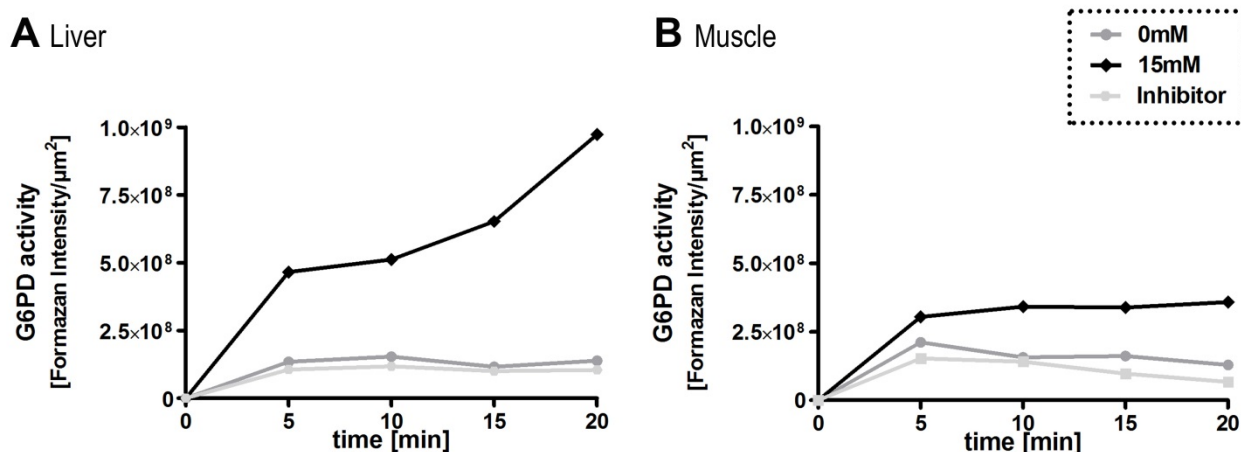


Figure 8. G6PD inhibition in liver and muscle tissue. Time dependent G6PD activity upon addition of no substrate (0 mM), 15 mM G6P or supplemental addition of 60 mM DHEA as an enzyme specific inhibitor in liver (A) and muscle (B). Data represents mean value of three replicates per time point and concentration.

For the calculation of enzyme kinetic parameters with the Hanes-Woolf plot, the ratio of the initial substrate concentration to the reaction velocity was plotted against the substrate concentration. The results from the Michaelis-Menten kinetic analysis and Hanes-Woolf plotting showed comparable results. G6PD activity in liver exhibited a relatively high V_{\max} of $7,9 \times 10^7$ mM/ $\mu\text{m}^2/\text{min}$ and K_M of 5,7 mM whereas in muscle V_{\max} was only $2,1 \times 10^7$ and K_M only 2,2 mM/ $\mu\text{m}^2/\text{min}$.

Overall, in both tissues G6PD activity increased over time with increasing substrate concentrations. The detected activity was specific, as it was severely inhibited by addition of DHEA. Moreover, substrate response of liver and muscle G6PD was different and appeared higher in liver than in muscle. Therefore, enzyme histochemistry was able to reveal the known differences in G6PD biochemical properties. To further validate the applicability for other enzymes, biochemical properties of GAPDH, LDH, IDH and SDH were also determined.

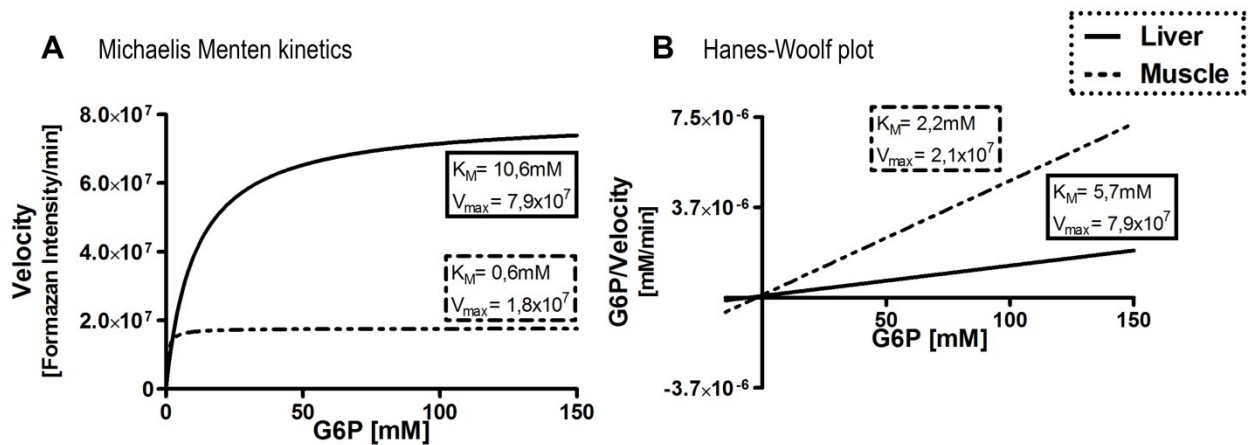
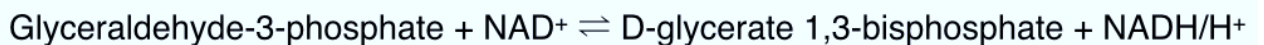


Figure 9. Michaelis-Menten kinetics (A) and Hanes-Woolf plot (B) of G6PD in mouse liver and muscle. Results of V_{max} calculation are in the same range whereas calculations of K_M vary between the evaluation methods. Data represents mean value of three replicates.

3.1.1.2. GAPDH activity

Following the same principle as the enzyme histochemical detection of G6PD, GAPDH activity was determined. Glycolytic GAPDH catalyzes the following reaction:



Reaction scheme 3.

GAPDH is known to be a reversible metabolic switch under oxidative stress and serves as an important regulator for the cellular redox balance (Agarwal et al., 2012). Upon oxidative stress, cells demand increased amounts of NADPH, mostly provided by G6PD through reduction of NADP^+ . In yeast, enhanced levels of oxidative stress have been shown to reduce GAPDH activity, redirecting metabolic flux from glycolysis to the oxidative branch of the PPP (Ralser et al., 2007).

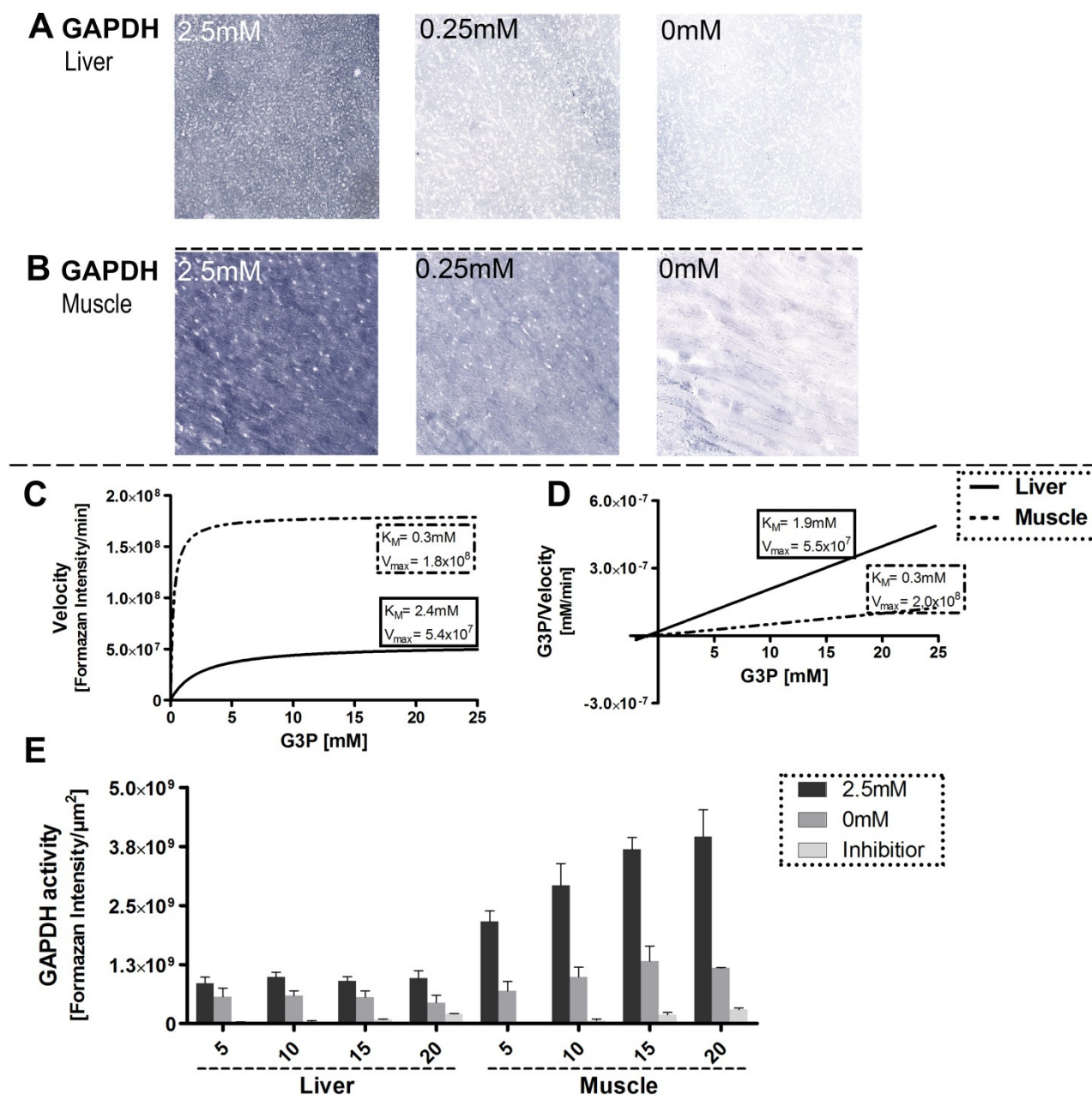


Figure 10. Kinetic analysis of GAPDH in mouse liver and muscle. GAPDH activity was determined upon addition of 2.5 mM, 0.25 mM and 0 mM G3P in liver (A) and muscle (B) cryosections. A dose response over time was used to calculate Michaelis-Menten kinetics (C) and Hanes-Woolf Plot (D). Addition of 40 mM iodoacetate inhibited the formation of formazan up to 20 minutes of incubation (E). Pictures were taken with 20x objective. Data represents mean value of three replicates; error bars indicate standard deviation.

In liver and muscle, addition of G3P induced a dose dependent enhancement in GAPDH activity staining (**Figure 10 A and B**). Michaelis-Menten analysis revealed a V_{\max} of $5,4 \times 10^7$ mM/ $\mu\text{m}^2/\text{min}$ for liver GAPDH, which is only approximately 30% of the V_{\max} of muscle GAPDH (**Figure 10 C**). Analogous, the K_M of liver GAPDH had a value of 2,4 mM, whereas muscle GAPDH K_M was only 0,3 mM. Using the Hanes-Woolf plot, resembling values were calculated (**Figure 10 D**). To confirm specificity of the GAPDH activity staining, GAPDH activity in liver and muscle was demonstrated in presence of iodoacetate as an inhibitor (**Figure 10 E**). Compared with stainings in absence of iodoacetate, GAPDH activity was reduced to approximately 10% in both tissues upon addition of the inhibitor.

3.1.1.3. LDH activity

Five different isoenzymes of LDHs are described in the literature. LDHs are tetramers composed of different protein subunits called M (muscle) or H (heart). The different isoenzymes contain different tissue-specific subunits which can be distinguished due to their physical (molecular weight, isoelectric point) and catalytical (K_M , pH optimum) properties. All isoenzymes catalyze the same reaction:



Reaction scheme 4.

The conversion of glycolytic pyruvate to lactate is mostly catalyzed upon hypoxic conditions and the reverse reaction is performed during the Cori cycle in the liver. Elevated lactate concentrations inhibit the catalysis of pyruvate to lactate so it is possible to determine LDH activity with lactate as a substrate (Spriet et al., 2000). LDH is best known to be deregulated in cancerous cells. As mentioned before, many cancer cells depend on the Warburg effect converting glucose to lactate even under normoxic conditions to fulfill the molecular needs of cellular proliferation rather than energy homeostasis (Warburg et al., 1927).

In liver and in muscle tissue, addition of lactate induced a dose dependent increase in LDH activity (**Figure 11 A and B**).

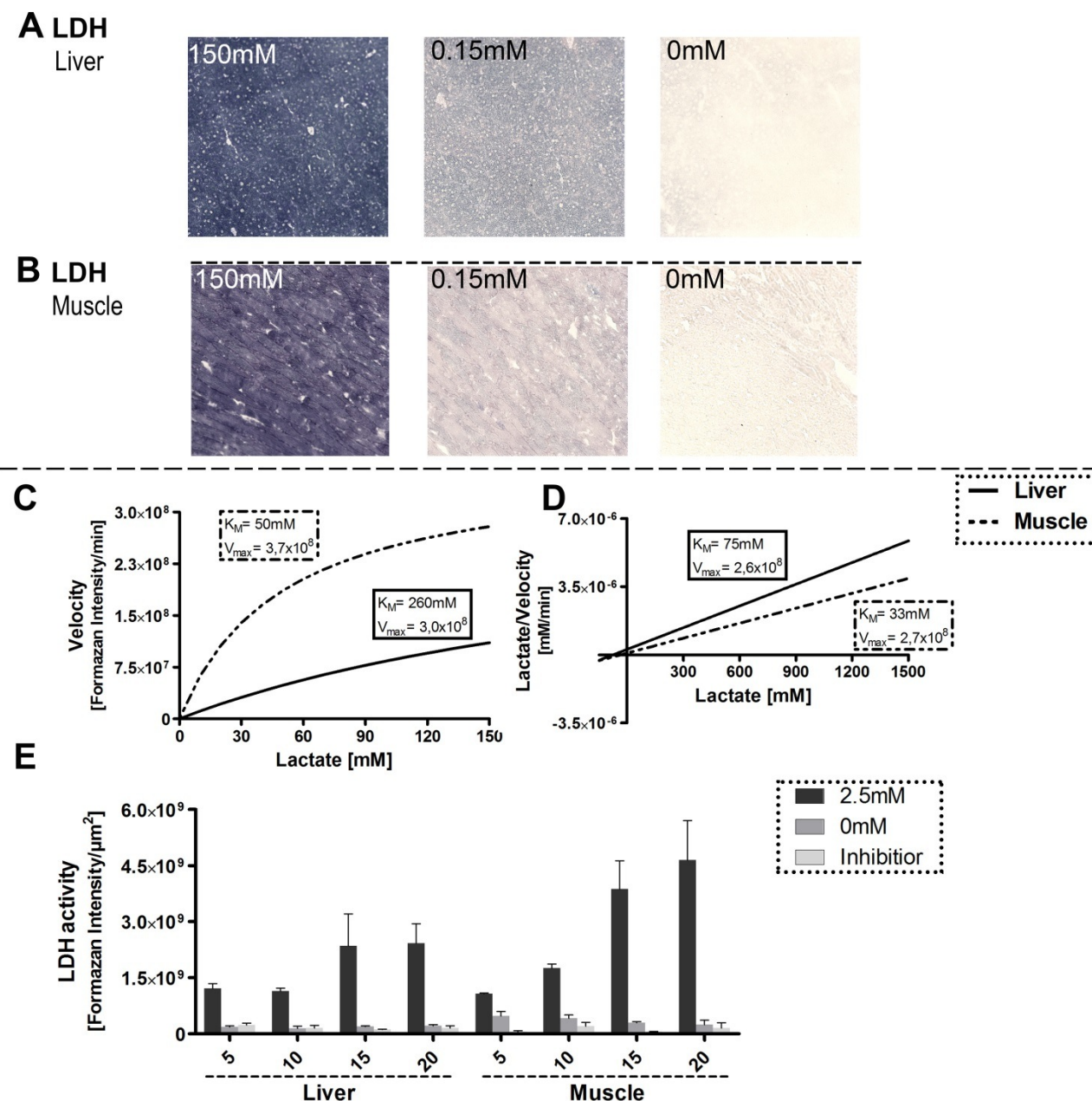
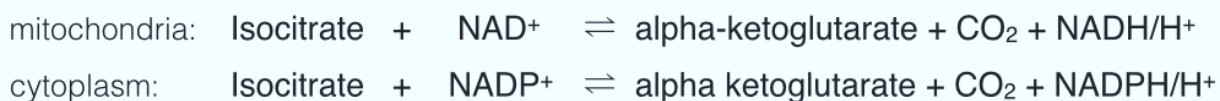


Figure 11. Kinetic analysis of LDH in mouse liver and muscle. LDH activity was determined upon addition of 150 mM, 15 mM and 0 mM lactate in liver (A) and muscle (B) cryosections. A dose response over time was used to calculate Michaelis-Menten kinetics (C) and Hanes-Woolf Plot (D). Addition of 200 mM sodium oxamate inhibited the formation of formazan up to 20 minutes of incubation (E). Pictures were taken with 20x objective. Data represents mean value of three replicates; error bars indicate standard deviation.

Michaelis-Menten kinetic analysis revealed a liver LDH V_{\max} of $3,0 \times 10^8$ mM/ μm^2 /min and an only approximately 20% higher V_{\max} for muscle LDH of $3,7 \times 10^8$ mM/ μm^2 /min (**Figure 11 C**). In contrast to that, liver K_M was 260 mM but muscle LDH had a K_M of only 50 mM. The Hanes-Woolf plot confirmed the range of those values (**Figure 11 D**). Taken together, liver and muscle LDH had similar maximum reaction velocities, but liver LDH required five times the amount of substrate than muscle LDH to reach the same reaction rate. Again, to determine the specificity of the LDH activity detection, addition of the enzyme specific inhibitor sodium oxamate was demonstrated in liver as well as in muscle tissue (**Figure 11 E**). In both tissues, addition of 200 mM sodium oxamate severely inhibited LDH activity up to 15 minutes of incubation time.

3.1.1.4. IDH activity

IDH catalyzes the oxidative decarboxylation of isocitrate, which forms alpha-ketoglutarate and CO_2 . This process involves oxidation of isocitrate to oxalosuccinate, followed by the decarboxylation of the carboxyl group beta to the ketone. In humans and mice, IDH exists in three isoforms: The isoforms IDH1 and IDH2 catalyze the reaction using NADP^+ as a cofactor. IDH3 catalyzes the reaction in the citric acid circle while converting NAD^+ to NADH in the mitochondria. Due to the high negative free energy change, it is one of the irreversible reactions in the citric acid cycle.



Reaction scheme 5.

IDH isoform distinction can be accomplished by addition of cofactors that are specific for the compartment that the isoform is located in. Also, the choice of electron carrier is a valuable tool to specify the reaction. In liver as well as in muscle tissue, kinetic analysis was performed using NAD^+ as a cofactor and phenazine methosulfate as an electron carrier to measure the activity of mitochondrial IDH.

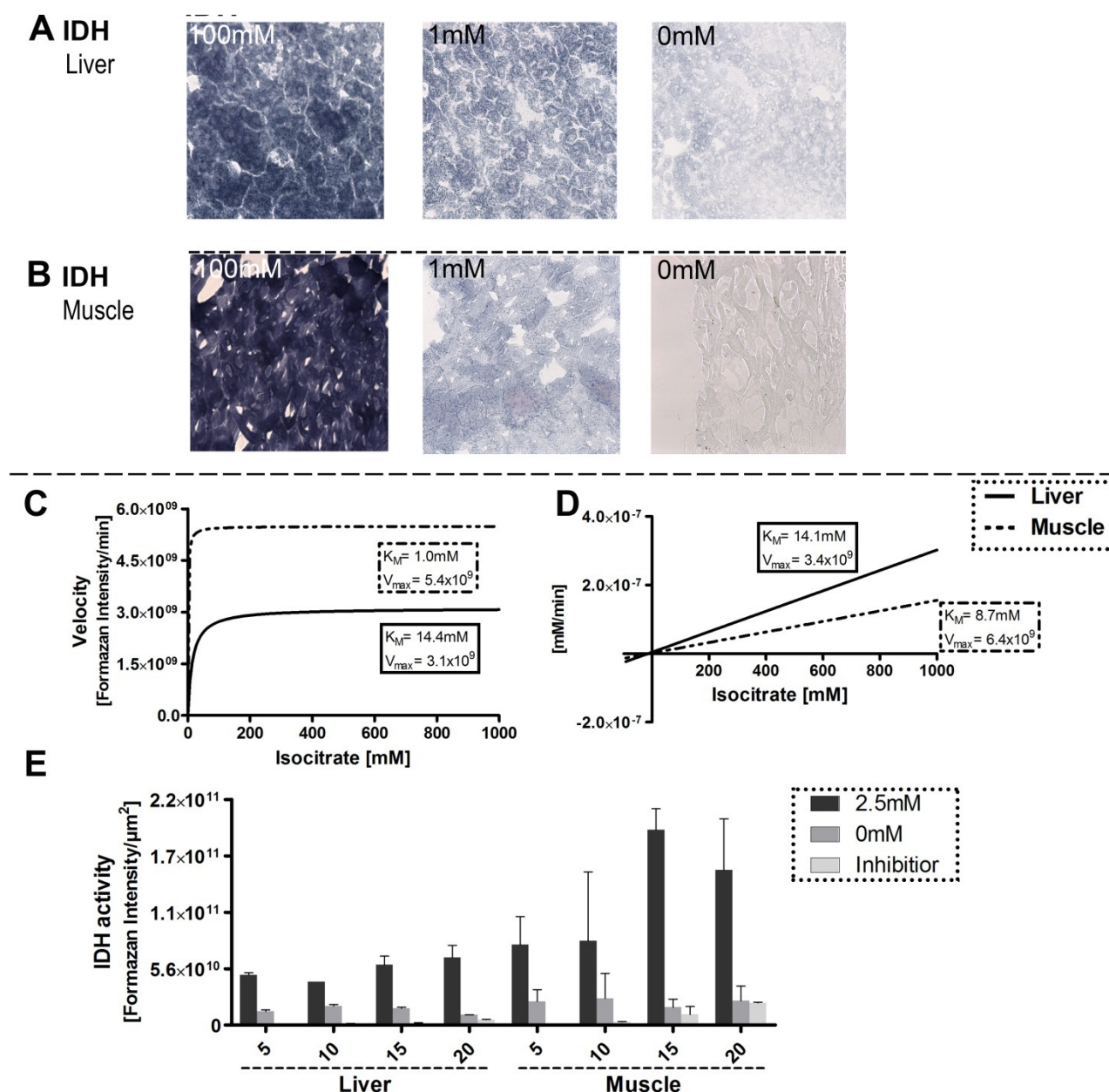


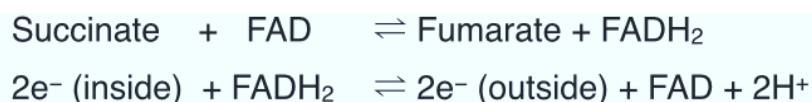
Figure 12. Kinetic analysis of IDH in mouse liver and muscle. IDH activity was determined upon addition of 100 mM, 1 mM and 0 mM isocitrate in liver (A) and muscle (B) cryosections. A dose response over time was used to calculate Michaelis-Menten kinetics (C) and Hanes-Woolf Plot (D). Addition of 250 mM oxaloglycine inhibited the formation of formazan up to 15 minutes of incubation (E). Pictures were taken with 20x objective. Data represents mean value of two replicates; error bars indicate standard deviation.

Addition of isocitrate induced a dose dependent increase in LDH activity in liver and in muscle tissue (**Figure 12 A and B**).

Michaelis-Menten kinetics revealed an approximately 40% lower V_{\max} of liver IDH ($3,1 \times 10^9$) compared to muscle. Whereas liver IDH had a K_M of 14,5 mM, muscle IDH had only a K_M of 1 mM (**Figure 12 C**). Hanes-Woolf Plot showed slightly aberrant results, with the similar K_M -range of liver IDH but a higher K_M for muscle IDH (**Figure 12 D**). Therefore, liver IDH had only half of the maximum reaction rate compared to muscle IDH. Especially when dealing with an enzyme of different isoforms in different cellular compartments, estimation of the specificity of the detection method is very important. To confirm specificity of the IDH activity staining we used oxaloglycine as an inhibitor for mitochondrial IDH. In both tissues, addition of isocitrate induced an uniform IDH activity over time which was completely blocked by the addition of 250 mM oxaloglycine up to 15 minutes of incubation (**Figure 12 E**).

3.1.1.5. SDH activity

SDH or respiratory complex II is an enzyme complex localized at the inner mitochondrial membrane which participates in the citric acid cycle and the electron transport chain. SDH catalyzes the oxidation of succinate to fumarate with simultaneous reduction of ubiquinone to ubiquinol:



Reaction scheme 6.

In contrary to the previously described mechanisms, reduction of NBT to its formazan does not occur via a direct interaction of reduced NAD(P). The primary reaction catalyzed by SDH is succinate oxidation via the flavin adenine dinucleotide (FAD) which is reduced to FADH_2 .

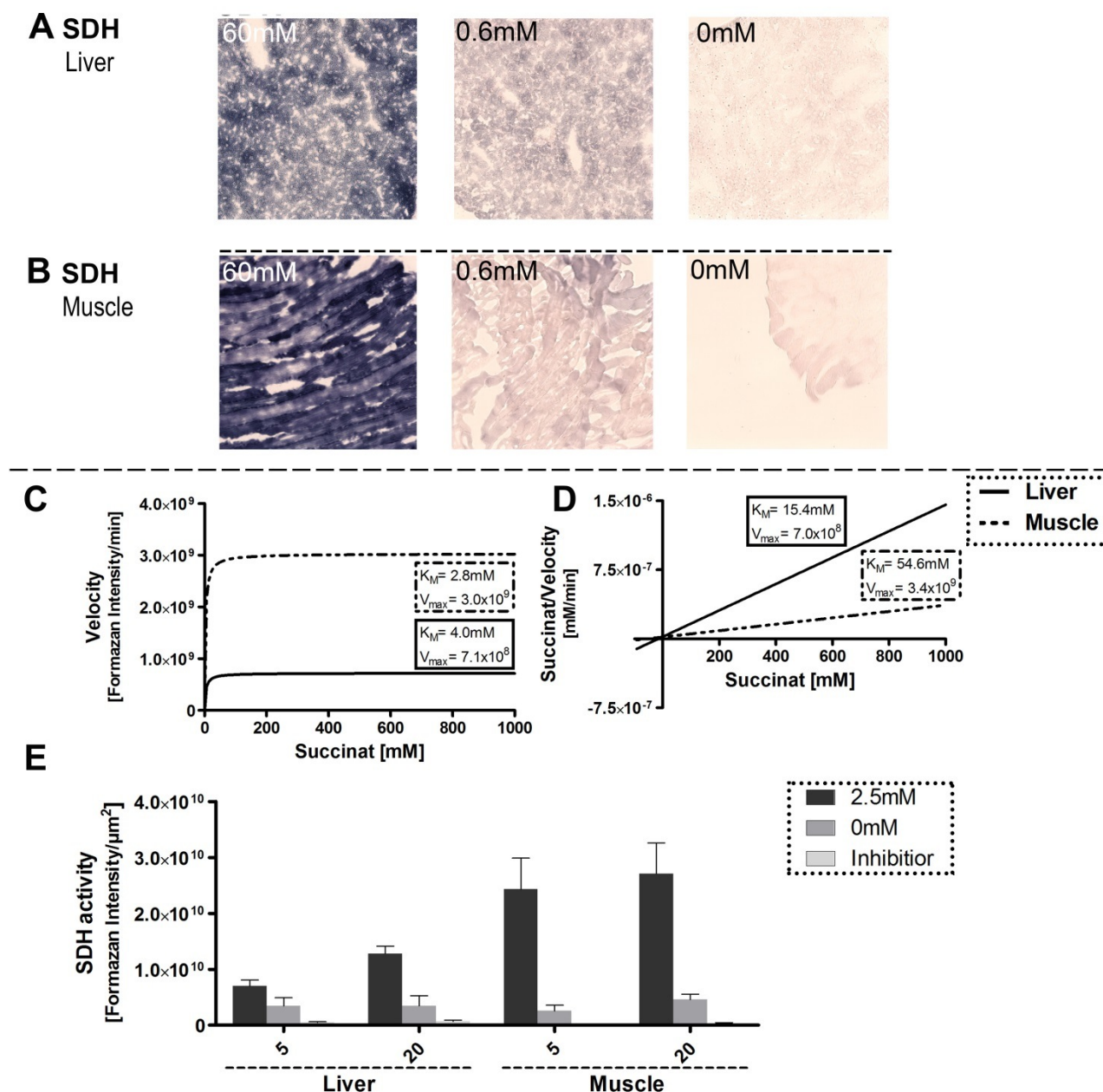


Figure 13. Kinetic analysis of SDH kinetics in mouse liver and muscle. SDH activity was determined upon addition of 60 mM, 6 mM and 0 mM succinate in liver (A) and muscle (B) cryosections. A dose response over time was used to calculate Michaelis-Menten kinetics (C) and Hanes-Woolf Plot (D). Addition of 250 mM malonate inhibited the formation of formazan up to 20 minutes of incubation (E). Pictures were taken with 20x objective. Data represents mean value of two replicates; error bars indicate standard deviation.

FADH₂ is involved in the electron transport across the mitochondrial membrane and while the electrons are subsequently transferred to an ubiquinone molecule, FADH₂ is reoxygenated to FAD. Then, the redundant H⁺ can reduce NBT to its formazan state. In liver and muscle tissue, addition of succinate induced SDH activity in a dose dependent manner (**Figure 13 A and B**).

In liver, Michaelis-Menten analysis of SDH activities revealed a very low V_{\max} of 7.1×10^8 mM/ μm^2 /min which is only 23% of the muscle V_{\max} (**Figure 13 C**). However, the Michaelis-Menten constant for liver SDH had a value of 4 mM and the muscle SDH K_M was in a comparable range. The Hanes-Woolf diagram showed a notable difference in the calculations of K_M of liver and muscle SDH. Whereas liver SDH had a K_M of 15,4 mM, muscle SDH had a K_M of 54,6 mM (**Figure 13 D**). Malonate was added to the reaction as an inhibitor to verify the specificity of the SDH activity staining method (**Figure 13 E**). In both tissues, addition of 250 mM malonate severely inhibited SDH activity up to 20 minutes of incubation time (**Figure 13 E**).

Taken together, determination of biochemical properties of G6PD, GAPDH, LDH, IDH and SDH with enzyme histochemistry was able to reveal differences in V_{\max} and K_M between muscle and liver tissue. The specificity of the activity measurements was further validated with the use of enzyme specific inhibitors. The determination of the described five metabolic enzymes was considered valid to reveal metabolic configurations in complex tissues.

3.1.3. Combination of the dehydrogenase activity assay with fluorescently labelled antibodies for cell type identification is functional

In order to create metabolic landscapes of complex tissues and to provide information on metabolic wiring within the individual cells, it was crucial to integrate the detection of enzymatic activities with reliable cell type identification. This was accomplished by combining bright field imaging of enzymatic activity with fluorescent labeled antibody-detection of cell types and nuclear DAPI. Pictures were merged as described in material and methods and **Figure 5**.

3.1.4. Substitution of NBT with fluorescent CTC – a great advantage?

In recent years, CTC, a redox dye similar to NBT has become a popular tool for redox-dependent applications such as cell-viability assays (**Figure 14**).

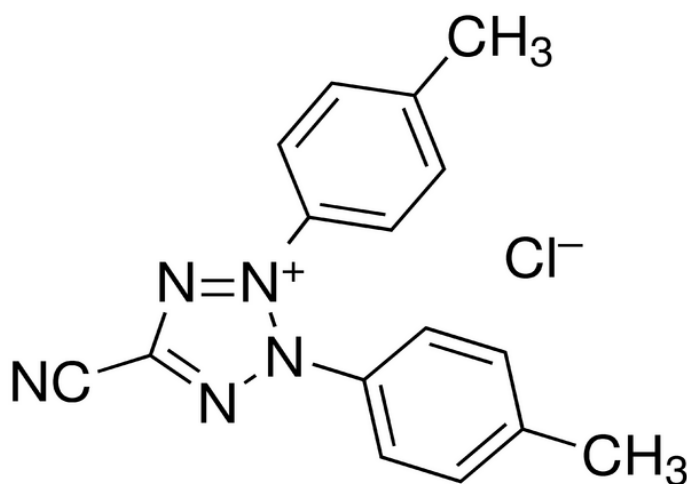


Figure 14. Chemical structure of CTC. CTC is a monotetrazolium redox dye which produces a fluorescent formazan when it is reduced giving rise to a bright red fluorescence when illuminated by long-wave UV light (>350nm).

The dye is of particular interest, because it produces a fluorescent signal after reduction and is has already been applied in flow-cytometric determination of dehydrogenase activities (Frederiks et al., 2006). Replacement of NBT with CTC showed a similar pattern of staining in human healthy colon tissue slices (**Figure 15**). Nevertheless CTC is a sophisticated substitute for NBT, the fluorescent signal was only stable for a short time period (**Figure 15 C**). After two hours, CTC signal strength was reduced about 40% and after three hours, the signal was decreased even approximately 80%.

However, CTC might be used for 3D reconstructions in combination with laser scanning microscopy to determine intracellular localizations of the enzymatic activities. To test this, we measured G6PD activity in 30µm thick mouse liver cryosections with CTC as detection reagent in combination with a fluorescent labelled macrophage specific MAC-2 antibody and DAPI. The acquired image demonstrated co-localization of G6PD activity and the macrophage marker in the x, y and z dimensions (**Figure 16**, indicated by the arrow).

For the analysis of metabolic landscapes in complex tissues, NBT was the preferable detection agent. Nevertheless, CTC clearly had advantages in other methodological approaches.

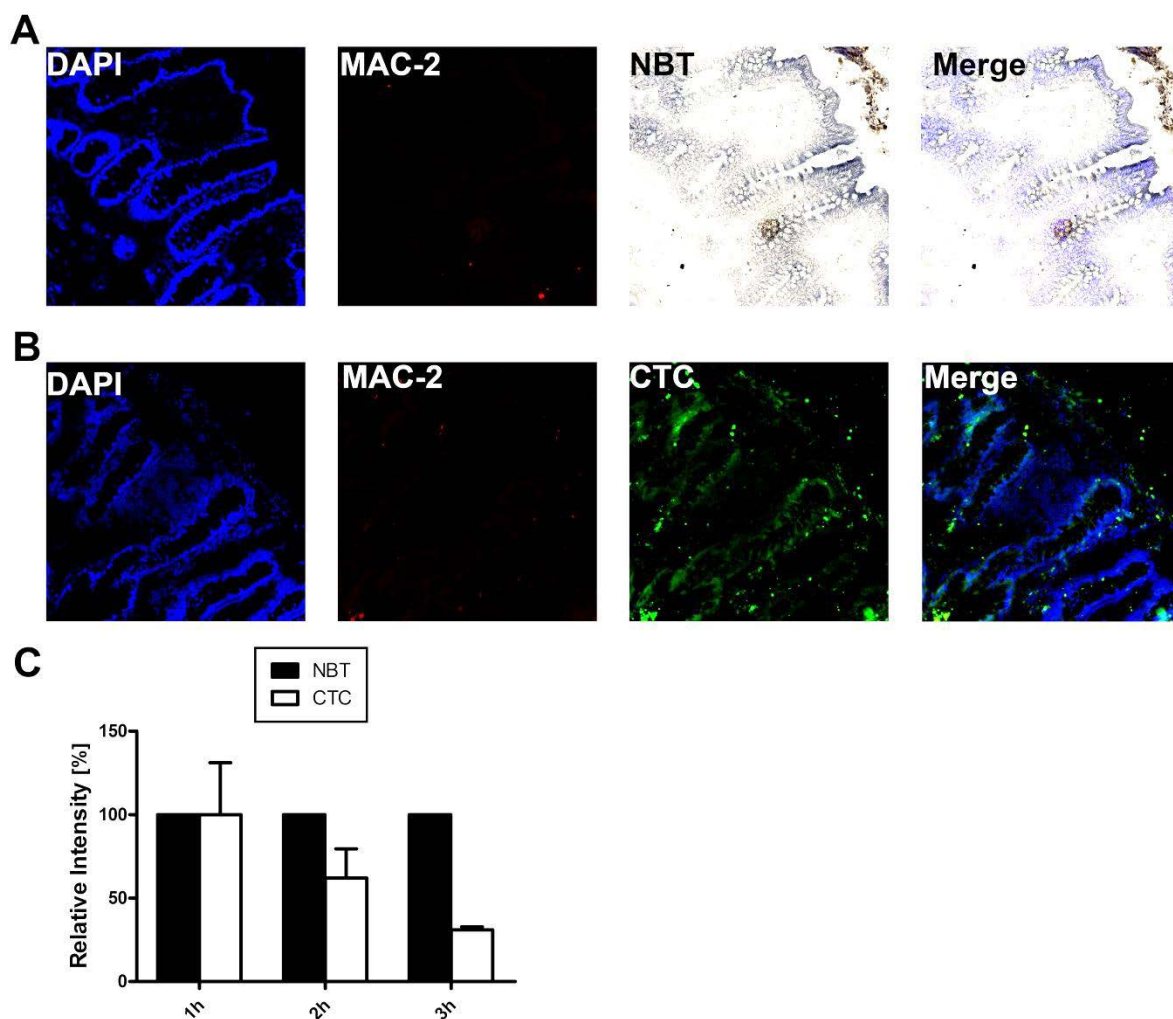


Figure 15. G6PD activity in healthy colon tissue using different redox-dyes.

Either NBT (A) or CTC (B) was used to demonstrate G6PD with subsequent fluorescent DAPI and MAC-2 antibody staining. CTC and NBT intensities were compared over the time course of 3 hours (C). Pictures were taken with 20x objective. Data represent mean value of two replicates, error bars indicate standard deviation.

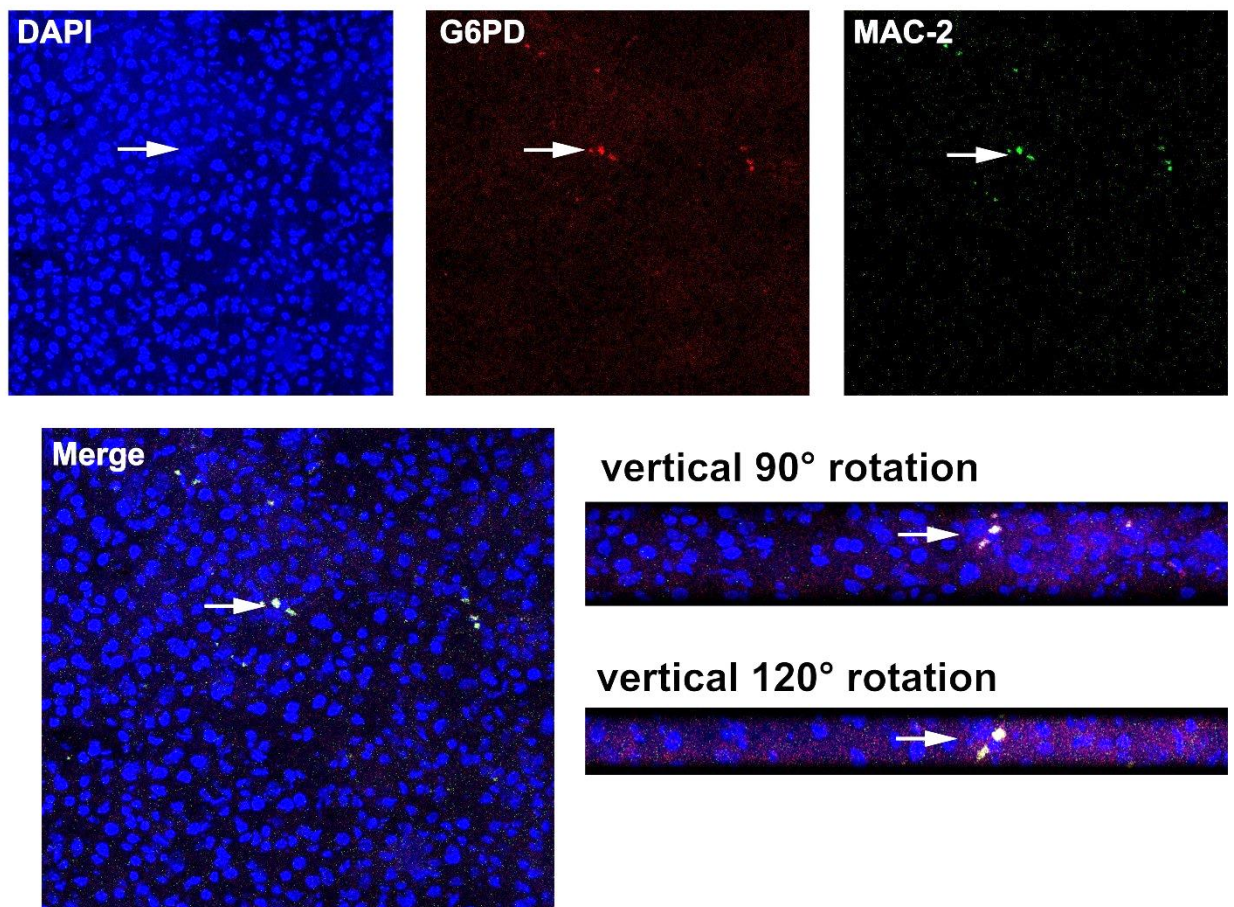


Figure 16. 3D reconstruction of G6PD activity in mouse liver with nuclear DAPI and MAC-2 antibody stain. Z-stacks were taken with confocal laser scanning microscopy. Virtual vertical rotations were performed using the Zeiss black software. Pictures were taken with 20x objective.

3.2. Deciphering metabolic landscapes of different tumor types

Recent studies indicated that not only cancerous cells undergo metabolic adaptations during tumorigenesis, but also associated cells in the tumor microenvironment (Bailey et al., 2012; Chiarugi et al., 2014). To verify that the dehydrogenase method using NBT as a detection agent could reveal such alterations, activity of G6PD, GAPDH, LDH, IDH and succinate SHD were visualized on human lung adenocarcinoma, pleural mesothelioma and colon carcinoma biopsy specimens (**Figure 17**).

Adenocarcinoma of the lung is the most common form of lung cancer and can be histologically distinguished from different cancerous forms through the malignant tissue architectural cytology. This includes gland and duct formation as well as the production of mucus. The overall G6PD activity appeared very high and unevenly distributed throughout the tissue specimen. Cells with high enzymatic activity were clustered together irregularly in the whole tissue (**Figure 17 A**). By contrast, GAPDH activity was rather weak and uniformly spread in the visible cells (**Figure 17 B**). LDH activity was also evenly distributed in the tissue specimen. Some cells showed enhanced enzymatic activity, those cells were clustered in the margins, close to one of the ductile spaces (**Figure 17 C**, indicated by the arrow). In contrast to that, some regions in the tissue specimen showed higher activities of mitochondrial IDH and SDH than others. Cells with particularly high enzymatic activity were rather randomly distributed throughout the specimen (**Figure 17 D and E**).

Pleural mesotheliomas are an unusual form of cancer that origins from the pleura, the mesothelial lining that cover the lungs. Development of pleural mesothelioma is directly linked with exposure to asbestos and the overall survival prognosis is very poor. Histologically, pleural mesothelioma mostly appears as a fibrous tumor, showing cytological atypie such as macronucleoli and enhanced number of cytoplasmatic vacuoles (Inai, 2008). Overall, all detected enzymatic activities appeared very low. However, cells that were close to luminal space showed enhanced G6PD, GAPDH, IDH and SDH activities, but no increased LDH activity (**Figure 17 A-E**).

Colorectal cancer is a widely spread form of cancer and strongly associated with lifestyle factors and age. The tumor mostly emerges from granular epithelia of colorectal mucosa. After invasion of the wall it can infiltrate the muscularis mucosae and submucosa. The cancerous cells itself show irregular tubular structure, formation of lumina and reduced stroma (**Figure 17**). Some cells may secrete mucus which histopathologically appears as empty spaces (Lunnen, 1983). In a biopsy specimen of a human colon carcinoma, G6PD activity exhibited a diverse spectrum of different activities (**Figure 17 A**). Cells that featured strong enzymatic activity appeared as “linings” throughout the tissue (**Figure 17 A**, black arrow). Some cells in the tumor stroma showed particularly high G6PD activity (**Figure 17 A**, indicated by the grey arrow). In the tissue specimen, GAPDH activity also appeared as a lining (**Figure 17 B**, black arrow). Stromal cells revealed an increased enzymatic activity (**Figure 17 B**, grey arrow). The cells in the specimen revealed multiple levels of LDH activity and cells that showed increased activity congregated in particular regions (**Figure 17 C**, indicated by the arrow). IDH activity was elevated in cells that bordered the luminal space (**Figure 17 D**). Also, a lined pattern was revealed in cells that border the stroma (**Figure 17 D**, indicated by the arrow). SDH activity resembled an overall heterogeneous picture (**Figure 17 E**). Again, cells that bordered the stroma showed an increased activity in form of a lined pattern (**Figure 17 E**, indicated by the arrow).

All in all, the combined determination of the chosen five enzymatic activities with NBT as a detection agent was able to reveal distinct metabolic patterns between lung adenocarcinoma, pleural mesothelioma and colon carcinoma tissue specimens as well as between the individual cells of the a specific tumor. Therefore, we concluded that enzyme histochemistry was a valid tool to decipher the metabolic landscapes of complex tissues.

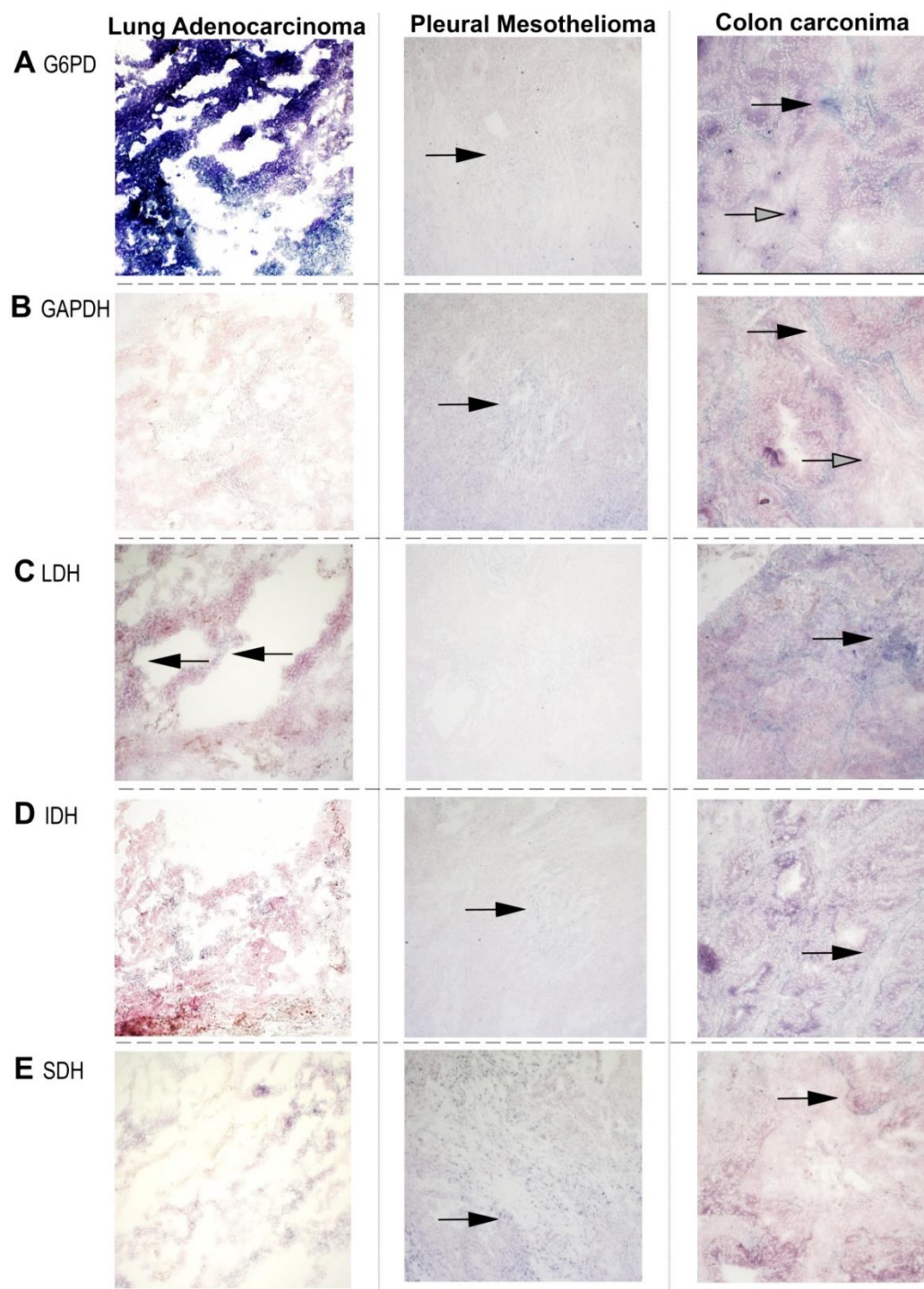


Figure 17. Metabolic landscapes of lung adenocarcinoma, pleural mesothelioma and colon carcinoma. Increased activities of G6PD (A), GAPDH (B), LDH (C), IDH (D) and SDH (E) were found in distinct tissue areas as indicated by the arrows. Pictures were taken with a 20x objective.

3.3. Cell type specific metabolic landscapes of healthy and cancerous colon tissue

The microenvironment of colon carcinoma showed diverse distribution of enzymatic activities so we further compared G6PD and SDH activities in cancerous and healthy colon tissue. As enzymatic activities were analyzed in specimens retrieved from the same patient, we had the unique possibility to directly compare the metabolic wiring in both conditions.

A variety of recent studies indicated a particular role of enhanced G6PD activity for proliferating cancer cells (Du et al., 2013; Hu et al., 2013). As the rate limiting enzyme of the PPP, G6PD is not only involved in nucleotide synthesis but a major contributor to the cellular redox pool by the production of NADPH (Haschemi et al., 2012; Reales-Calderon et al., 2014). SDH activity is regarded a tumor suppressor and its dysfunction has been connected to tumorigenesis in a variety of examples (King et al., 2006). Determination of SDH activity in the tumor microenvironment is also reasonable because of its possible role in cellular activation. Oxidative metabolism is known to be reduced upon macrophage activation, but in activated fibroblasts SDH activity seems to be elevated (King et al., 2006; Tannahill et al., 2013).

The tissue specimens were analyzed with a combination of fluorescent DAPI staining, the proliferation marker Ki67, the macrophage marker MAC-2 and the fibroblast activation protein marker FAP.

3.3.1. Activity of G6PD

In healthy colon tissue G6PD activity was especially located in the apical side of external epithelial cells. The lamina propia did not show visible activity of G6PD (**Figure 18 A and B**). Cells that were positive for the proliferation marker Ki67 were also located at the utter epithelial cell layer. There were almost no MAC-2 positive and no FAP positive cells visible in healthy colon tissue (**Figure 18 A and B**).

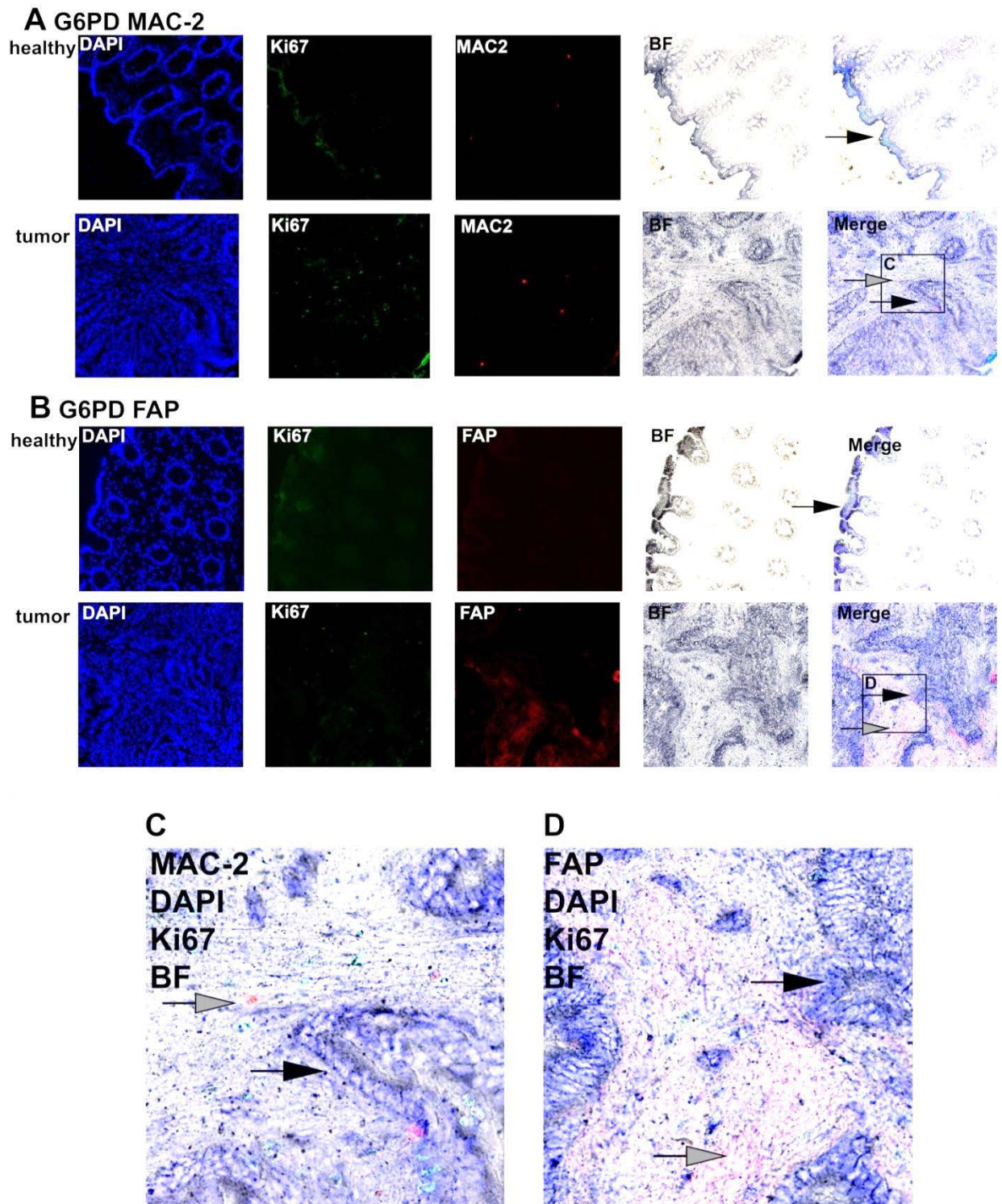


Figure 18. G6PD activity in healthy and cancerous colon tissue. G6PD activity (bright field, BF) was determined in combination with nuclear DAPI stain (blue), proliferation marker Ki67 (green), MAC-2 (red, A and C) or fibroblast activation protein FAP (red, B and D). Pictures were taken with a 20x objective. Metabolically distinct areas are indicated by the arrows.

In the colon tumor tissue the overall G6PD activity appeared to be stronger, especially cells that were located at luminal space showed enhanced G6PD activity (**Figure 18**; indicated by the black arrows). The cancerous cells appeared to show a more distinct G6PD activity than stromal cells. MAC-2 positive cells were found clustered in the tumor stroma (**Figure 18 A**). In those cells, G6PD activity appeared particularly high (**Figure 18 C**, indicated by the grey arrow). FAP positive cells were also found in the stromal part of the tumor, those cells had a noticeable lower G6PD activity than the surrounding cells (**Figure 18 D**, indicated by the grey arrow). Computerized analysis of G6PD activity confirmed the qualitative interpretation (**Figure 19**).

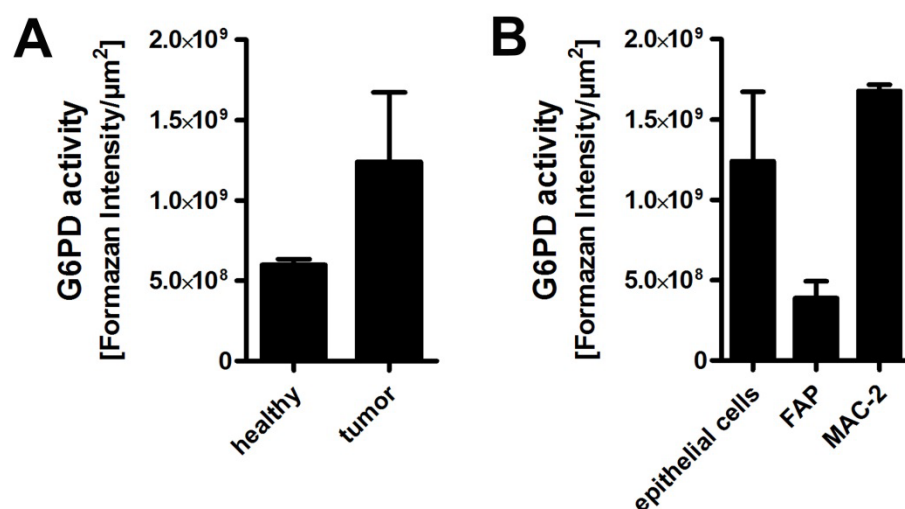


Figure 19. G6PD activity in cells of healthy and cancerous colon tissue. Computerized analysis revealed different enzymatic activities in epithelial cells (A) as well as in cells of the tumor microenvironment (B). Data represents mean of three replicates, error bars indicate standard deviation.

3.3.2. Activity of SDH

To investigate if the cells in healthy and cancerous colon tissue showed differences in SDH activity, enzymatic activities were analyzed in tissues retrieved from the same patient. In the healthy colon specimen, SDH activity was particularly located in the utmost epithelial cell layer, but evenly located within the whole cell (**Figure 20**, indicated by the grey arrow). Besides that, some cells that were located near the lamina propria showed moderate SDH activity (**Figure 20 A and B**). Those cells were randomly allocated throughout the periphery. Ki67 positive cells throughout the specimen showed high SDH activity, whereas there were almost no MAC-2-positive and no FAP positive cells visible (**Figure 20 A and B**).

In the cancerous colon tissue, cells exhibited diverse levels of SDH activities. Cells that were directly located at luminal space showed particularly high SDH activity (**Figure 20**, indicated by the black arrows). MAC-2 positive cells did not display any notable SDH activity (**Figure 20 A**). Some of the FAP positive cells which were located in the tumor stroma featured extremely high SDH activity (**Figure 20 B**, indicated by the grey arrow). Computerized analysis of SDH activity revealed that SDH activity was higher in epithelial cells of the healthy tissue compared to epithelial cells in the tumor (**Figure 20 C**). In the tumor microenvironment, epithelial cancer cells showed the highest SDH activity and FAP positive cells featured an approximately 60% reduced SDH activity. Compared to epithelial cells, SDH activity in MAC-2 positive cells was only 20% (**Figure 20 D**).

All in all, the determination of dehydrogenase activity with enzyme histochemistry was able to reveal differences in G6PD as well as in SDH activity among the different cells in non-cancerous as well as colon tumor tissue. These differences included an altered overall enzymatic activity, distinctions in activities in adjacent cells as well as varieties in intracellular localization.

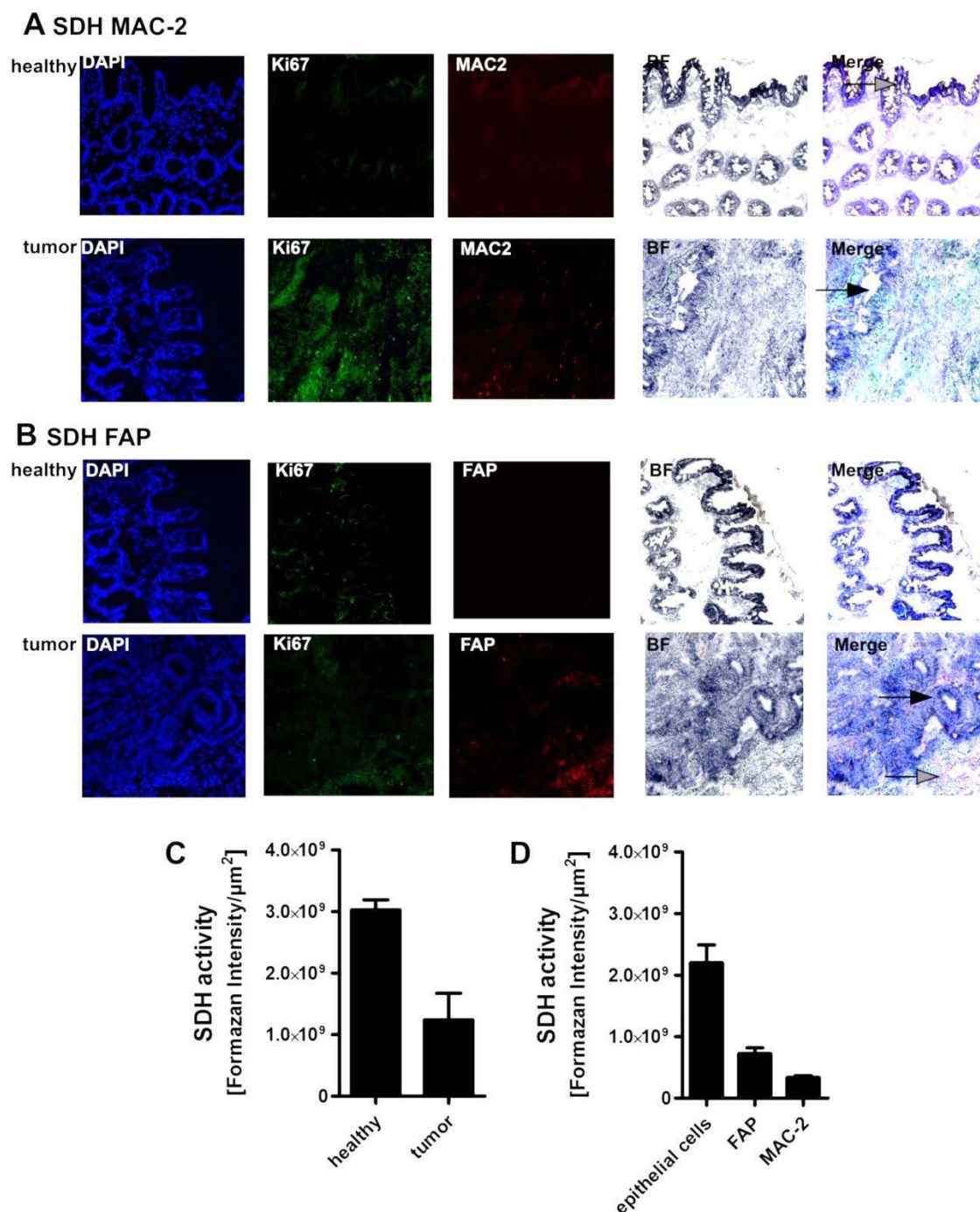


Figure 20. SDH activity in healthy and cancerous colon tissue. SDH activity (bright field, BF) was determined in combination with nuclear DAPI stain (blue), proliferation marker Ki67 (green), MAC-2 (red, A) or fibroblast activation protein FAP (red, B). Pictures were taken with a 20x objective. Metabolically distinct areas are indicated by the arrows. Computerized analysis revealed different enzymatic activities in epithelial cells of healthy and cancerous colon tissue (C) as well as in cells of the tumor microenvironment (D). Data represents mean of three replicates, error bars indicate standard deviation.

3.4. Metabolic landscapes of organotypic colon cancer co-culture can be used for functional *in-vitro* assays

In order to investigate metabolic co-dependencies between cells of the tumor microenvironment, I established a tool to integrate fibroblasts and macrophages into organotypic co-cultures with colon cancer cells. HTC-116 cancer cells were either grown on collagen gels including primary human CAFs alone, or on top of gels including CAFs and primary human macrophages. Additionally, we performed functional integration of LPS pre-stimulated macrophages with CAFs in the co-cultures. Activities of G6PD, GAPDH, LDH, IDH and SDH were measured in combination with detection of the proliferation marker Ki67 and DAPI. HTC-116 cells that were grown on top of CAFs showed an evenly distributed staining for LDH activity. The outermost cell layer of the cancer cells showed increased LDH activity (**Figure 21 A**, indicated by the arrow). Proliferating cells were evenly distributed throughout the cancerous cells.

HTC-116 cells that were grown on top of CAFs and naïve macrophages also presented an equal distribution of LDH activity (**Figure 21 B**). The utter cancer cell layer had increased LDH activity (**Figure 21 B**, indicated by the arrow). Proliferating cells were again evenly distributed throughout the cancer cells.

HTC-116 cells that were grown on top of CAFs and LPS pre-treated macrophages showed a different pattern in LDH activity (**Figure 21 C**). The utmost cancer cell layer showed stronger LDH activity compared to the cells that were located below (indicated by the boxes I and II). HTC-116 cells that were located on the bottom of the cell layer, in close proximity to the collagen gel also displayed stronger LDH activity (indicated by box III). Computerized analysis of LDH activities confirmed the qualitative interpretation (**Figure 21 D**).

Analysis of G6PD and GAPDH activity revealed an evenly distributed staining throughout the HTC-116 cells, whereas the utter top layer exhibited stronger enzymatic activities (**Figure 22 A and B**). Between the cancer cells grown on top of CAFs alone or in combination with naïve macrophages, no differences in glycolytic enzyme activities were detected compared to HTC-116 cells grown on top of LPS pre-treated macrophages. In contrast to that did tumor cells that were grown on top

of CAFs and LPS pre-treated macrophages show a gradient in mitochondrial IDH and SDH activity (**Figure 22 C and D**). Whereas the uttermost cancer cell layer showed the highest mitochondrial enzymatic activities (I), the cells located below showed weaker activities (II) and the cells that were in close proximity to the collagen gels exhibited even lower IDH and SDH activities (III).

All in all, upon different co-culture conditions the cellular top layer had a different metabolic setup compared to cells which were located below. Only cells than were grown on top of fibroblasts and LPS pre-stimulated macrophages showed differences in their metabolic configuration such as the formation of metabolic gradients. This data clearly indicated that this *in-vitro* co-culture model is a valid tool to recreate metabolic patterns as they are found in the *in-vivo* situation. The results support our concept that the presence of different cell types in the tumor microenvironment influences the metabolic configuration of the cancerous cells.

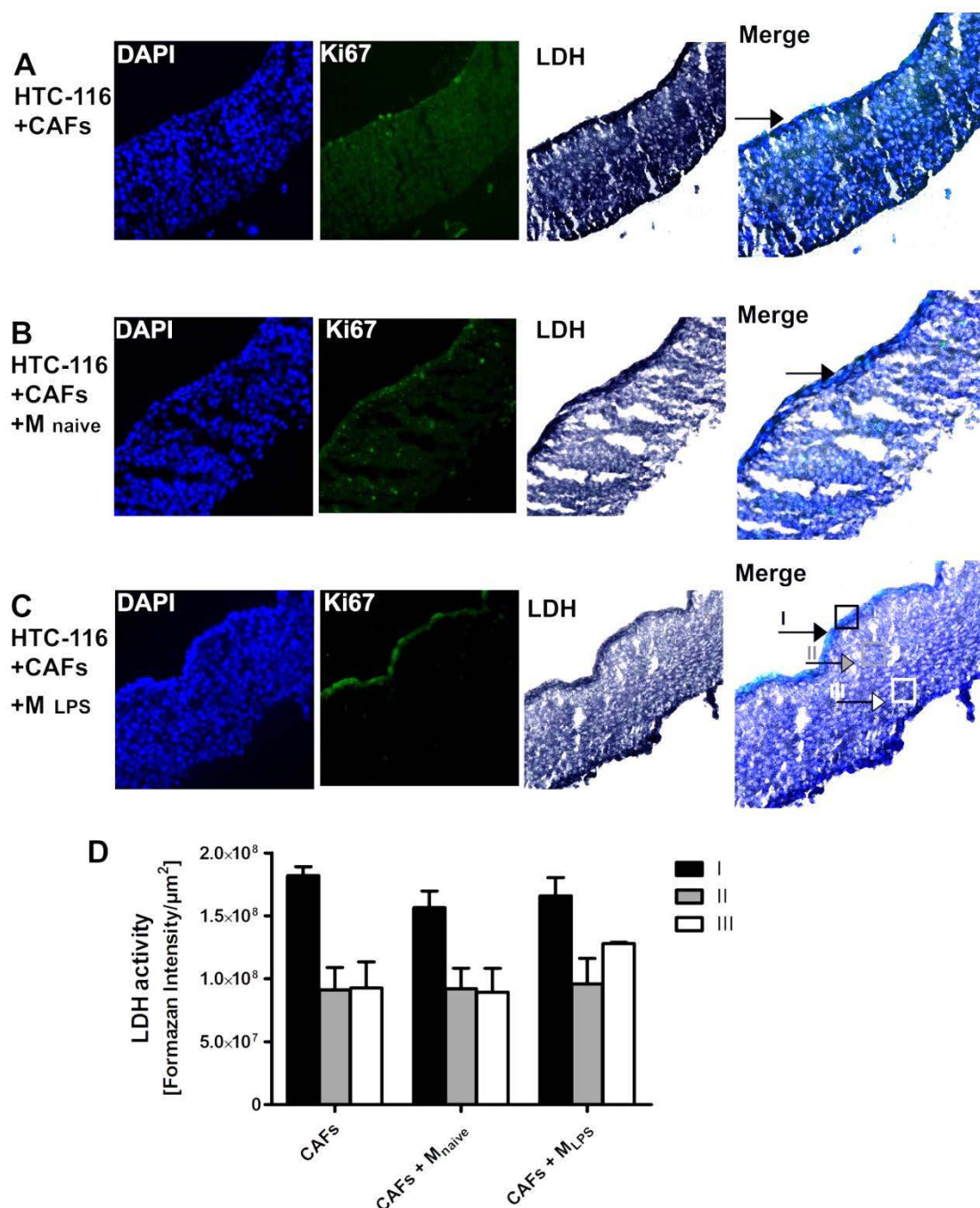


Figure 21. LDH activity in colon tumor cells cultured in organotypic co-cultures gels. HTC-116 cancer cells were grown on top of collagen gels including primary CAFs alone (A) or in combination with naïve macrophages (B) or LPS pre-treated primary macrophages (C). Prominent changes in enzymatic activities are indicated by the arrows. Pictures were taken with a 20x objective. Computerized analysis of LDH activity confirmed the quantitative interpretation of different enzymatic activities in individual parts of the cancer cell layer (D; I,II,III) Data represents mean of two replicates, error bars indicate standard derivation.

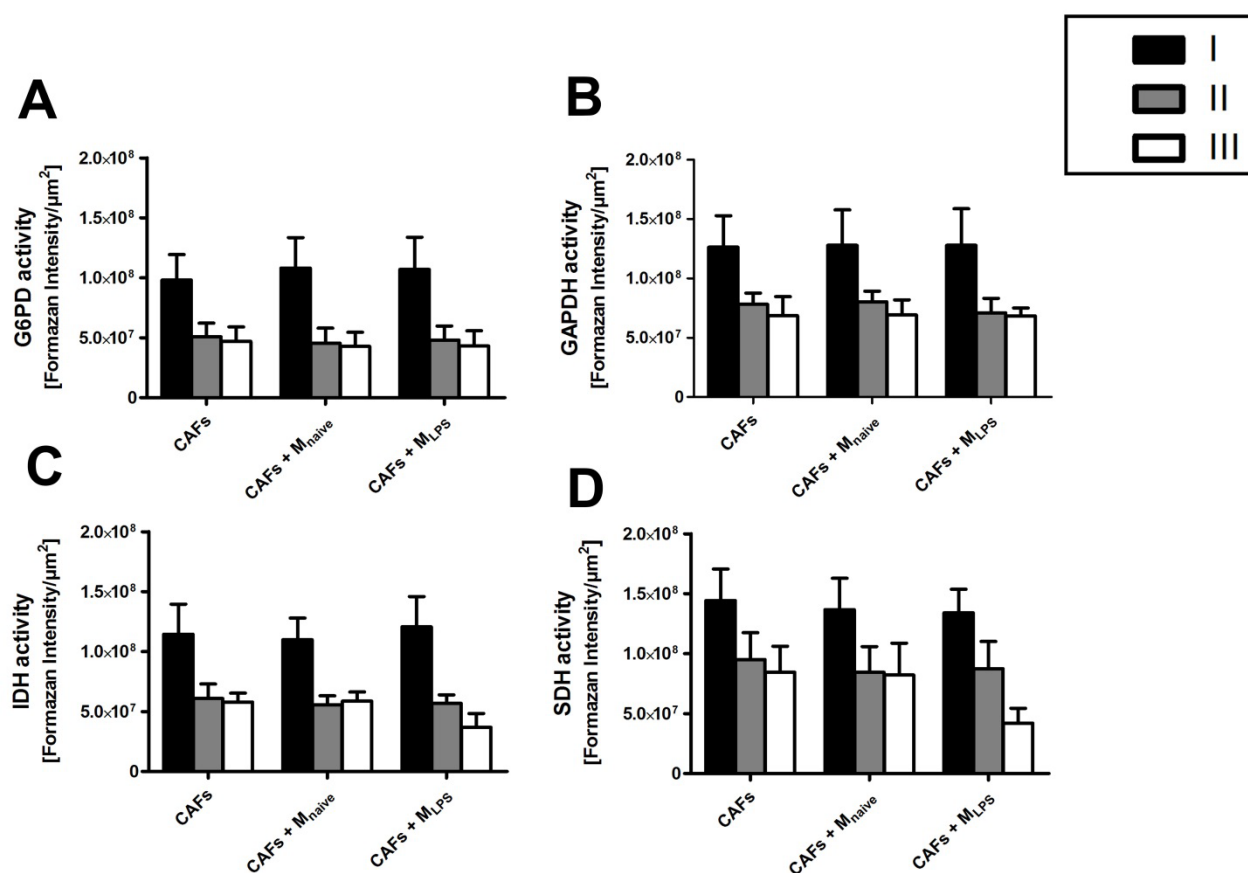


Figure 22. Enzymatic activities in colon tumor cells cultured in organotypic co-cultures gels. HTC-116 cancer cells were grown on top of collagen gels including primary CAFs alone or in combination with naïve macrophages or LPS pre-treated primary macrophages. Computerized analysis of G6PD (A), GAPDH (B), IDH (C) and SDH (D) activities revealed metabolic differences in individual parts of the cancer cell layer (I,II,III). Data represents mean of two replicates, error bars indicate standard derivation.

4. Discussion

4.1. Enzyme histochemistry: a valid tool to decipher metabolic landscapes?

4.1.1. Kinetic analysis of mouse liver and muscle metabolic enzymes reveals different biochemical properties between both tissues

Enzyme kinetics of G6PD, GAPDH, LDH, IDH and SDH were determined using a series of substrate dilutions and incubations times on mouse liver and muscle cryosections (**Figure 7-13**). Even though the experimental setup retrieved great source of error because every dilution and every time point had to be performed on a separate tissue slice, the overall outcome was more than satisfactory. In liver and muscle tissue, increasing substrate concentrations induced progressive coloration intensities for all detected enzymes (**figure 7-13**). Absence of substrate caused a very light pink staining which can be seen as the „overall redox background“ of the tissue. This unspecific “background” retrieves information about residual dehydrogenase and oxidase activities as well as other reducing agents in the tissue slices. The “background reaction” represents a valuable control reaction and may even contain information about the overall redox status of the particular tissue.

The color formation in all enzymatic assays could be suppressed by addition of inhibitors, demonstrating the specificity of the presented activity detections (**Figure 8-13**). As the concentrations of all necessary coenzymes and cofactors were kept at constant, saturating conditions, I applied the Michaelis-Menten model for single substrate reactions to calculate the biochemical enzyme properties. Additional data evaluation using Hanes-Woolf plot showed comparable results. Both data evaluation systems indicated great variance in K_M and V_{max} between the two tissues (**Figure 9-13**). In liver, G6PD had a higher turnover rate and weaker substrate binding capability compared to muscle G6PD as previously described in the literature (Battistuzzi et al., 1985). GAPDH showed a lower rate of turnover and also lower substrate binding abilities compared to muscle GAPDH (**figure 10**). Studies on GAPDH gene expression reveal a higher GAPDH expression in muscle whereas no data for enzymatic activities were available (Barber et al., 2005; Piechaczyk et

al., 1984). LDH turnover rates were at a comparable level between both tissues, whereas liver LDH had a much lower substrate binding capacity as muscle LDH. The literature describes human as well as mouse LDH as more active in the liver (Singh and Kanungo, 1968; Van Noorden, 1989). The mitochondrial IDH isoform and SDH had both lower turnover rates and better binding capacity in liver compared to muscle. In rodents, the literature usually describes IDH as well as SDH activity to be higher in liver than in muscle tissue (Bennett, 1972; Czyzewska et al., 2012). Unspecificity of the detected signal could be excluded, because formazan formation was severely suppressed by addition of the substrate analogues oxaloglycine and malonate (**Figures 12 and 13 E**). One possible explanation could rest upon the tight regulation of metabolic flow through the citric acid cycle. Both enzymes can be strongly inhibited by competitive feedback inhibition of other TCA intermediates. The reaction catalyzed by IDH is irreversible due to its large negative free energy change and inhibited by NAD and alpha-ketoglutarate as well as by ATP (Gabriel et al., 1985; Gabriel et al., 1986; Rutter and Denton, 1988). SDH is vigorously inhibited by malate and oxaloacetate (Dutra et al., 1993; Greene et al., 1993; Zeylemaker et al., 1969). In this experimental setup, application of excessive amounts of substrate might have triggered enzyme inhibition and lead to distorted data in the calculated kinetics.

An uniform incubation time of 15 minutes was appointed for all enzymatic assays, because some reactions including enzyme specific inhibitors started to give rise to an unspecific staining after 20 minutes of incubation (**Figure 10 E and 12 E**). Selection of substrate concentration was based on the Michaelis-Menten kinetics to retrieve a zero-order enzymatic activity upon saturating substrate concentrations. Furthermore, the incubation temperature was taken into consideration, choosing incubation at room temperature because of a „patchy“ staining at 37°C due to tissue desiccation.

4.1.2. Integration of pyruvate metabolism in metabolic landscapes is desirable but not methodologically sound

Pyruvate is the key intermediate in the intersection of glycolysis, lactate production, citric acid cycle, amino acid generation and hepatic gluconeogenesis. Because of its unique position in the metabolic network we found its catalysis and channeling into the TCA of special interest. Therefore, I established time dependent dose response curves for the pyruvate kinase (PK) and pyruvate dehydrogenase complex (PDH). Upon increasing substrate concentrations an enhanced formazan formation was detected and the coloration was severely suppressed by addition of enzyme specific inhibitors (**Figure S 2 A and S 4 A**). As both detection methods are in need of various co-substrates, formazan formation upon coenzyme omission was also detected. In the assay for determination of PDH activity, exclusion of FAD led to an even lower formazan formation as in the inhibited reaction (**Figure S 2 B**). FAD is a cellular redox factor and can be reduced to FADH₂. A variety of enzymes, including some dehydrogenases and oxygenases use FAD as a redox cofactor, leading to contemporary reduction of NBT to formazan and produce an unspecific coloration of the tissue specimen. The coupled assay detecting PK activity involved addition of various cofactors as well as supplemental auxiliary enzymes. Control reactions, that contained a PK inhibitor and lacked either HK or G6PD revealed that omission of G6PD reduced the formazan signal about 66%. Addition of an inhibitor reduced formazan production about 73%. Strikingly, exclusion of HK did only slightly reduce the formazan production. Addition of HK as an auxiliary enzyme therefore did not have the same impact on PK activity detection as G6PD. HKs phosphorylate hexoses and glucose is the most prominent substrate. The omission of HK may not have impact on the determined PK activity because hexoses are very active enzymes and may show a high residual activity in the cryosections. Nevertheless, it was decided that reactions that are not fully „controlled“ should not be included in the routine assay because such a theory has to be confirmed before - for example through specific inhibition of HK with mannoheptulose.

4.1.3. Substitution of NBT by fluorescent CTC is not recommendable for deciphering metabolic landscapes

The redox dye CTC produces a fluorescent signal after reduction and has already been applied in flow-cytometric determination of dehydrogenase activities in the same manner as NBT (Frederiks et al., 2006). CTC shows the same pattern of staining as NBT in human colon tissue sections (**Figure 15 A and B**). Subsequent incubation with DAPI and MAC-2 was also functional. Nevertheless, CTC as substitute for NBT had one major disadvantage: The fluorescent formazan was only stable for about two hours (**Figure 15 C**). Considering, that NBT was stable for month, CTC clearly had its advantages in other applications such as subcellular tracing of enzymatic activities in combination with confocal laser scanning microscopy. For the purpose of deciphering the metabolic landscapes of complex tissues, I recommended the utilization of NBT.

4.2. Metabolic landscapes of complex tumor tissues

The aim of this work was to establish a method to create metabolic maps of enzyme activities in complex tissues. The histochemical detection of enzyme activities was combined with conventional immunohistochemical approaches to identify certain cell types or functional markers. Possible applications involve all situations in which different cell types are located in tissue areas which are predestined to have different metabolic functions. As the previously described enzymes G6PD, GAPDH, LDH, IDH and SDH are all known to be essential in the primary carbohydrate catabolism, the localization of their activity was estimated in different cancer tissues. The established technique was applied to samples of human lung adenocarcinoma, pleural mesothelioma and colon cancer (**Figure 17**). We were able to reveal differences in metabolic setups between the different tumor samples as well as differences between cells of the tumor microenvironment. At least our test samples, which were not representative to allow any valid conclusion, revealed that the slow growing and treatment resistant pleural mesothelioma demonstrated very low enzymatic activities. In contrast to that, lung adenocarcinoma showed extremely high activity of G6PD and moderate activities of the other estimated

enzymatic activities. Colon carcinoma showed the most diverse distribution of enzymatic activities. The overall activity of G6PD and SDH was elevated and differed between certain cells. The combined detection of five metabolic enzymes was suitable to reveal distinct metabolic patterns between different cancer types as well as between the individual cells of the tumor microenvironment.

4.2.1. Cell type identification in the metabolic landscapes of healthy and cancerous colon tissue reveals differences in cellular metabolic configurations

According to the previous results, G6PD and SDH activities were successfully assigned to different cell types and functional marker expression in human colon cancerous and non-cancerous tissue. Fluorescent labeled antibodies for macrophages (MAC-2), activated fibroblasts (FAP) as well as the proliferation marker Ki67 were applied in combination with a nuclear DAPI stain (**Figure 18 - 20**). For analysis, the TissueFAX system was used because it is an automated workstation for both fluorescence and bright field scanning of whole tissue sections equivalent to flow cytometry. One the greatest advantage of the detection system is that it is possible to record bright field and fluorescent pictures at the same time, but one drawback is that it is not possible display the pictures together. Therefore, an alternative method to merge the acquired pictures was established (see **Figure 5**). Merged images of enzymatic activities in healthy colon tissue revealed that G6PD activity was especially located in the apical side of external epithelial cells in the crypts, but not in the goblet cells and the lamina propia (**Figure 18 and 19**). Ki67 positive cells were scattered among the crypts, they did not show a different G6PD activity than the surrounding epithelial cells. In colon tumor tissue the overall G6PD activity appeared stronger (**Figure 18 and 19**). Compared to stromal cells, cancerous cells revealed an enhanced G6PD activity. MAC-2 positive cells were found throughout the whole tissue and showed increased G6PD activity (**Figure 19**). FAP positive cells were located in the stromal part of the tumor, those cells had a lower G6PD activity. A metabolic “lining” of G6PD seemed to be associated with the border between proliferating cancerous cells and stromal cells. In yeast, elevated G6PD levels are associated with cellular proliferation, but enhanced

enzymatic activity may also be an advantage in cancer cell growth as a recent study revealed an anti-cancerogenic effect of the G6PD inhibitor DHEA on precursors of colon cancer (Osawa et al., 2002; Ralser et al., 2007).

SDH activity in healthy colon tissue was evenly located in the utmost epithelial cell layer and also in single cells that were located in the lamina propria (**Figure 20**). In the cancerous tissue, cells demonstrated diverse levels of SDH activities. MAC-2 positive cells did not exhibit detectable expression of SDH and some of the FAP positive cells presented moderate activity of SDH (**Figure 20 C**). These assays clearly revealed that the different cells which were part of the healthy colon tissue, but especially the cells in the tumor tissue microenvironment had unique metabolic configurations. These results indicated that the established method could become a valuable tool for metabolic fingerprinting in the field of personalized medicine. Personalized medicine is a healthcare model which recommends customized treatment decisions depending on molecular analysis. Diagnostic testing is employed in advance or in course of a therapy to select appropriate medical procedures. Subsequently to a biopsy, metabolic fingerprinting could be applied in addition to common routine histology when choosing growth suppressing anti-cancer treatments based on metabolic intervention. Prior estimation of cellular metabolic configurations could significantly benefit therapeutic outcomes. Additionally, these pictures revealed information that traditional histological staining procedures do not detect. Enzymatic activity was not only diverse in different cell types such as macrophages or fibroblasts, but show two surprising new attributions: assembly of multicellular complexes with similar metabolic alignments as well as differences in subcellular localization. Such intracellular “clustering” of sequential enzymes of metabolic pathways has been repeatedly reported in recent years (Beeckmans et al., 1990). Multienzyme complexes could accumulate under conditions of excessive energy necessity such as cellular proliferation or locomotion. The high resolution capacity indicates, that the method is sensitive to even small metabolic imbalances and could not only be used as a personalized pre-treatment opportunity, but as an accompanying routine procedure for early revelation of treatment resistances due to metabolic shifts. As promising as this preliminary data appears, it is not sufficient to make biological assertion. To reveal functional cellular assignments in the context of cancerogenesis, a higher number

of patients should be analyzed. On top, the data should be interpreted in context of patient gender, body weight, age, medical history and genetic attributes.

4.2.2. Metabolic structure replication of organotypic colon cancer co-cultures is a valuable tool and reveals a possible role for macrophage activation status on cancer cell metabolism

In order to have a functional *in-vitro* model to investigate metabolic co-dependencies between cells of the tumor microenvironment, I established a colon carcinoma co-culture system. HTC-166 colon cancer cells were either grown on collagen gels including CAFs alone or on top of gels including CAFs and primary human macrophages. Additionally, LPS-pretreated macrophages were integrated in the assay to ascertain a potential rewiring of enzymatic activities by macrophage polarization. Activities of G6PD, GAPDH, LDH, IDH and SDH were measured in combination with detection of the proliferation marker Ki67 and DAPI. Independent of co-cultured cell types, G6PD and GAPDH activity was evenly distributed throughout the HTC-116 cells, whereas the cellular top layer exhibited stronger enzymatic activities (**Figure 22**). The cellular top layer appeared to have a different metabolic overall condition than the cells inside the cell mass and was most probably not affected by the fibroblasts and macrophages inside the gel. Nevertheless, it was striking, that the top layer resembled the epithelial cancer cells which were located directly bordering a luminal space (**see Figure 17-19**). In the co-culture system as well as *in-vivo* these cells were rich in oxygen supply and showed a higher metabolic capacity than adjoining cells which displayed weaker enzymatic activities.

Only tumor cells grown on top of fibroblasts and LPS pre-stimulated macrophages showed differences in their metabolic configuration. The cancer cell layer showed the formation of a metabolic gradient. Under hypoxic conditions in the lower parts of the cancer cell layer LDH activity was increased and mitochondrial IDH and SDH activities were decreased (**figure 21 and 22**). Those cells predominantly produced energy by a high rate of glycolysis followed by lactic acid fermentation in the cytosol rather than pyruvate oxidation in the mitochondria.

Above all, this data indicates that the organotypic 3D co-culture model at least partly reassembles the metabolic *in-vivo* situation found in the tumor microenvironment of human colon cancer tissue. It was a valid tool to recreate metabolic patterns as they were found in the *in-vivo* situation. Additionally, the *in-vitro* system revealed a possible functional role for LPS-pretreated macrophages in rewiring cancer cell metabolism. The results support our concept that the presence of different cell types in the tumor microenvironment influences the metabolic configuration of the cancerous cells. As a further perspective the model could also be applied for functional testing of metabolic inhibitors and their influence on cancer metabolism.

4.3. Conclusion

In contrast to traditional histology, enzyme histochemistry is a method for imaging enzymatic reactions that links biochemistry and morphology (Hardonk and Koudstaal, 1976). As demonstrated in the first part of this work, the activity assays followed stoichiometric principles and could therefore be used to estimate enzyme activities in complex tissue. In addition, the combination with immunohistochemical staining techniques allowed precise assignment of enzyme activities to certain cell types and localization within the individual cells. Together, this gave valuable information about cellular as well as area specific metabolic configurations within complex tissue while representing the histological structure of the enzymatic activities. This is a powerful, dynamic and technically easy technique, which is able to reveal even small metabolic imbalances due to its high resolution. Please note, that this method does only allow direct quantitative comparison of one specific enzyme between different samples. Nevertheless, other comparable techniques such as metabolomics or the real time extracellular flux analyzer (Seahorse Bioscience) are either much more elaborate and expensive, lack resolution or specificity. The methods and procedures, which were established within this thesis might become valuable tools to predict patient-specific treatment outcome as well as resistance and are of interest to all research areas which address metabolic co-dependencies of different cell types.

5. Supplements

Attempting to integrate pyruvate metabolism in metabolic landscaping

Pyruvate, the carboxylate anion of pyruvic acid is a key intermediate in the intersection of several metabolic pathways. Primarily, it originates from glucose as the final product of glycolysis and can fuel energy production by conversion into acetyl-CoA which channels the citric acid cycle and fatty acid production. Pyruvate can also be converted to oxaloacetate which refills intermediates of the TCA, but also serves the conversion to carbohydrates via gluconeogenesis. Beyond that, pyruvate can be used in the generation of amino acids such as alanine, glycine, threonine, cysteine and serine. As mentioned before, upon hypoxic conditions, pyruvate can be anaerobically catalyzed to lactate. Because pyruvate occupies a unique position in connecting metabolic pathways its fate is of special interest in the generation of metabolic network maps.

Detection of PDH activity is not necessarily specific

One of the main fates of pyruvate is the PDH mediated conversion to acetylCoA to fuel mitochondrial metabolism. PDH is a complex of three enzymes that converts pyruvate into acetyl-CoA (see **Figure S 1**). The initial step is performed by the actual pyruvate dehydrogenase, which binds thiamine pyrophosphate to pyruvate followed by decarboxylation. The resulting molecule attacks lipoid acid that is attached to a lysine residue. Subsequently, S₂ is displaced as a sulfide or sulfhydryl moiety. Subsequent collapse of the tetrahedral hemithioacetal ejects thiazole, releasing the TPP cofactor and producing a thioacetate of lipoate. In the next step, the lipoate-thioester is translocated into the next active side of the enzymatic complex, called dihydrolipoyl transacetylase, where the acetyl the lipoyl is transferred to Coenzyme A. This produces acetylCoA, which is released from the enzyme complex and subsequently enters the citric acid cycle. The dihydrolipoate which is still bound to the lysin residue then enters the complex's next active site, the dihydrolipoyl dehydrogenase. There, FAD oxidizes dihydrolipoate back to its

lipoate resting state, producing FADH_2 . Then, NAD^+ oxidizes FADH_2 back to its FAD resting state, producing NADH/H^+ . This in return can serve as a reducing factor to form formazan from NBT and visualize the activity of the pyruvate dehydrogenase complex when all necessary cofactors are abundantly provided.

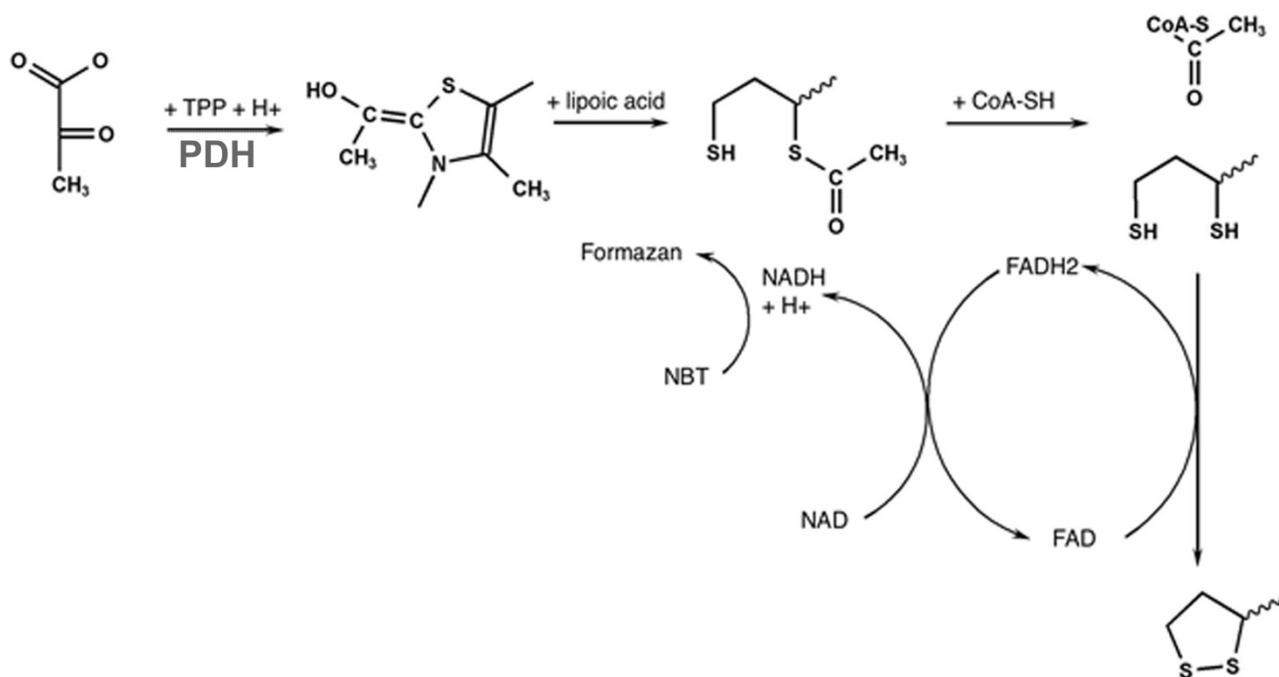


Figure S 1. Chemical reaction series catalyzed by PDH and the associated detection via reduction of NBT. Formazan formation is directly linked to FADH_2 -dependent production of NADH/H^+ .

When supplying the NBT-based reaction on mouse liver with different concentrations of pyruvate (and all necessary cofactors including TPP, CoA, NAD and FAD) a dose-dependent increase in coloration was visible. Analysis with the HistoQuest software also implied a steady accumulation of signal after 15 minutes of incubation (**Figure S 2 A**). Control reactions, that were supplied with 300 mM of the substrate analogue 3-fluoro-2-oxopropanoic acid an enzyme specific inhibitor, or that lacked one of the coenzymes all showed decreased formazan formation

(**Figure S 2 B**). Notably, formazan intensity was particularly low when FAD was excluded from the reaction mixture (**Figure S 2 B**).

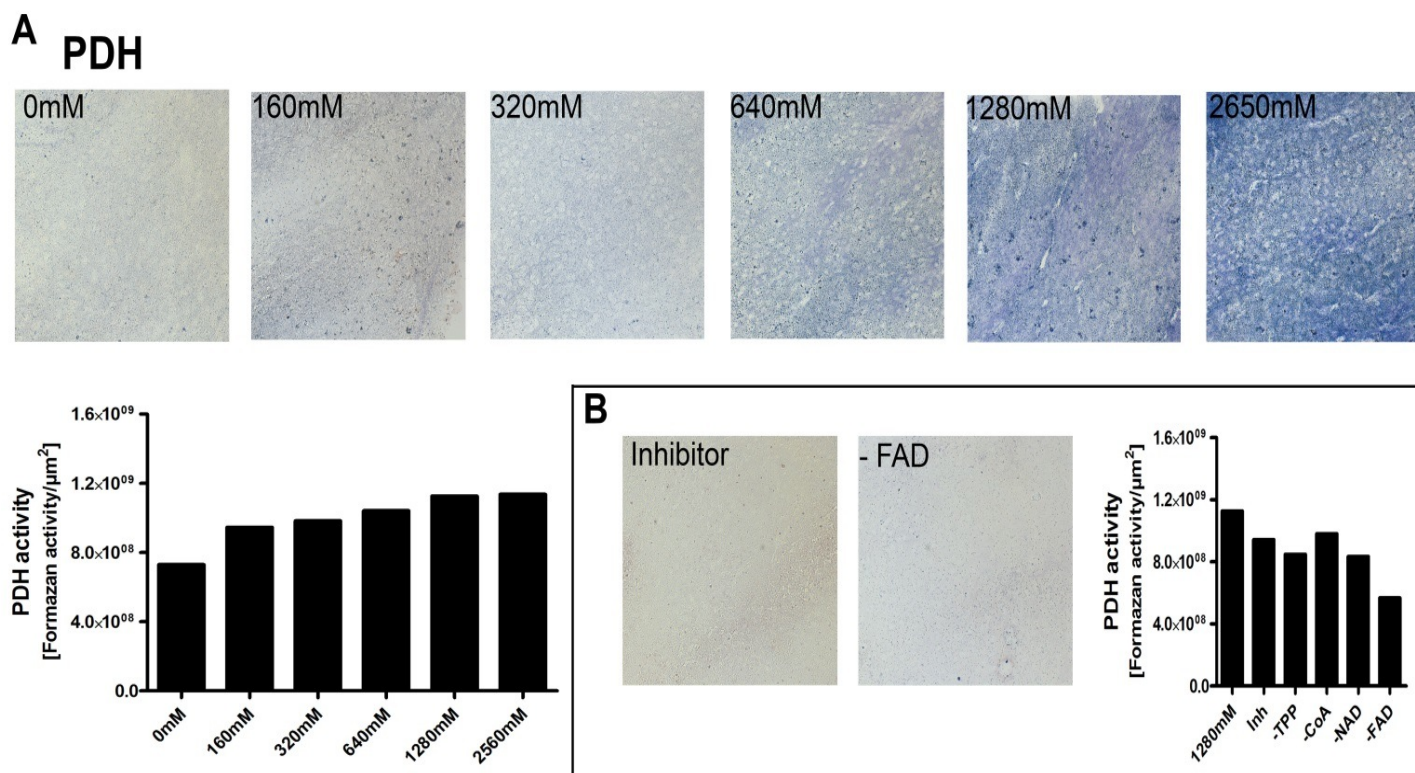


Figure S 2. Detection of PDH activity in mouse liver cryosections. Upon addition of different concentrations of sodium pyruvate (0 mM, 160 mM, 320 mM, 640 mM, 1280 mM and 2650 mM) PDH activity was determined by means of total formazan formation/μm² (A). Specificity of the depicted reaction was determined either by exclusion of co-substrates or addition of 300 mM of the substrate analogue 3-fluoro-2-oxopropanoic acid (B). Data is representative for one experiment.

Detection of PK activity is not necessarily specific

Theoretically, the NBT-based detection of enzymatic activity can be used to determine the activities of all dehydrogenases when the reaction is supplied with necessary substrates and cofactors. Above that, there is also the possibility to detect activities of enzymes other than dehydrogenases in form of a coupled assay. Potentially, this opens the possibility to map metabolic networks beyond dehydrogenase activities. PK which catalyzes the final step of glycolysis was chosen to serve as an example. PK transfers a phosphate group from phosphoenolpyruvate (PEP) to ADP - yielding one molecule of pyruvate and ATP (see **Figure S 3**). Coupling one enzymatic reaction with another enabled determination of PK activity with NBT. The product of the first reaction was substrate for the second reaction (see **Figure S 3**). The generated ATP could be further processed by HK. In a secondary coupled reaction, G6P could be processed to 6-phospho-D-glucono-1,5-lactone by G6PD, which is the actual detected reaction. Not only substrates and co-substrates were provided in excess, also the necessary auxiliary enzymes had to be abundant. Addition of different PEP concentrations led to dose dependent coloration of the liver specimen compared to a reaction lacking PEP as a substrate. Control reactions that contained 1200 mM glutathione and lacked either HK or G6PD revealed that omission of G6PD reduced the formazan signal about 66% (**Figure S 4 B**). Addition of GSH inhibited PK activity approximately 73%. Strikingly, exclusion of HK did only slightly diminish formazan production compared to the full reaction. Addition of HK as an auxiliary enzyme therefore did not have the same impact on PK activity detection as G6PD.

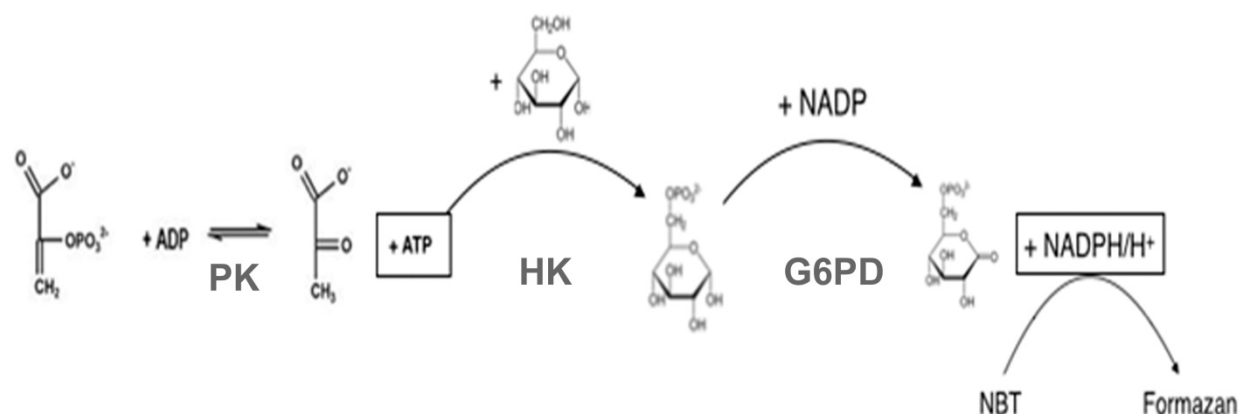
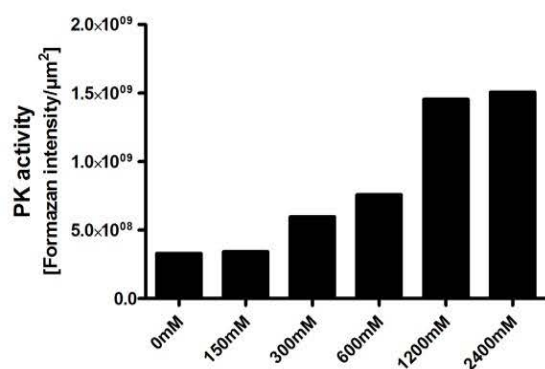
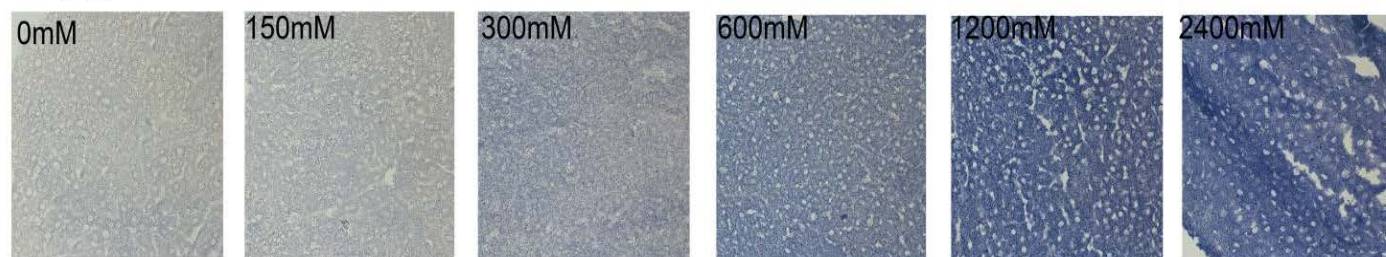


Figure S 3. Coupled series of reactions for PK activity detection. ATP, the byproduct of the transfer of one phosphate from PEP serves as a co-substrate for the HK-mediated phosphorylation of glucose to G6P. Subsequently, the G6P serves in a secondary-coupled reaction as a substrate for 6-phospho-D-glucono-1,5-lactone production by G6PD. When all substrates, cofactors and enzymes are added in excess, the last reaction, forming NADPH/H⁺ leads to reduction of the redox dye NBT - forming a colored formazan product at the exact location of the first enzyme in the reaction series.

A PK



B

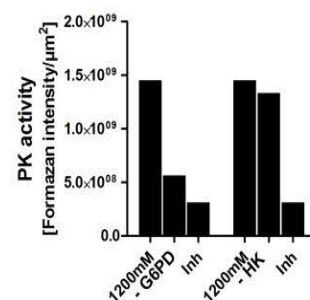
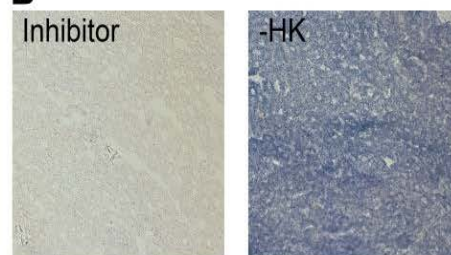


Figure S 4. Detection of PK activity in mouse liver. Dose dependent PK activity was determined upon addition of different concentrations of PEP (0 mM, 150 mM, 300 mM, 600 mM, 1200 mM and 2400 mM; A). Verification of the specificity was performed by omission of auxiliary enzymes G6PD and HK and upon addition of 1200 mM glutathione as an inhibitor (B). Data is representative for one experiment.

6. References

Ich habe mich bemüht, sämtliche Inhaber der Bildrechte ausfindig zu machen und ihre Zustimmung zur Verwendung der Bilder in dieser Arbeit eingeholt. Sollte dennoch eine Urheberrechtsverletzung bekannt werden, ersuche ich um Meldung bei mir.

- Addabbo, F., Montagnani, M., and Goligorsky, M.S. (2009). Mitochondria and reactive oxygen species. *Hypertension* 53, 885-892.
- Agarwal, A.R., Zhao, L., Sancheti, H., Sundar, I.K., Rahman, I., and Cadenas, E. (2012). Short-term cigarette smoke exposure induces reversible changes in energy metabolism and cellular redox status independent of inflammatory responses in mouse lungs. *American journal of physiology Lung cellular and molecular physiology* 303, L889-898.
- Altman, F.P. (1974). Studies on the reduction of tetrazolium salts. 3. The products of chemical and enzymic reduction. *Histochemie Histochemistry Histochimie* 38, 155-171.
- Anastasiou, D., Poulogiannis, G., Asara, J.M., Boxer, M.B., Jiang, J.K., Shen, M., Bellinger, G., Sasaki, A.T., Locasale, J.W., Auld, D.S., *et al.* (2011). Inhibition of pyruvate kinase M2 by reactive oxygen species contributes to cellular antioxidant responses. *Science* 334, 1278-1283.
- Anderberg, C., and Pietras, K. (2009). On the origin of cancer-associated fibroblasts. *Cell Cycle* 8, 1461-1462.
- Babior, B.M. (1999). NADPH oxidase: an update. *Blood* 93, 1464-1476.
- Bailey, K.M., Wojtkowiak, J.W., Hashim, A.I., and Gillies, R.J. (2012). Targeting the metabolic microenvironment of tumors. *Adv Pharmacol* 65, 63-107.
- Barber, R.D., Harmer, D.W., Coleman, R.A., and Clark, B.J. (2005). GAPDH as a housekeeping gene: analysis of GAPDH mRNA expression in a panel of 72 human tissues. *Physiological genomics* 21, 389-395.
- Battistuzzi, G., D'Urso, M., Toniolo, D., Persico, G.M., and Luzzatto, L. (1985). Tissue-specific levels of human glucose-6-phosphate dehydrogenase correlate with methylation of specific sites at the 3' end of the gene. *Proceedings of the National Academy of Sciences of the United States of America* 82, 1465-1469.
- Beeckmans, S., Van Driessche, E., and Kanarek, L. (1990). Clustering of sequential enzymes in the glycolytic pathway and the citric acid cycle. *Journal of cellular biochemistry* 43, 297-306.

- Bennett, A.F. (1972). Comparison of Activities of Metabolic Enzymes in Lizards and Rats. *Comp Biochem Physiol* 42, 637-8.
- Biswas, S., Lunec, J., and Bartlett, K. (2012a). Non-glucose metabolism in cancer cells--is it all in the fat? *Cancer metastasis reviews* 31, 689-698.
- Biswas, S.K., Chittezhath, M., Shalova, I.N., and Lim, J.Y. (2012b). Macrophage polarization and plasticity in health and disease. *Immunologic research* 53, 11-24.
- Biswas, S.K., and Mantovani, A. (2010). Macrophage plasticity and interaction with lymphocyte subsets: cancer as a paradigm. *Nature immunology* 11, 889-896.
- Callura, J.M., Cantor, C.R., and Collins, J.J. (2012). Genetic switchboard for synthetic biology applications. *Proceedings of the National Academy of Sciences of the United States of America* 109, 5850-5855.
- Cantor, J.R., and Sabatini, D.M. (2012). Cancer cell metabolism: one hallmark, many faces. *Cancer discovery* 2, 881-898.
- Chiarugi, P., Paoli, P., and Cirri, P. (2014). Tumor microenvironment and metabolism in prostate cancer. *Seminars in oncology* 41, 267-280.
- Clasquin, M.F., Melamud, E., Singer, A., Gooding, J.R., Xu, X., Dong, A., Cui, H., Campagna, S.R., Savchenko, A., Yakunin, A.F., *et al.* (2011). Riboneogenesis in yeast. *Cell* 145, 969-980.
- Czyzewska, U., Tylicki, A., Siemieniuk, M., and Strumilo, S. (2012). Changes of activity and kinetics of certain liver and heart enzymes of hypothyroid and T(3)-treated rats. *Journal of physiology and biochemistry* 68, 345-351.
- Dawson, I.M., and Filipe, M.I. (1967). The value of enzyme histochemical studies in the histological and cytological diagnosis of uterine cervical lesions. *The Journal of obstetrics and gynaecology of the British Commonwealth* 74, 432-441.
- DeBerardinis, R.J., Lum, J.J., Hatzivassiliou, G., and Thompson, C.B. (2008). The biology of cancer: metabolic reprogramming fuels cell growth and proliferation. *Cell metabolism* 7, 11-20.
- Dolznic, H., Rupp, C., Puri, C., Haslinger, C., Schweifer, N., Wieser, E., Kerjaschki, D., and Garin-Chesa, P. (2011). Modeling colon adenocarcinomas in vitro a 3D co-culture system induces cancer-relevant pathways upon tumor cell and stromal fibroblast interaction. *The American journal of pathology* 179, 487-501.

- Du, W., Jiang, P., Mancuso, A., Stonestrom, A., Brewer, M.D., Minn, A.J., Mak, T.W., Wu, M., and Yang, X. (2013). TAp73 enhances the pentose phosphate pathway and supports cell proliferation. *Nature cell biology* 15, 991-1000.
- Dutra, J.C., Dutra-Filho, C.S., Cardozo, S.E., Wannmacher, C.M., Sarkis, J.J., and Wajner, M. (1993). Inhibition of succinate dehydrogenase and beta-hydroxybutyrate dehydrogenase activities by methylmalonate in brain and liver of developing rats. *Journal of inherited metabolic disease* 16, 147-153.
- Fischer, K., Hoffmann, P., Voelkl, S., Meidenbauer, N., Ammer, J., Edinger, M., Gottfried, E., Schwarz, S., Rothe, G., Hoves, S., *et al.* (2007). Inhibitory effect of tumor cell-derived lactic acid on human T cells. *Blood* 109, 3812-3819.
- Folkman, J. (1971). Tumor angiogenesis: therapeutic implications. *The New England journal of medicine* 285, 1182-1186.
- Frederiks, W.M., van Marle, J., van Oven, C., Comin-Anduix, B., and Cascante, M. (2006). Improved localization of glucose-6-phosphate dehydrogenase activity in cells with 5-cyano-2,3-ditolyl-tetrazolium chloride as fluorescent redox dye reveals its cell cycle-dependent regulation. *The journal of histochemistry and cytochemistry : official journal of the Histochemistry Society* 54, 47-52.
- Frederiks, W.M., Vizan, P., Bosch, K.S., Vreeling-Sindelarova, H., Boren, J., and Cascante, M. (2008). Elevated activity of the oxidative and non-oxidative pentose phosphate pathway in (pre)neoplastic lesions in rat liver. *International journal of experimental pathology* 89, 232-240.
- Gabriel, J.L., Milner, R., and Plaut, G.W. (1985). Inhibition and activation of bovine heart NAD-specific isocitrate dehydrogenase by ATP. *Archives of biochemistry and biophysics* 240, 128-134.
- Gabriel, J.L., Zervos, P.R., and Plaut, G.W. (1986). Activity of purified NAD-specific isocitrate dehydrogenase at modulator and substrate concentrations approximating conditions in mitochondria. *Metabolism: clinical and experimental* 35, 661-667.
- Gajewski, T.F., Schreiber, H., and Fu, Y.X. (2013). Innate and adaptive immune cells in the tumor microenvironment. *Nature immunology* 14, 1014-1022.
- Gerlinger, M., Rowan, A.J., Horswell, S., Larkin, J., Endesfelder, D., Gronroos, E., Martinez, P., Matthews, N., Stewart, A., Tarpey, P., *et al.* (2012). Intratumor heterogeneity and branched evolution revealed by multiregion sequencing. *The New England journal of medicine* 366, 883-892.

- Gillies, R.J., Schornack, P.A., Secomb, T.W., and Raghunand, N. (1999). Causes and effects of heterogeneous perfusion in tumors. *Neoplasia* 1, 197-207.
- Greene, J.G., Porter, R.H., Eller, R.V., and Greenamyre, J.T. (1993). Inhibition of succinate dehydrogenase by malonic acid produces an "excitotoxic" lesion in rat striatum. *Journal of neurochemistry* 61, 1151-1154.
- Hanahan, D., and Coussens, L.M. (2012). Accessories to the crime: functions of cells recruited to the tumor microenvironment. *Cancer cell* 21, 309-322.
- Hanahan, D., and Weinberg, R.A. (2000). The hallmarks of cancer. *Cell* 100, 57-70.
- Hanahan, D., and Weinberg, R.A. (2011). Hallmarks of cancer: the next generation. *Cell* 144, 646-674.
- Hardonk, M.J., and Koudstaal, J. (1976). Enzyme histochemistry as a link between biochemistry and morphology. *Progress in histochemistry and cytochemistry* 8, 1-68.
- Haschemi, A., Kosma, P., Gille, L., Evans, C.R., Burant, C.F., Starkl, P., Knapp, B., Haas, R., Schmid, J.A., Jandl, C., *et al.* (2012). The sedoheptulose kinase CARKL directs macrophage polarization through control of glucose metabolism. *Cell metabolism* 15, 813-826.
- Hu, T., Zhang, C., Tang, Q., Su, Y., Li, B., Chen, L., Zhang, Z., Cai, T., and Zhu, Y. (2013). Variant G6PD levels promote tumor cell proliferation or apoptosis via the STAT3/5 pathway in the human melanoma xenograft mouse model. *BMC cancer* 13, 251.
- Inai, K. (2008). Pathology of mesothelioma. *Environmental health and preventive medicine* 13, 60-64.
- Ishii, T. (1969). Enzyme histochemical studies of senile plaques and the plaque-like degeneration of arteries and capillaries (Scholz). *Seishin shinkeigaku zasshi = Psychiatria et neurologia Japonica* 71, 790-800.
- Jones, R.G., and Thompson, C.B. (2009). Tumor suppressors and cell metabolism: a recipe for cancer growth. *Genes & development* 23, 537-548.
- Kalluri, R., and Zeisberg, M. (2006). Fibroblasts in cancer. *Nature reviews Cancer* 6, 392-401.
- Kim, J.W., Tchernyshyov, I., Semenza, G.L., and Dang, C.V. (2006). HIF-1-mediated expression of pyruvate dehydrogenase kinase: a metabolic switch required for cellular adaptation to hypoxia. *Cell metabolism* 3, 177-185.
- King, A., Selak, M.A., and Gottlieb, E. (2006). Succinate dehydrogenase and fumarate hydratase: linking mitochondrial dysfunction and cancer. *Oncogene* 25, 4675-4682.

- Landex, N.L., Thomsen, J., and Kayser, L. (2006). Methimazole increases H₂O₂ toxicity in human thyroid epithelial cells. *Acta histochemica* 108, 431-439.
- Lardner, A. (2001). The effects of extracellular pH on immune function. *Journal of leukocyte biology* 69, 522-530.
- Locasale, J.W., and Cantley, L.C. (2011). Metabolic flux and the regulation of mammalian cell growth. *Cell metabolism* 14, 443-451.
- Lunnen, K.Y. (1983). Atlas of Pulmonary Pathology - Gibbs, Ar, Seal, Rme. *Phys Ther* 63, 1533-1533.
- Lunt, S.Y., and Vander Heiden, M.G. (2011). Aerobic glycolysis: meeting the metabolic requirements of cell proliferation. *Annual review of cell and developmental biology* 27, 441-464.
- Meier-Ruge, W.A., and Bruder, E. (2008). Current concepts of enzyme histochemistry in modern pathology. *Pathobiology : journal of immunopathology, molecular and cellular biology* 75, 233-243.
- Odeggaard, J.I., and Chawla, A. (2011). Alternative macrophage activation and metabolism. *Annual review of pathology* 6, 275-297.
- Osawa, E., Nakajima, A., Yoshida, S., Omura, M., Nagase, H., Ueno, N., Wada, K., Matsushashi, N., Ochiai, M., Nakagama, H., *et al.* (2002). Chemoprevention of precursors to colon cancer by dehydroepiandrosterone (DHEA). *Life sciences* 70, 2623-2630.
- Pavlidis, S., Vera, I., Gandara, R., Sneddon, S., Pestell, R.G., Mercier, I., Martinez-Outschoorn, U.E., Whitaker-Menezes, D., Howell, A., Sotgia, F., *et al.* (2012). Warburg meets autophagy: cancer-associated fibroblasts accelerate tumor growth and metastasis via oxidative stress, mitophagy, and aerobic glycolysis. *Antioxidants & redox signaling* 16, 1264-1284.
- Pavlidis, S., Whitaker-Menezes, D., Castello-Cros, R., Flomenberg, N., Witkiewicz, A.K., Frank, P.G., Casimiro, M.C., Wang, C., Fortina, P., Addya, S., *et al.* (2009). The reverse Warburg effect: aerobic glycolysis in cancer associated fibroblasts and the tumor stroma. *Cell Cycle* 8, 3984-4001.
- Piechaczyk, M., Blanchard, J.M., Marty, L., Dani, C., Panabieres, F., El Sabouty, S., Fort, P., and Jeanteur, P. (1984). Post-transcriptional regulation of glyceraldehyde-3-phosphate-dehydrogenase gene expression in rat tissues. *Nucleic acids research* 12, 6951-6963.

- Pool-Zobel, B., Veeriah, S., and Bohmer, F.D. (2005). Modulation of xenobiotic metabolising enzymes by anticarcinogens -- focus on glutathione S-transferases and their role as targets of dietary chemoprevention in colorectal carcinogenesis. *Mutation research* 591, 74-92.
- Pouyssegur, J., Sardet, C., Franchi, A., L'Allemain, G., and Paris, S. (1984). A specific mutation abolishing Na⁺/H⁺ antiport activity in hamster fibroblasts precludes growth at neutral and acidic pH. *Proceedings of the National Academy of Sciences of the United States of America* 81, 4833-4837.
- Prahoveanu, E., Bronitki, A., and Barbu, C. (1973). Studies on enzymes-lactic dehydrogenase, succinic dehydrogenase, alkaline phosphatase, glutamic-oxalacetic transaminase-in cell cultures. *Revue roumaine de virologie* 10, 217-226.
- Raghunand, N., and Gillies, R.J. (2000). pH and drug resistance in tumors. *Drug resistance updates : reviews and commentaries in antimicrobial and anticancer chemotherapy* 3, 39-47.
- Ralser, M., Wamelink, M.M., Kowald, A., Gerisch, B., Heeren, G., Struys, E.A., Klipp, E., Jakobs, C., Breitenbach, M., Lehrach, H., *et al.* (2007). Dynamic rerouting of the carbohydrate flux is key to counteracting oxidative stress. *Journal of biology* 6, 10.
- Reales-Calderon, J.A., Aguilera-Montilla, N., Corbi, A.L., Molero, G., and Gil, C. (2014). Proteomic characterization of human proinflammatory M1 and anti-inflammatory M2 macrophages and their response to *Candida albicans*. *Proteomics* 14, 1503-1518.
- Roos, A., and Boron, W.F. (1981). Intracellular pH. *Physiological reviews* 61, 296-434.
- Rutter, G.A., and Denton, R.M. (1988). Regulation of NAD⁺-linked isocitrate dehydrogenase and 2-oxoglutarate dehydrogenase by Ca²⁺ ions within toluene-permeabilized rat heart mitochondria. Interactions with regulation by adenine nucleotides and NADH/NAD⁺ ratios. *The Biochemical journal* 252, 181-189.
- Schlappack, O.K., Zimmermann, A., and Hill, R.P. (1991). Glucose starvation and acidosis: effect on experimental metastatic potential, DNA content and MTX resistance of murine tumour cells. *British journal of cancer* 64, 663-670.
- Seagroves, T.N., Ryan, H.E., Lu, H., Wouters, B.G., Knapp, M., Thibault, P., Laderoute, K., and Johnson, R.S. (2001). Transcription factor HIF-1 is a necessary mediator of the pasteur effect in mammalian cells. *Molecular and cellular biology* 21, 3436-3444.

- Singh, S.N., and Kanungo, M.S. (1968). Alterations in lactate dehydrogenase of the brain, heart, skeletal muscle, and liver of rats of various ages. *The Journal of biological chemistry* 243, 4526-4529.
- Sonveaux, P., Vegran, F., Schroeder, T., Wergin, M.C., Verrax, J., Rabbani, Z.N., De Saedeleer, C.J., Kennedy, K.M., Diepart, C., Jordan, B.F., *et al.* (2008). Targeting lactate-fueled respiration selectively kills hypoxic tumor cells in mice. *The Journal of clinical investigation* 118, 3930-3942.
- Spriet, L.L., Howlett, R.A., and Heigenhauser, G.J. (2000). An enzymatic approach to lactate production in human skeletal muscle during exercise. *Medicine and science in sports and exercise* 32, 756-763.
- Storz, P. (2005). Reactive oxygen species in tumor progression. *Frontiers in bioscience : a journal and virtual library* 10, 1881-1896.
- Sugimoto, H., Mundel, T.M., Kieran, M.W., and Kalluri, R. (2006). Identification of fibroblast heterogeneity in the tumor microenvironment. *Cancer biology & therapy* 5, 1640-1646.
- Tannahill, G.M., Curtis, A.M., Adamik, J., Palsson-McDermott, E.M., McGettrick, A.F., Goel, G., Frezza, C., Bernard, N.J., Kelly, B., Foley, N.H., *et al.* (2013). Succinate is an inflammatory signal that induces IL-1 β through HIF-1 α . *Nature* 496, 238-242.
- Ullah, M.S., Davies, A.J., and Halestrap, A.P. (2006). The plasma membrane lactate transporter MCT4, but not MCT1, is up-regulated by hypoxia through a HIF-1 α -dependent mechanism. *The Journal of biological chemistry* 281, 9030-9037.
- Van Noorden, C.J. (1989). Cytophotometric analysis of enzyme reaction rates in tissue sections. *The Histochemical journal* 21, 515-516.
- Van Noorden, C.J. (2010). Imaging enzymes at work: metabolic mapping by enzyme histochemistry. *The journal of histochemistry and cytochemistry : official journal of the Histochemistry Society* 58, 481-497.
- Van Noorden, C.J., Tas, J., and Vogels, I.M. (1983). Cytophotometry of glucose-6-phosphate dehydrogenase activity in individual cells. *The Histochemical journal* 15, 583-599.
- Vaupel, P. (2010). Metabolic microenvironment of tumor cells: a key factor in malignant progression. *Experimental oncology* 32, 125-127.
- Vaupel, P., and Mayer, A. (2007). Hypoxia in cancer: significance and impact on clinical outcome. *Cancer metastasis reviews* 26, 225-239.

- Veskoukis, A.S., Tsatsakis, A.M., and Kouretas, D. (2012). Dietary oxidative stress and antioxidant defense with an emphasis on plant extract administration. *Cell stress & chaperones* 17, 11-21.
- Warburg, O., Wind, F., and Negelein, E. (1927). The Metabolism of Tumors in the Body. *The Journal of general physiology* 8, 519-530.
- Wojtkowiak, J.W., Verduzco, D., Schramm, K.J., and Gillies, R.J. (2011). Drug resistance and cellular adaptation to tumor acidic pH microenvironment. *Molecular pharmaceutics* 8, 2032-2038.
- Zeylemaker, W.P., Klaasse, A.D., and Slater, E.C. (1969). Studies on succinate dehydrogenase. V. Inhibition by oxaloacetate. *Biochimica et biophysica acta* 191, 229-238.
- Zhang, H., Bosch-Marce, M., Shimoda, L.A., Tan, Y.S., Baek, J.H., Wesley, J.B., Gonzalez, F.J., and Semenza, G.L. (2008). Mitochondrial autophagy is an HIF-1-dependent adaptive metabolic response to hypoxia. *The Journal of biological chemistry* 283, 10892-10903.

7. Curriculum Vitae

Personal Data

Name Anne Elisabeth Miller

Education

2005 - 2008

High school graduation

Albert Schweizer Gymnasium, Marl, Deutschland

2008 – 2012

Bachelor of Science

Studies of Biology at the University of Cologne, Germany

2010

Research internship at the Oswaldo Cruz Foundation,
Rio de Janeiro, Brazil

2010 – 2011

Research internship at the Department for Biochemistry
at the University of Cologne, Germany

2011

Research internship at the Cologne cluster of excellence
in Cellular Stress Responses in Aging associated
Diseases, Cologne Germany

2011 – 2012

Practical work of the bachelor thesis at the Clinical
Institute for Microbiology and Hygiene, Medical University
Cologne, Germany

2012 – 2014

Master of Science

Studies of molecular Biology at the University of Vienna,
Austria

2013 – 2014

Practical work of the master thesis at the Clinical
Institute for Laboratory Medicine, Medical University of
Vienna, Austria

8. Danksagung

An dieser Stelle möchte ich mich bei allen Beteiligten bedanken, die mich bei der Erstellung dieser Arbeit unterstützt haben.

An erste Stelle steht dabei Mag. Arvand Haschemi, PhD bei dem ich mich für die Möglichkeit bedanken möchte unter seiner Anleitung zu lernen sowie für die weitere Betreuung und Unterstützung bei der Erstellung meiner Masterarbeit. Er hat mich immer wieder zu neuen Ideen inspiriert und mir neue Herausforderungen gestellt.

Ein weiterer Dank gebührt Univ. Prof. Dr. Oswald Wagner, der mir nicht nur zu meinem Arbeitsplatz verholfen hat, sondern mich auch im weiteren Verlauf meiner Tätigkeit unterstützt und betreut hat.

Ein besonderer Dank gilt Ao. Univ. Prof. Dr. Michael Bergmann und Assoc. Prof. Priv. Doz. Mag. Dr. Helmut Dolznig für die große Begeisterung für mein Projekt sowie für die Möglichkeit mit ihnen zusammenarbeiten zu dürfen.

Bei Alexander Jais möchte ich mich herzlich für seine Geduld, jegliche Unterstützung sowie für das Korrekturlesen bedanken. Er stand mir jederzeit mit ausführlichem Rat zur Seite.

Ebenso gilt mein Dank den weiteren Mitgliedern des Labors Elisa Einwallner, Csörsz Nagy, Gabriel Wagner und Gerfried Mitterer an welche ich mich mit jeglichen Fragen wenden und auf persönliche Unterstützung verlassen konnte.

Weiterer Dank gilt den Mitgliedern der Imaging Core Facility der medizinischen Universität Wien, Priv.-Doz.in Marion Gröger und Sabine Rauscher welche sich die Zeit dafür genommen haben mich in alle Geräte meiner Wahl einzuschulen und mit allen Mitteln versucht haben meine Extrawünsche zu erfüllen.

Insbesondere möchte ich mich auch bei meiner Familien und meinen Freunden bedanken, die mir über die ganze Zeit emotionalen und motivierenden Beistand geleistet haben.